PROJECT REPORT No. 435

A collection of papers on

"A Theoretical, Empirical and Experimental Investigation of the Spatial Scaling and Dynamics of Braided Rivers"

by E. Foufoula-Georgiou, Christopher Paola, Victor Sapozhnikov,
Deborah Nykanen, and A. Brad Murray
Principal Investigators

University of Minnesota
St. Anthony Falls Laboratory
Minneapolis, Minnesota

Research funded by

NATIONAL SCIENCE FOUNDATION
NATIONAL AERONAUTICS AND SPACE ADMINISTRATION

Table of Contents

WATER RESOURCES RESEARCH, VOL. 35, NO. 3, PAGES 843–851, MARCH 1999

St. Anthony Falls Laboratory
Technical Paper No. 574, Series A

Horizontal and vertical self-organization of braided rivers toward a critical state

Victor B. Sapozhnikov and Efi Foufoula-Georgiou

St. Anthony Falls Laboratory, University of Minnesota, Minneapolis

Abstract. Self-organization in an experimental braided river is studied. It is shown that the experimental braided river self-organizes into a critical state where it shows dynamic scaling; that is, small and large parts of the river evolve statistically identically after proper renormalization of space and time. The dynamic scaling emerges during the process of approaching the critical state which involves self-adjustment of both profile (vertical self-organization) and braiding pattern (horizontal self-organization). The obtained result corroborates the hypothesis suggested by the authors earlier [*Sapozhnikov and Foufoula-Georgiou*, 1997] that braided rivers are self-organized critical systems. The results are also important for understanding and statistically predicting the behavior of natural braided rivers because, owing to external conditions (e.g., sudden streamflow changes), some of them may be driven out of the critical state and therefore may show deviation from dynamic scaling.

1. Introduction

Braided rivers are complex systems characterized by hierarchical geometry and rapid evolution. Different approaches have been used to describe and understand their morphology and dynamics. A bulk of research on braided rivers has focused on detailed study of processes in a small area, such as flow and sediment flux around a single channel bar or confluence [*Ashmore and Parker*, 1983; *Ashmore et al.*, 1992; *Best*, 1986, 1988; *Bristow et al.*, 1993; *Mosley*, 1976, 1977; *Robert*, 1993]. Another approach involves exploring statistical properties of the spatial structure and evolution of braided rivers from the point of view of unraveling and quantifying scale relationships in space and time [*Sapozhnikov and Foufoula-Georgiou*, 1996, 1997; *Foufoula-Georgiou and Sapozhnikov*, 1998]. It is hoped that this approach can shed new light on braided rivers as a whole in terms of understanding the underlying mechanisms responsible for the formation and evolution of braided patterns, and statistical prediction of their behavior.

From the analysis of three natural braided rivers, *Sapozhnikov and Foufoula-Georgiou* [1996] showed that these rivers exhibit anisotropic spatial scaling in their static morphology. This implies that a smaller part of a river, stretched differently along the mainstream and the perpendicular directions, is statistically identical to a larger part. Later, *Sapozhnikov and Foufoula-Georgiou* [1997] presented experimental evidence that in addition to the spatial scaling, stationary braided rivers (i.e., rivers given enough time to reach statistical equilibrium under constant external conditions) exhibit dynamic scaling in their evolution. The presence of dynamic scaling implies that a smaller part of a braided river evolves identically (in the statistical sense) to a bigger part provided that time is rescaled by a factor which depends only on the ratio of the spatial scales of the two parts.

The presence of dynamic scaling together with other theoretical considerations led us to conjecture [*Sapozhnikov and Foufoula-Georgiou*, 1997] that braided rivers belong to self-organized critical (SOC) systems [see *Bak et al.*, 1987]. Indeed, in stationary systems, dynamic scaling is a signature of critical state. Also, a large number of degrees of freedom (i.e., a large number of possible independent changes in the patterns) and nonlinearity, both of which are present in braided rivers, are typical of self-organized critical phenomena. SOC systems bring themselves to a critical state which is an attractor of their dynamics. This is different from traditional critical systems, which require external fine tuning of a driving parameter (e.g., temperature in the case of a magnetic material or concentration in the case of a percolation system) to be brought to a critical state [e.g., *Ma*, 1976].

Since by definition SOC systems show critical behavior only after they have brought themselves to a critical state, which is also a statistical equilibrium state, *Sapozhnikov and Foufoula-Georgiou* [1997] left their experimental braided river to evolve until both its profile and braiding pattern reached equilibrium, and then the presence of SOC was tested. We note here that the profile reached the static equilibrium (i.e., it stopped changing), whereas the braiding pattern, while remaining statistically the same, was undergoing continual changes (statistical equilibrium). After the river reached the equilibrium state we analyzed it for criticality and, indeed, found the presence of dynamic scaling, an indicator of a critical state.

However, a more thorough study of a SOC system requires exploration of its behavior not only at equilibrium but also before it reaches this state. Thus, in this study we examine an experimental braided river at different stages, as it approaches statistical equilibrium. There are two motivations for such a study. The first motivation is theoretical. It stems from the fact that critical systems show dynamic scaling at the critical state but deviate from dynamic scaling as they are driven out of this state [e.g., see *Ma*, 1976]. Therefore, to confirm that a state a system brought itself into is critical, it is important not only to demonstrate the presence of dynamic scaling at this state but also to show that the dynamic scaling was not present before and only arose as the system approached this state. The second motivation stems from the fact that in transferring results from

Paper number 98WR02744.
0043-1397/99/98WR-02744$09.00

an idealized experimental environment to natural braided rivers one cannot neglect the fact that a natural river may not be exactly at the equilibrium state. This may be due to natural variability of external factors, as, for example, abrupt discharge changes or long-timescale tectonic events. Another reason is that the river may have changed its path, and therefore, even if the external conditions are stable after the change, the river might simply not have had enough time to reach the equilibrium (this includes slope buildup and reworking external constraints, like mountains). As discussed in section 5, knowing the behavior, in terms of deviation from dynamic scaling, of natural rivers which are not quite at the equilibrium state is needed for statistical prediction of the evolution of such rivers.

In this work an experimental braided river is studied for presence of dynamic scaling at the equilibrium state and before it approached this state. The closeness to the equilibrium state is considered with respect to two factors: profile shape (vertical self-adjustment of the river) and braiding pattern (horizontal self-adjustment). A significantly larger body of data than that used by *Sapozhnikov and Foufoula-Georgiou* [1997] has been obtained and analyzed for the present study.

It should be mentioned that the anisotropy of dynamic scaling, implying that the river evolution scales differently in the direction of the slope and in the perpendicular direction [see *Foufoula-Georgiou and Sapozhnikov*, 1998], has not been considered herein. Rather, we employed the isotropic dynamic scaling framework of *Sapozhnikov and Foufoula-Georgiou* [1997], as it better suits the purpose of this study, which requires establishing presence or absence of dynamic scaling and not evaluating the scaling exponents. Also, the advantage of this framework is that it is more robust and less data-demanding and thus can handle "difficult" cases when the river has approached dynamic scaling but has not quite reached it yet.

2. Review of the Theory

The theoretical framework of testing for the presence of dynamic scaling based on changes in the analyzed objects is described in detail by *Sapozhnikov and Foufoula-Georgiou* [1997]. Here we present only in brief the essence of the theory.

Spatial scaling in a fractal object implies that the object looks statistically the same at different spatial scales. If, additionally, it evolves in such a way that after a proper rescaling of time its evolution is also statistically indistinguishable at different scales, then we say that in addition to spatial scaling, the object exhibits dynamic scaling. The space-time rescaling has the form

$$t_2/t_1 = (L_2/L_1)^z \tag{1}$$

where L_1 and L_2 are the scales at which the evolution of the object is considered, t_2/t_1 is the time rescaling factor, and z is called the dynamic scaling exponent. One can see (1) as providing the space-time rescaling needed to have the projection of the evolution of part $L_1 \times L_1$ on a screen, statistically indistinguishable from the projection of part $L_2 \times L_2$ on a screen of the same size.

Let us characterize the evolution of a stationary fractal object by "changes" in its pattern, where changes are defined as parts of the space which were not occupied by the object at a certain moment of time but became occupied after some time lag t. Let $n(l' > l, t)$ denote the number of changes exceeding size l after some time lag t, and let D be the fractal dimension of the object (e.g., in this work it is the fractal dimension of the braided river spatial pattern). It can be shown [see *Sapozhnikov and Foufoula-Georgiou*, 1997] that the condition for dynamic scaling (1) can be written in terms of the statistics of changes as

$$n(l' > l, t) = l^{-D} f(t/l^z) \tag{2}$$

where $f(\ )$ is some function.

For time lag $t = 0$, there are no changes in the object, which implies $n(l' > l, 0) = 0$, and, correspondingly, $f(0) = 0$. If for small values of the argument the function f can be approximated by a power law, with some exponent β, then the condition (2) for dynamic scaling takes the form

$$n(l' > l, t) \sim t^{\beta} l^{-D-\beta z} \tag{3}$$

Although, in contrast to (2), (3) holds only for small values of t/l^z, it can be conveniently used to facilitate the estimation of the dynamic scaling exponent z. Specifically, the following procedure of estimating z was employed by *Sapozhnikov and Foufoula-Georgiou* [1997]. It was based on their empirical finding that indeed in the experimental braided river, at small t/l^z values,

$$n(l' > l, t) \sim l^{-k} \tag{4}$$

for every fixed value of the time lag t, and

$$n(l' > l, t)/l^k \sim t^{\beta} \tag{5}$$

for every fixed value of l.

These two equations coincide with (3) with the dynamic exponent z given as

$$z = (k - D)/\beta \tag{6}$$

Thus, in a system showing dynamic scaling one can first estimate the k exponent from the log-log plots of $n(l' > l, t)$ versus l (for several fixed values of t) and the β exponent from the log-log plot of $n(l' > l, t)/l^k$ against t. This, together with the fractal dimension D of the system (estimated using, for example, the mass-in-a-box method; *Mandelbrot* [1982]) enables estimation of z using (6). Then one can plot for the estimated value of z, the values of $n(l' > l, t)l^D$ versus t/l^z, for all (and not only small) values of t/l^z, to verify that the general equation of dynamic scaling (2) holds. Collapsing of all curves to a single curve, the $f(\ )$ curve in (2), would verify the presence of dynamic scaling in the river. The procedure is schematically displayed in Figure 1.

3. Experimental Setup

The experimental setup used to collect the data for this analysis is similar to that described by *Sapozhnikov and Foufoula-Georgiou* [1997], and the reader is referred to that work for more details. Here we present only a brief description and then elaborate on the procedures we used to introduce vertical and horizontal disturbances in the system and to monitor its recovery.

A 5 × 0.75 m experimental basin was constructed at the St. Anthony Falls Laboratory. Sediment and water were supplied continuously at a precisely controlled rate. The sediment and water were combined together in a mixing funnel before injection into the basin. The grain size of the supplied sediment was 0.12 ± 0.03 mm. The water discharge was 20 g/s, and the

sediment supply was 0.6 g/s. A video camera recorded the evolution of the system. To visualize the river and monitor its depth, dye was supplied continuously during each videotaping session. After each videotaping session the dye supply was cut, and water flushed the dye from the system in a matter of a few hours. The recorded data were subsequently digitized for treatment and analysis. The studied region size was 0.75 × 1.0 m and was located between the 2.8 and 3.8 m marks (measured from the point of inflow). The final resolution of images was 3 mm across the river and 1.5 mm along the river.

The evolution of the braided river was characterized by monitoring changes in the pattern of the river and analyzing them according to the procedure described in section 2. It should be noticed that extracting the river patterns from the videotaped images presented significant difficulties, because very soon the sediment was colored with the same dye as water. However, extracting changes in the river patterns by subtracting images taken at different instants of time was found to be quite plausible, since the colored sediment patterns were almost the same and got zeroed when subtracted. Although changes in a river are three-dimensional, as is the river itself, we only considered in our previous work and here their horizontal projections. Thus changes (reflected by differences in the darkness of the images) represent water depth changes which include the cases of covering with water a previously dry area or exposing a previously water-covered area.

Before the experiment started, a certain initial amount of sediment was put manually in the basin such that a linear profile with a constant slope of 0.032 was formed (see Figure 2). This linear shape of the profile was different from the concave-shaped profile of the same average slope which would have been obtained had it been left to build up itself. Therefore the initially imposed shape of the profile can be considered as a vertical disturbance of the river. The profile of the river was monitored as it progressed. The initial profile and the

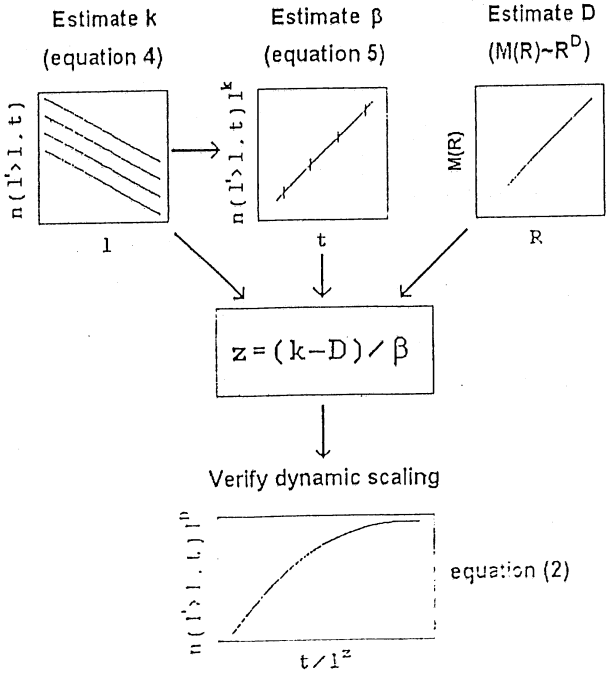

Figure 1. Schematic of estimation and verification procedure for dynamic scaling.

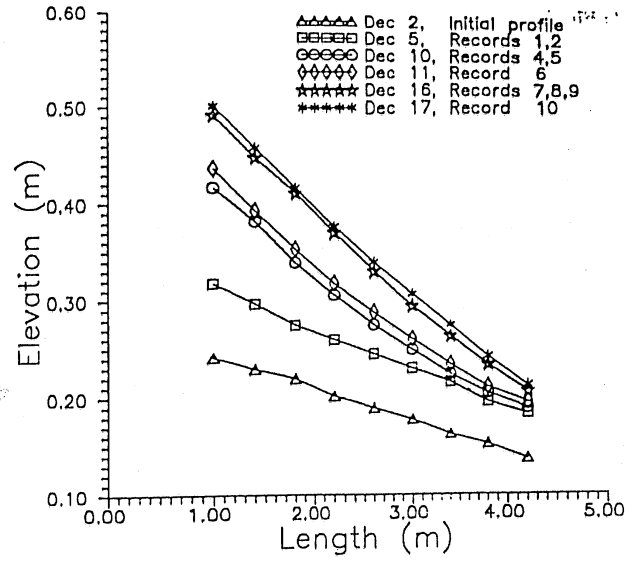

Figure 2. Evolution of the experimental braided river profile.

profiles at the days when the video records of the river were taken are shown in Figure 2.

At several instances of time (with different profiles of the river) we manually wiped out the braiding pattern, thus introducing a horizontal disturbance. In these cases it took several hours for the river to recover the pattern. The process of recovering the braided pattern (horizontal self-adjustment of the river) was followed by recording the behavior of the river immediately after wiping out the braided pattern, after the pattern partially recovered, and after it recovered completely (the judgment on a complete recovery was made visually, by seeing that the degree of braiding was restored and that statistically, the braiding pattern did not change anymore). We qualitatively characterized the degree of braiding by attributing each pattern to one of three groups: "not braided" (immediately after the braiding pattern was erased), "half braided" (when the braiding was restored partially, usually about half an hour after the pattern was wiped out), and "fully braided" (several hours or more later). We did not characterize the degree of braiding more quantitatively, such as by computing the braiding index, because, as was mentioned earlier, the colored sediment did not allow accurate extraction of the braided river patterns, although it permitted accurate extraction of changes.

The process of recovery of the river from these disturbances was followed by recording the behavior of the river after the disturbances were introduced. We collected and analyzed the statistics of changes in the river at different days, as the river profile was building up and at different degrees of braiding. Table 1 displays the time the records were taken, the qualitative degree of braiding of the river for each record, and the average slope of the recorded region of the river (recall that this region had a length of 1 m and was located between the 2.8 and 3.8 m marks measured from the inflow point).

4. Results

First, at different profiles and different degrees of recovery of the braided patterns (records 1–10 in Table 1), the param-

Table 1. Video Recordings of the Experimental Braided River

Record ID	Day of the Experiment	Slope	Braiding
Record 1	3	0.037	none
Record 2	3	0.037	half
Record 3	4	0.041	full
Record 4	9	0.058	none
Record 5	9	0.058	half
Record 6	10	0.063	full
Record 7	15	0.080	full
Record 8	15	0.080	none
Record 9	15	0.080	half
Record 10	16	0.081	full

eter k was estimated from (4) using small values of the time lag t (4–32 s) and large enough values of l. The estimation was done only where appropriate, that is, where the $n(l' > l, t)$ versus l dependencies were a series of reasonably parallel straight lines in the log-log scale (Figure 3). Then from (5) the values of β were estimated (Figure 4). From the estimated values k and β the dynamic scaling exponent z was calculated using (6). Table 2 shows the estimated values of the parameters k, β, and z for different profiles and degrees of braiding. Absence of values for some records indicates lack of log-log linearity or parallelism in the $n(l' > l, t)$ versus l dependence even for small t/l^z values and therefore lack of dynamic scaling.

As mentioned above, (4) and (5) express scaling only for small values of the t/l^z parameter. They are convenient to use for estimating the dynamic scaling exponent z under the assumption that dynamic scaling is present in the system but by themselves are not enough to answer the question of whether dynamic scaling is indeed present. Only the general equation (2), which must be satisfied for all values of t/l^z, can answer this question. Therefore, for all records which satisfied (4) and (5) we plotted (using the estimated values of z) the values of $n(l' > l, t)l^D$ versus t/l^z, for different time lags from 4 to 256 s to test for each of them if the dynamics of the river satisfy the general equation of dynamic scaling (2) at any time lag. The value of D was estimated from a tracing of the river (using a mass-in-a-box method) as 1.7. Presence of dynamic scaling would be indicated by the fact that all $n(l' > l, t)l^D$ versus t/l^z curves for all time lags collapse to a single curve. As one can see in Plate 1, where the plots are presented, only records 7 and 10 reveal a reasonably good dynamic scaling. Note from Table 2 that these records correspond to the cases when the river was given enough time to develop the profile and to recover its braided pattern after it was wiped out. In all other cases when the river was not given enough time to either self-adjust its slope or to recover its braiding pattern after wiping it out, the dynamic scaling was not present. Thus the braided river paved its way to dynamic scaling through both vertical and horizontal self-organization.

5. Discussion and Conclusions

The main goal of this study was to provide more concrete evidence which would support or disprove our earlier hypothesis that braided rivers are self-organized critical systems [*Sapozhnikov and Foufoula-Georgiou*, 1997]. This hypothesis was based on our finding that in the statistical equilibrium state our experimental braided river showed dynamic scaling, and also on the fact that braided rivers are nonlinear systems with a high number of degrees of freedom, which is typical of SOC systems. However, there is one more crucial feature of critical systems: The quality of scaling in such systems depends on how close they are to the critical state [e.g., see *Ma*, 1976]. Therefore, to verify our hypothesis, we had to test whether the dynamic scaling really arises and improves with time, as the river undergoes self-organization. We believe that the results of this study showing that indeed dynamic scaling is not always present but develops only if the river is given enough time to self-organize strongly support our hypothesis and, together with the previous arguments, provide enough evidence that braided rivers are self-organized critical systems. Therefore they can be studied under the general framework of critical phenomena. This framework provides a conceptual basis for understanding critical systems as well as an apparatus for their description.

A distinct feature which makes braided rivers (together with some other SOC systems, such as a sandpile) essentially different from the traditional critical systems (such as magnetic materials) is the clear anisotropy between horizontal and vertical directions, produced by gravity. In fact, it was found in this study that the process of approaching the critical state by a braided river involves self-adjustment of both profile (vertical self-organization) and braiding pattern (horizontal self-organization). The theory of critical state of anisotropic systems is not developed yet. However, one can hypothesize that in contrast to the well-studied traditional isotropic critical systems, it takes tuning (self-tuning in the case of SOC systems) of more than one parameter to bring such systems to the critical state. Specifically, on the basis of the results of the experiment testifying that braided rivers exhibit dynamic scaling only after they undergo both vertical and horizontal self-adjustment, we conjecture that there are at least two self-tuning parameters which drive braided rivers to a critical state: One of them reflects vertical self-organization (profile self-adjustment), and the other accounts for horizontal self-organization (development of a braided pattern).

It should be noted that the two objectives, (1) revealing how the river self-organizes if it is left to evolve freely and (2) following how different factors affect the presence of dynamic

Table 2. Estimation of the k, β, and z Parameters of the Experimental Braided River

Day of the Experiment	Braiding		
	None	Half	Full
3, 4	record 1: ...	record 2: ...	record 3: k = 2.63, β = 2.74, z = 0.32
9, 10	record 4: ...	record 5: k = 2.43, β = 2.63, z = 0.28	record 6: k = 2.12, β = 2.26, z = 0.14
15, 16	record 8: k = 2.00, β = 2.03, z = 0.15	record 9: k = 2.41, β = 2.32, z = 0.31	record 7: k = 2.49, β = 2.41, z = 0.33
			record 10: k = 2.67, β = 2.34, z = 0.42

Absence of values for some records indicates lack of log-log linearity and thus lack of dynamic scaling.

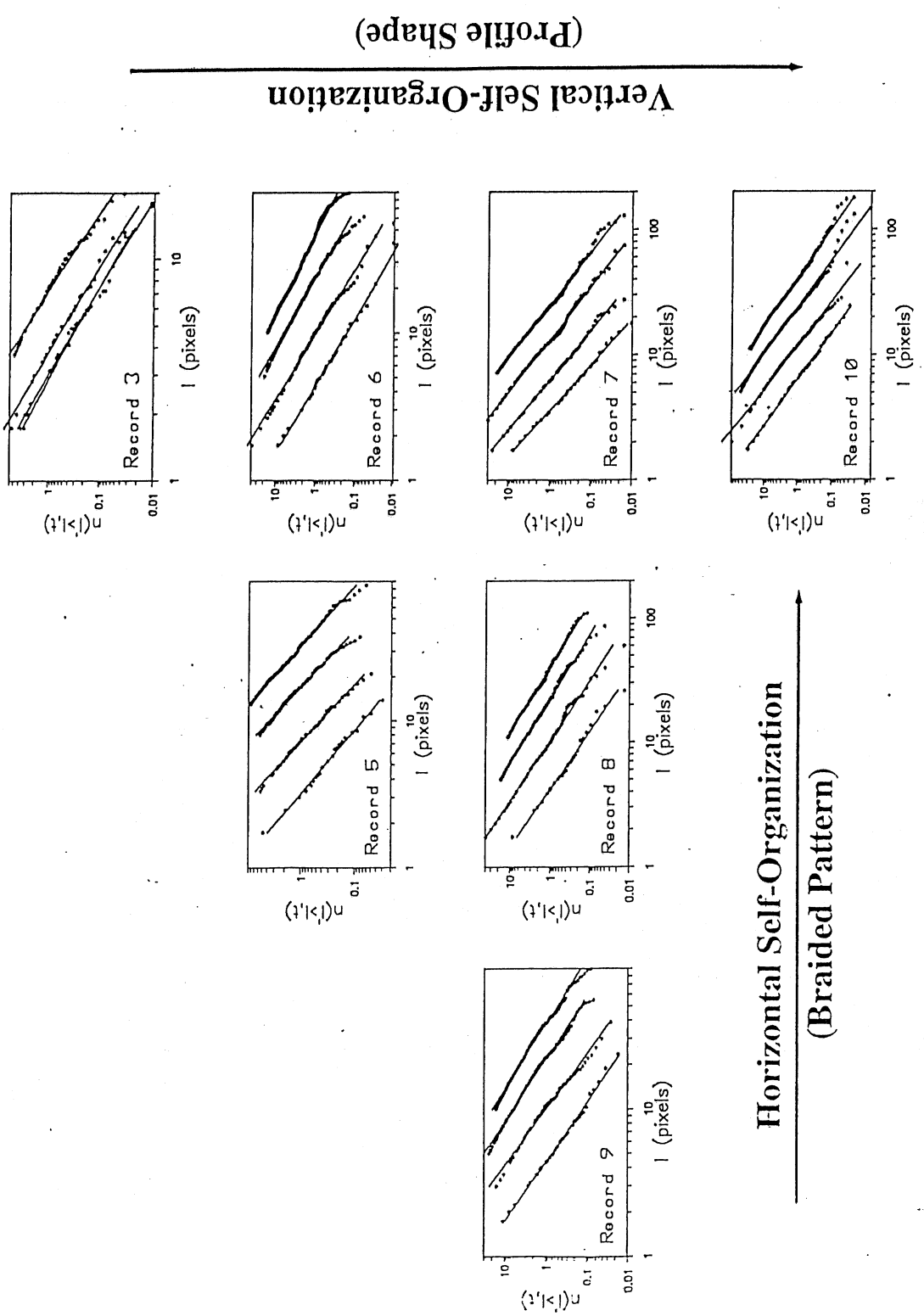

Figure 3. Estimation of the k exponent in the river (see equation (4)). For all records, except record 3, the curves are plotted for time lags t of 4, 8, 16, and 32 s (from bottom to top). For record 3 the time lags of 16, 32, 64, and 128 s are shown because the evolution of the river was slower owing to a lower slope.

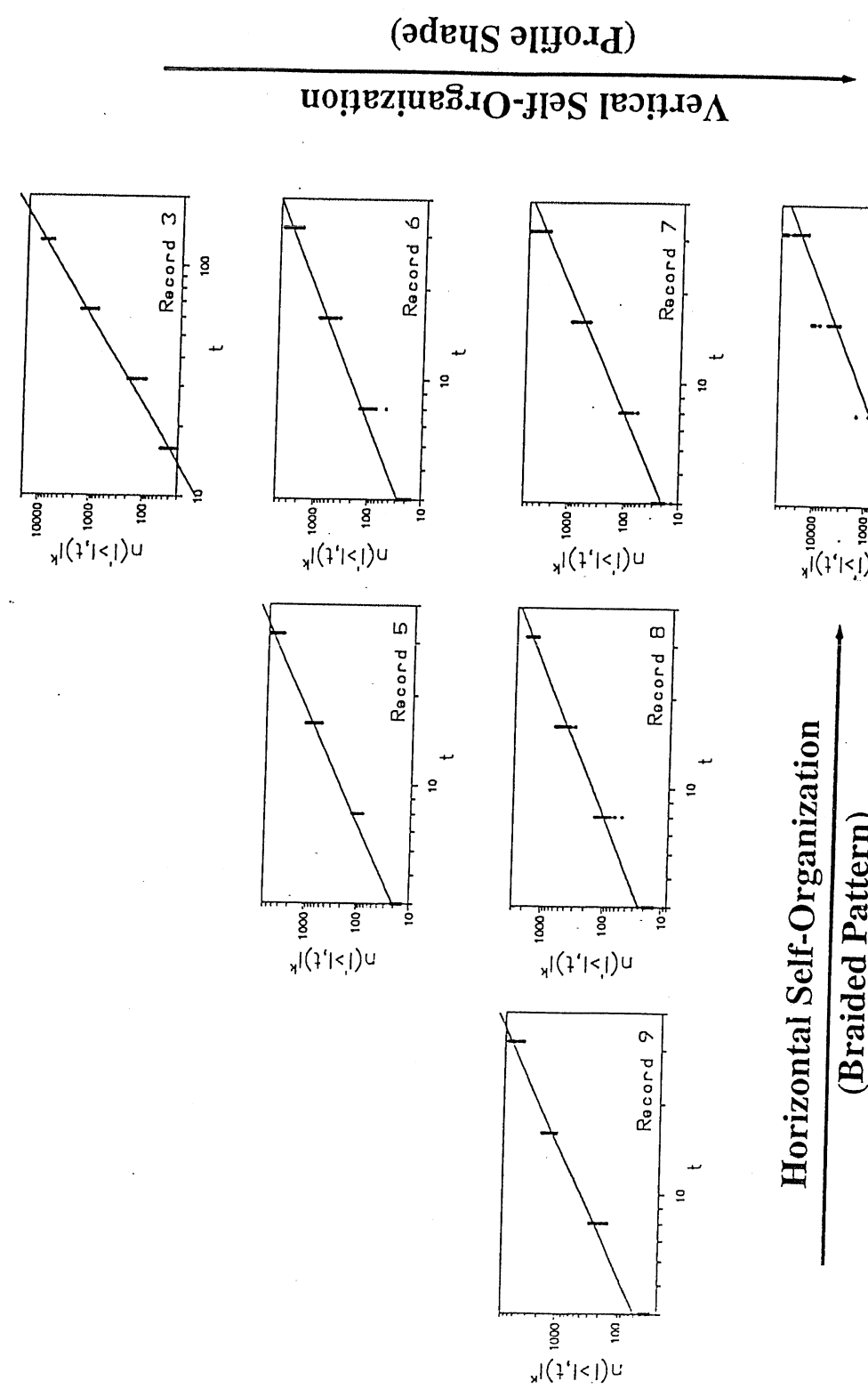

Figure 4. Estimation of the β exponent in the river (see equation (5)). Every vertically grouped set of points corresponds to one of the four distributions shown in Figure 3.

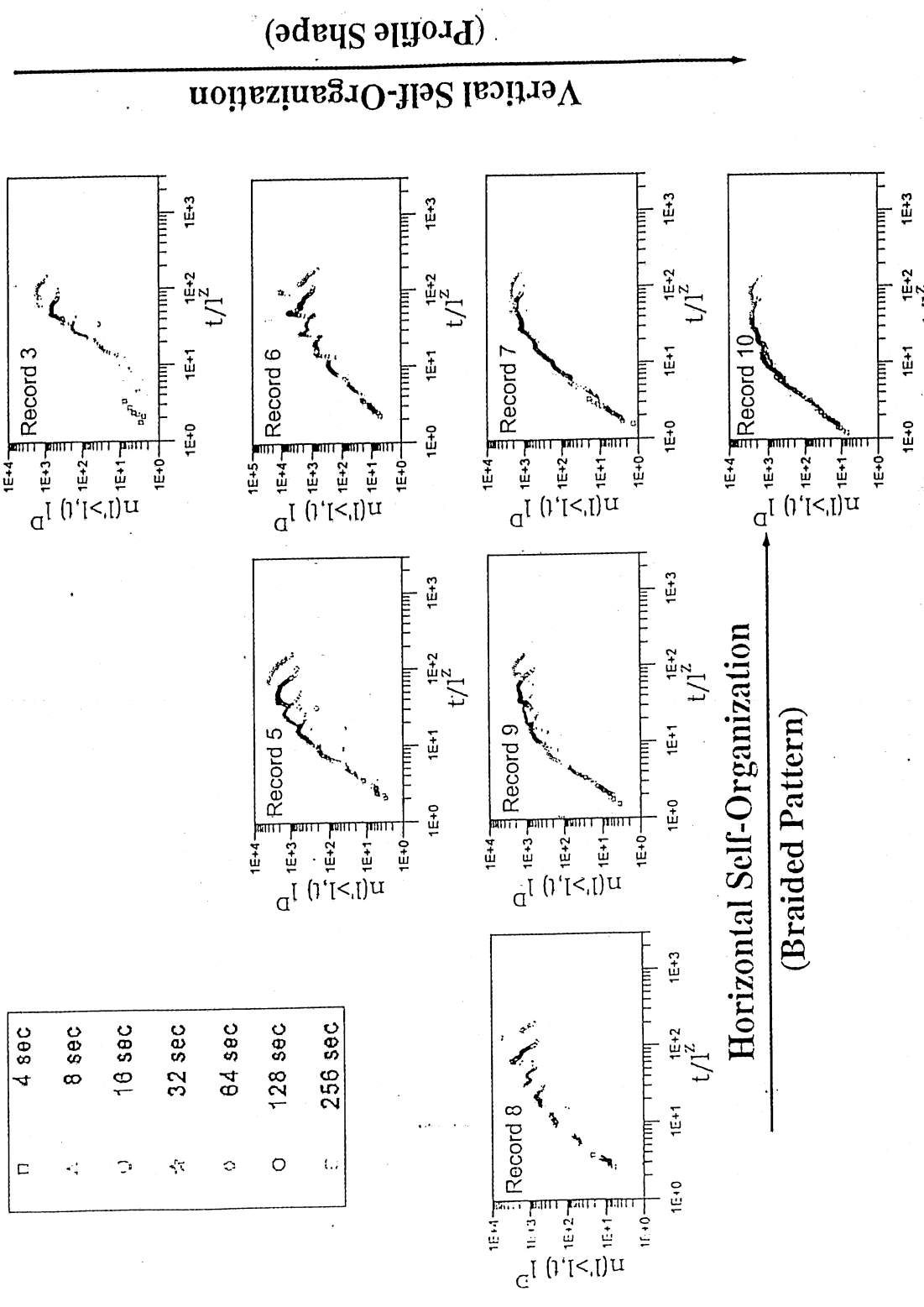

Plate 1. Verification of the presence of dynamic scaling in the experimental braided river according to the general equation (2). Observe how the dynamic scaling improves as the system undergoes vertical and horizontal self-organization.

scaling in the river, in a way conflict with each other from the point of view of their experimental implementation. This is because while the first one supposes that the river is left to evolve undisturbed, the second one requires introducing disturbances in the braided river system. This problem is common to all SOC systems which organize in a critical state themselves, and it can leave one with the dilemma to either (1) only observe the system approaching the critical state and not control the driving parameters or (2) control the parameters and accept the fact that the self-organization process is disturbed. However, one may be able to resolve this problem by separating the two processes in time, namely, by introducing short-time disturbances and then allowing for undisturbed self-organization in the system. In our case this was easier to implement for the horizontal than for the vertical self-adjustment. The reason for that is that the braided river was fairly shallow (deepest channels were just several millimeters in depth), and thus horizontal disturbances, that is, disturbances of the braided pattern, involved less bed material transport, even if the pattern was completely wiped out, and therefore required less time to recover than drastic vertical disturbances (significant changes of the profile). Thus we were able to introduce horizontal disturbances several times by erasing the braiding pattern and observe the river self-recovery afterward, while the vertical disturbance was imposed only once, by creating an initial profile which was far from the one which the river would have produced itself had it been left undisturbed.

It should be mentioned that on its way to the final equilibrium, and if left to develop without interference, the profile of the river undergoes an infinite series of relatively stable profiles. Although the profile keeps changing as the bed is built up, the change occurs significantly slower than the change caused by an artificially imposed profile disturbance of an arbitrary shape. Thus we call every naturally built profile a "quasi-equilibrium profile," in contrast to the profiles with the imposed disturbance. As the river evolved, it was recovering from the initial vertical disturbance by approaching a profile of a quasi-equilibrium shape, and at the same time it was developing toward the final equilibrium profile. This final equilibrium profile obtained by *Sapozhnikov and Foufoula-Georgiou* [1997] under the same conditions (same water and sand supply) is known to have a uniform slope of 0.15. We notice here, however, that by the time the dynamic scaling in the system had been achieved, the river was far from its final equilibrium profile. Indeed, as one can see from Table 1, the slope of the observed region was 0.08 when the dynamic scaling was achieved, which is approximately half the final equilibrium slope of 0.15. Therefore we hypothesize that the river reached the dynamic scaling because it reached a profile of a quasi-equilibrium shape (which continued to develop via other quasi-equilibrium profiles to the final equilibrium) and not because it approached closely enough the final equilibrium profile. Further experiments involving disturbances of the shape of several quasi-equilibrium profiles, as they approach the final equilibrium profile, are needed to answer this question conclusively. The disturbances would need to be small enough to enable introducing several of them before the final equilibrium profile is reached.

It has been long argued in the literature that relating scaling in natural objects to their physical properties is a high-priority task. The finding of this work that dynamic scaling in braided rivers arises only as they approach equilibrium (statistical equilibrium for the braided pattern and quasi-equilibrium for the profile) provides a highly desired connection between the scaling properties of the rivers and their physical state (closeness to equilibrium). Besides, it provides a quantitative tool of judging whether a braided river is close to equilibrium by checking its deviation from dynamic scaling. In a relatively short period of time one can collect information on the evolution of a natural river which would permit testing for the presence of dynamic scaling. The absence of dynamic scaling would imply that the river is far from equilibrium.

Although we presented here evidence that dynamic scaling arises in braided rivers only as they approach a stationary (critical) state, it is important for prediction purposes to be able to characterize quantitatively their deviation from the dynamic scaling behavior as a function of their deviation from stationarity. For that one would have to introduce two parameters describing the vertical and the horizontal self-organization of a braided river which would play the role of "temperature" in reaching the critical state of a traditional system. At this point we cannot be more specific other than suggesting that the first self-tuning parameter should reflect the shape of the profile (curvature and possibly the average slope) and the second one should depend on the braiding index. Considering the importance of old inactive channels as preferred pathways for active channel switching, an index which includes both active and inactive channels might be needed to describe the horizontal self-organization tuning parameter. The introduction of such two parameters would allow description of braided rivers which did not quite reach the critical state, a case which is often expected in natural systems. Indeed, it is known from the theory of the critical state [e.g., see *Ma*, 1976] that systems which are close to a critical state but not quite in it show scaling up to a certain scale (the correlation scale) which depends on the closeness of the system to the critical state. Thus description of such rivers in the dynamic scaling framework would still be possible, within, however, a more limited range of spatial and temporal scales.

Acknowledgments. This research was supported by NSF grant EAR-9628393 and NASA grant NAG5-6191. Supercomputer resources were kindly provided by the Minnesota Supercomputer Institute.

References

Ashmore, P., and G. Parker, Confluence scour in coarse braided streams, *Water Resour. Res.*, *19*, 392–402, 1983.

Ashmore, P. E., R. I. Ferguson, K. L. Prestegaard, P. J. Ashworth, and C. Paola, Secondary flow in anabranch confluences of a braided, gravel-bed stream, *Earth Surf. Processes Landforms*, *17*, 299–311, 1992.

Bak, P., C. Tang, and K. Wiesenfeld, Self-organized criticality: An explanation of 1 *f* noise, *Phys. Rev. Lett.*, *59*, 381–384, 1987.

Best, J. L., The morphology of river channel confluences, *Prog. Phys. Geogr.*, *10*, 157–174, 1986.

Best, J. L., Sediment transport and bed morphology at river channel confluences, *Sedimentology*, *35*, 481–498, 1988.

Bristow, C. S., J. L. Best, and A. G. Roy, Morphology and facies models of channel confluences, in *Fluvial Sedimentology*, edited by M. Marzo and C. Puigdefabregas, *Spec. Publ. Int. Assoc. Sedimentol.*, *17*, 91–100, 1993.

Foufoula-Georgiou, E., and V. B. Sapozhnikov, Anisotropic scaling in braided rivers: An integrated theoretical framework and results from application to an experimental river, *Water Resour. Res.*, *34*, 863–867, 1998.

Ma, S. K., *Modern Theory of Critical Phenomena*, Benjamin, White Plains, N. Y., 1976.

Mandelbrot, B. B., *The Fractal Geometry of Nature*, W. H. Freeman, New York, 1982.
Mosley, M. P., An experimental study of channel confluences, *J. Geol.*, *84*, 535–562, 1976.
Mosley, M. P., Stream junctions—A probable location for bedrock placers, *Econ. Geol.*, *72*, 691–697, 1977.
Robert, A., Bed configuration and microscale processes in alluvial channels, *Prog. Phys. Geogr.*, *17*, 123–136, 1993.
Sapozhnikov, V., and E. Foufoula-Georgiou, Self-affinity in braided rivers, *Water Resour. Res.*, *32*, 1429–1439, 1996.
Sapozhnikov, V. B., and E. Foufoula-Georgiou, Experimental evidence of dynamic scaling and indications of self-organized criticality in braided rivers, *Water Resour. Res.*, *33*, 1983–1991, 1997.

E. Foufoula-Georgiou and V. B. Sapozhkinov, St. Anthony Falls Laboratory, University of Minnesota, Mississippi River at Third Avenue, SE, Minneapolis, MN 55414-2196. (efi@mykonos.safhl.umn.edu; sapoz001@maroon.tc.umn.edu)

(Received March 24, 1998; revised August 21, 1998;
accepted August 21, 1998.)

St. Anthony Falls Laboratory
Tech. Paper No. 563, Series A

WATER RESOURCES RESEARCH, VOL. 34, NO. 9, PAGES 2353–2364, SEPTEMBER 1998

Validation of braided-stream models: Spatial state-space plots, self-affine scaling, and island shapes

Victor B. Sapozhnikov
St. Anthony Falls Laboratory, Department of Civil Engineering, University of Minnesota, Minneapolis

A. Brad Murray and Chris Paola
Department of Geology and Geophysics, University of Minnesota, Minneapolis

Efi Foufoula-Georgiou
St. Anthony Falls Laboratory, Department of Civil Engineering, University of Minnesota, Minneapolis

Abstract. We present a comprehensive approach for validating braided-stream models and apply it to a specific cellular braided-stream model. The approach involves quantitative comparison of modeled and natural braided streams in terms of two main aspects: the sequential organization of their plan patterns studied using their state-space characteristics and the hierarchical organization of their patterns studied in the framework of self-affine scaling. These two aspects of braided streams are complementary to each other and taken together provide a sensitive test of the validity of a model of braided streams. The simple model we examine produces patterns that are similar to those of natural braided rivers in terms of both sequential organization and self-affine scaling. This finding supports the conclusion that the nonlinear interactions between water and sediment in the model are the primary mechanisms responsible for shaping braided rivers in nature.

1. Introduction

A new computational model for fully developed braided streams has been proposed recently by *Murray and Paola* [1994]. Water and sediment are routed from cell to cell in a computational grid using simple abstractions of the governing conservation equations for mass and momentum. The model appears to reproduce the main dynamic features of stream braiding: formation of multiple interwoven channels separated by islands within which the flow shifts continuously from path to path, reshaping the islands as it does so. The model also reproduces broadband fluctuations in sediment discharge that have been observed in laboratory and field braided rivers.

Given the simplicity of the model, its ability to reproduce many features of real braided rivers even at a qualitative level is encouraging. But how does one test such a model quantitatively? In many systems whose spatial patterns possess one or more well-defined characteristic length scales, the first test is to see how well the model results match these scales quantitatively. However, recent work by *Sapozhnikov and Foufoula-Georgiou* [1996, 1997] has shown that braided rivers exhibit self-affine scaling in their morphology and that their temporal dynamics is consistent with self-organized critical behavior. These results suggest that braided rivers do not possess characteristic length scales, either when viewed as static spatial patterns or in terms of their temporal evolution. What is the best way to test models of such a system?

In this paper, we present a comprehensive approach to testing braided-stream models on the basis of two main aspects: the sequential organization and the hierarchical organization of their plan patterns. These two aspects of braided streams are complementary to each other, as the first depicts the river pattern in the dynamical-system theory framework and the second one describes scale-invariant characteristics of the braided-stream system.

Before discussing the technical details of the model and the various tests, a brief overview of the philosophy of the various approaches for model validation of a complex, scale-invariant system may be helpful. The basic question in model validation is, what are the features of the system of interest that are truly fundamental and give it its distinctive character? For instance, there is an extensive body of literature describing stability theories of stream meandering [e.g., see *Parker*, 1976; *Fredsoe*, 1978]. Two basic criteria are used to evaluate these theories: correct prediction of the physical conditions needed to produce meandering (primarily in terms of channel width-depth ratio) and correct prediction of the ratio of meander wavelength to channel width. These criteria are appropriate for such systems because meandering has a clear, dominant wavelength; indeed, the requirement of a preferred wavelength is embedded in the whole notion of stability analysis [*Parker*, 1976; *Fredsoe*, 1978], in which the single most unstable wavelength is presumed to dominate the fully developed system. Although the initial development of a braided pattern from a straight channel does appear to involve a single dominant bar wavelength, as described in stability theories, the picture for fully developed braiding is quite different. The original regular pattern of bars breaks up into a complex network of bars and channels on many length scales. Though it appears to remain statistically stationary (given constant flow conditions), the network continually reconfigures itself. The spatial pattern at any instant is "self-affine," that is, shows an anisotropic fractal

Paper number 98WR01697.
0043-1397/98/98WR-01697$09.00

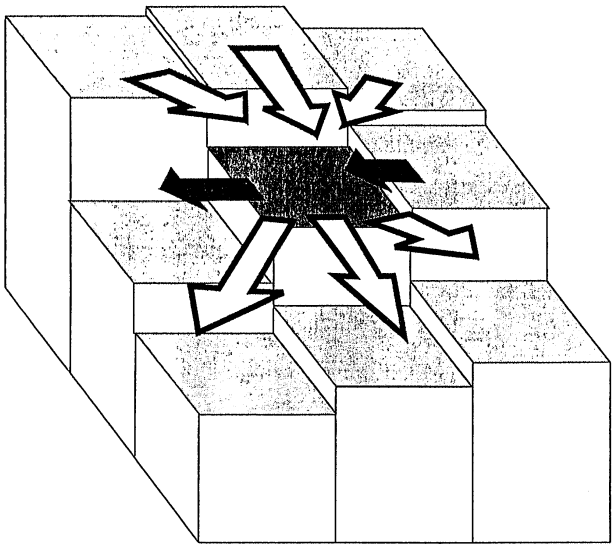

Figure 1. A schematic illustration of the rules in the cellular braided-stream model. Open arrows represent water routing and downstream sediment transport, and solid arrows represent the lateral-transport rule.

geometry in which patterns at different magnification scales are statistically similar within a consistent stretching of one spatial coordinate relative to the other. Like self-similar (isotropic) fractals, self-affine systems have a hierarchical geometric organization but no characteristic length scale (up to the scale of the whole system). The transition from an initial instability with a well-defined dominant wavelength to the final scale-free configuration is not well understood, but it may be analogous to the transition in fluids from an initial single-wavelength instability to the broadband distribution of eddies that characterizes fully developed turbulence [e.g., see *Tennekes and Lumley*, 1990].

The model developed by *Murray and Paola* [1994] is aimed not at predicting the conditions of formation of initial instabilities that might lead to braiding, but at the properties of the fully developed braided state. Hence model comparisons with initial bar wavelengths would not be very useful. Instead, model comparisons employing measures of spatial patterns and temporal dynamics would be more appropriate. Such measures, which include self-affinity in morphology, scaling behavior of island shapes, and dynamic scaling in spatiotemporal structure, capture information about the hierarchical space-time organization of the pattern: the relation of the whole to the parts of which it is made.

Another line of analysis is suggested by the fact that the flow of water down a river implies a preferred direction of causality. Under these conditions a spatial series is directly analogous to a time series, opening the possibility of applying the many techniques that have been developed for analysis of chaotic time series [*Weigend and Gershenfeld*, 1994; *Takens*, 1981; *Sauer et al.*, 1991; *Sugihara*, 1994]. Here the analysis aims to capture information about the sequential organization of the plan pattern: how the pattern at one point in space depends on the pattern upstream. We focus on spatial series of total flow width because they are readily measured from aerial photographs. Of course, total flow width is an aggregate measure of the morphology of a braided river, and as such it does not explicitly carry information about the relative position, shape, and distribution of widths of individual channels. This information, however, is explicitly incorporated in the self-affinity tests which look statistically at the detailed planform geometry of the braided patterns.

2. Summary of Cellular Model

In a cellular model, called a "coupled map lattice" by *Kaneko* [1993], the cells of a lattice interact according to simple rules meant to represent the basic physics of a system. Cellular automata models have found a wide application in the physical sciences [e.g., see *Vichniac*, 1984; *Toffoli*, 1984; *Salem and Wolfram*, 1986; *Frish et al.*, 1986], and such a model was proposed by *Murray and Paola* [1994, 1997]. Here we give only a brief overview of the model.

Elevations are defined for each cell in the lattice, initially forming an overall slope with random elevation perturbations which are the only random input into the model. At each iteration, water is introduced into cells at the uphill end of the lattice. From each cell the water is distributed to the three downstream immediate neighbor cells, with more water going where the bed slopes are steeper (Figure 1). A rule relates the amount of sediment transported from a cell to one of the three downstream neighbors, Q_{si}, to the local slopes and discharges. *Murray and Paola* [1994] have employed several sediment-transport rules, but here we will not consider rules that produce visually unrealistic patterns or contain terms that do not enhance the pattern's apparent realism. We will refer only to the rules called Q_s rules 3 and 4, respectively.

$$Q_{si} = K(Q_iS_i + Q_iC)^m \tag{1}$$

$$Q_{si} = K\left(Q_iS_i + \varepsilon \sum_j Q_jS_j\right)^m \tag{2}$$

where K is a constant and Q_i and S_i are the discharges and slopes from the cell in question to downstream neighbor i. In Q_s rule 3, C is a constant. In Q_s rule 4, ε is a constant, and Q_j and S_j refer to the discharges and slopes from the three upstream neighbors into the cell in question. Q_iS_i is the stream power index. The terms added to the stream power index in Q_s rules 3 and 4 allow sediment to be transported on locally flat or slightly uphill slopes, as occurs locally in real rivers, as long as water continues to flow downstream into the cell in question. On the basis of *Ashmore*'s [1985] compilation of data from laboratory and natural gravel bed rivers with a range of stream powers, we estimate that the whole river sediment transport varies as the reach-averaged stream power raised to an exponent of approximately 2.5. Although this does not apply strictly to the local treatment of sediment transport in the model, with the terms added to the stream power, we use 2.5 as a reasonable value for the exponent m. Model results do not depend sensitively on the value of m [*Murray and Paola*, 1997]. Another rule transports a small amount of sediment down transverse slopes (Figure 1) [*Murray and Paola*, 1994], representing the gravity-induced component of bedload sediment transport that occurs in real rivers when the bed slope is not parallel to the flow direction [*Blondeaux and Seminara*, 1985; *Parker*, 1978, 1984]. When the water reaches the downhill end of the lattice, the iteration ends, and the elevation of each cell is adjusted according to the difference between the amount of sediment entering and leaving that cell.

The output of the model is the distribution of water dis-

charge and bed topography over the lattice as a function of time. Both quantities can be measured in the laboratory, though only the general pattern of flow distribution (i.e., presence/absence) can be readily obtained from field aerial photographs. Sediment flux is also computed in the model, but since spatial distribution of sediment flux is difficult to measure in the field, we have not used it as a comparison variable.

3. State Space Approach

As discussed in section 1, one approach to evaluating the realism of a given model is to see how well it describes the sequential structure of real systems. In real braided rivers the geometry of the flow at one point affects the geometry that develops downstream. For example, where the flow is confined in a single narrow, deep channel, the sediment flux into downstream areas will likely be relatively large. This large flux enhances the likelihood that deposition and bed aggradation will occur where the channel next widens. Deposition often causes the flow to become wider and shallower. The downstream decrease in local flow strength heading into the shallow section encourages further deposition. Thus wide shallow flows and midchannel bars often occur directly downstream of narrow, deep sections in braided streams. If the processes in the model are similar to those in real braided streams, the downstream influences should be similar, leading to similar sequences of downstream changes in geometry.

We parameterize the geometry of braided streams by measuring total widths (the sum of the widths of all the channels in a cross section) for a long series of cross sections. (Other geometric variables could be used [*Murray and Paola*, 1996], but widths for many cross sections can be measured from aerial photographs. In addition, because it is the sequences of widths that are of interest, changes in stage should not affect the results strongly.) Constructing a spatial "state-space plot" by plotting each total width versus the previous width (or versus more than one previous width in higher-dimensional plots) encapsulates the information about the downstream changes in widths in that section of river (Figure 2). *Murray and Paola* [1996] described one method for quantitatively comparing state-space plots. Using this to compare plots representing model-generated and real patterns provides a measure of how realistic the model is. Here we improve on this approach in two ways. First, *Murray and Paola* [1996] used width data from two braided streams. Here we present data from an additional river which differs in characteristics such as slope and sediment type, providing a more reliable basis for comparison. Second, we apply a new method for quantitatively comparing state-space plots [*Moeckel and Murray*, 1997], which is more robust than the one applied previously.

3.1. Comparison Method

The technique of plotting each value in a time series versus some number of previous values is called "delay coordinate embedding" in dynamical-systems research [*Takens*, 1981; *Sauer et al.*, 1991]. As the system moves from one point in the plot, representing the current value and the recent past, to successive points, the system traces out a path through the state space. For a system that is deterministic and involves a small number of important variables, and yet displays complex and unpredictable behavior (a "chaotic" system), delay coordinate embedding is one way to depict the system's "attractor." An attractor is the manifold in state space (also called "phase space") that the system moves on as its long-term behavior is plotted. Superficially different time series from the same system will trace out very similar patterns, which depict the sequences of changes the system exhibits. To produce an accurate representation of the attractor, the plot must be of sufficiently high dimension; each point must represent enough previous values to uniquely determine the next value and therefore the next point. This means that in such a plot of a deterministic system, lines connecting successive points will not cross.

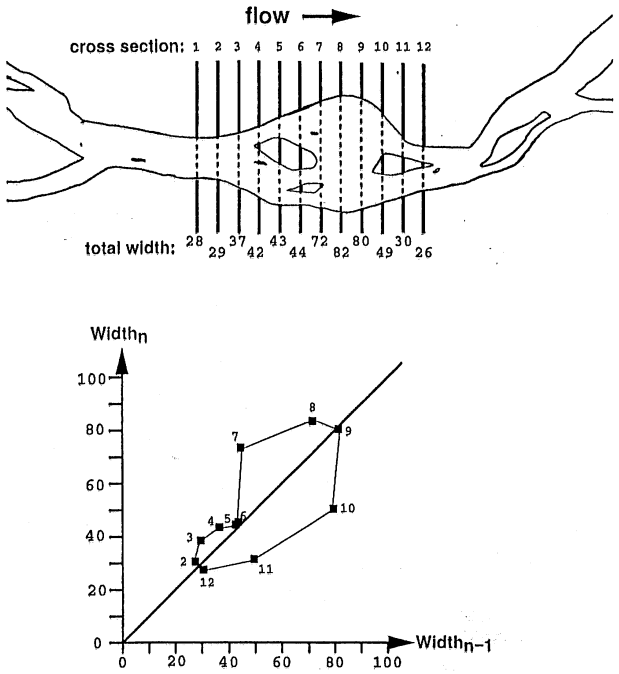

Figure 2. An illustration of how a two-dimensional state-space plot is constructed from a series of total widths. Total widths are the sum of the widths of all the channels in a cross section. A width greater than the previous width plots above the diagonal and vice versa. The magnitude of the difference between the two widths determines how far from the diagonal the point falls.

Plotting a spatial series of braided-stream total widths using delay-coordinate embedding in two or three dimensions produces patterns with lines that often cross (Figure 3). In other words, the downstream influences are not deterministic in these few dimensions; a sequence of three total widths is not enough information to uniquely determine the next width. This system may appear more deterministic in higher dimensions, or it may include some stochastic behavior. However, the method we use for quantitatively comparing state-space plots does not require that the system be plotted in the proper dimensions or that it be deterministic; the plots are not assumed to depict attractors. This method treats state-space plots as probability distributions, comparing the frequency with which typical sequences occur. In this context, the state-space–plot comparison method does not require that a given sequence of total widths is always followed by the same width. This method provides a useful way to compare spatial series of widths as long as there is enough downstream influence to produce typical series of widths rather than completely random series.

In the first step of this method, state-space plots are trans-

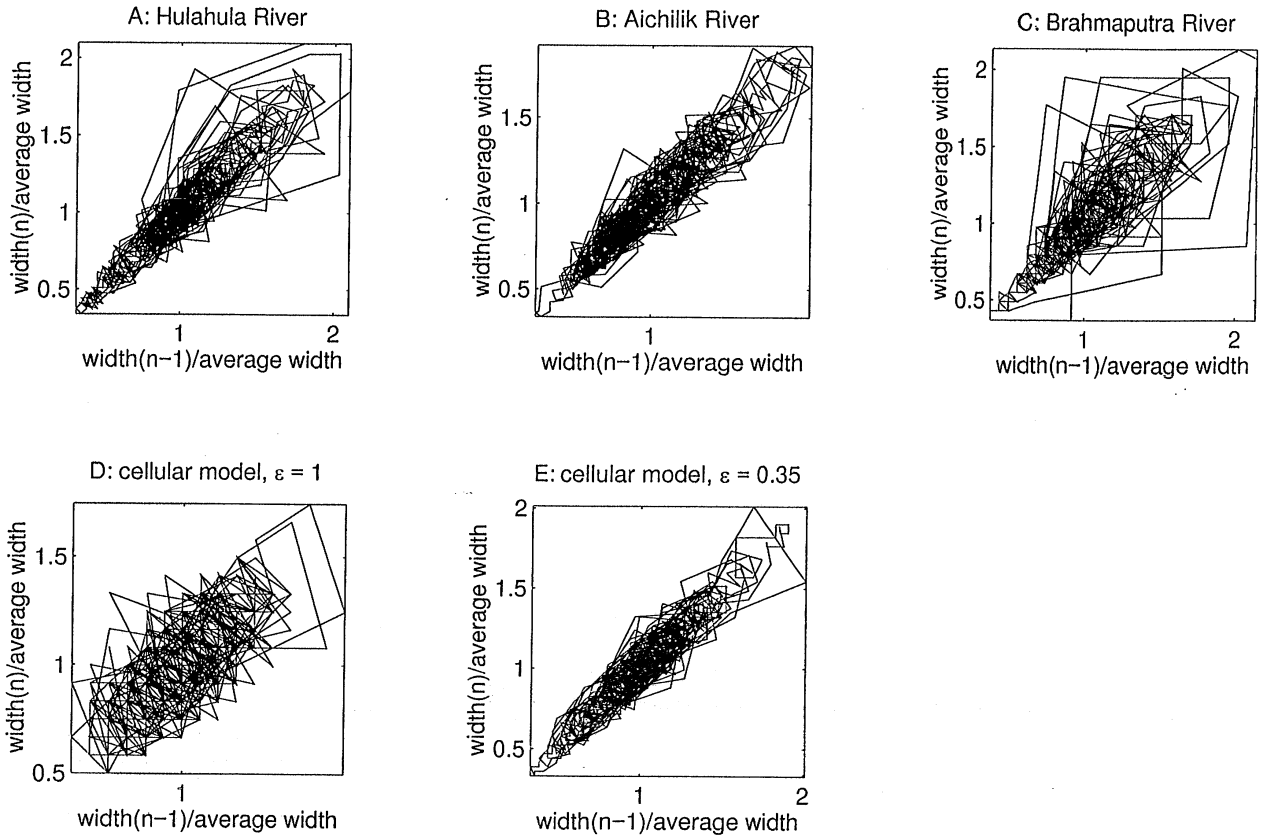

Figure 3. State-space plots of total-width series from (Figures 3a–3c) real rivers and (Figures 3d and 3e) the model runs. Each data set is normalized to the average total width for the reach measured.

formed into discrete probability distributions by dividing the state space into cells and assigning a probability to each cell that is equal to the number of points in that cell normalized by the total number of points in the plot. Then an algorithm finds the minimum average distance that the elements of one discretized distribution must be moved to duplicate the other distribution (Figure 4). The distance is given in the units in which the series are expressed. This metric was proposed originally by Kantorovich as an optimal solution of transportation problems and was later applied in the probability literature [*Dudley*, 1989]. *Hutchinson* [1981] used a related function in connection with iterated function systems. *Moeckel and Murray* [1997] adapted the theoretical metric into a practical comparison between discretized probability distributions. The probabilistic and geometric properties of this "transportation distance" give it advantages over other commonly used metrics for assessing how similar the arrangements of probability in two distributions are, which represents in this case how similar the typical sequences in two series are. For example, the transport distance is relatively insensitive to outliers, especially when compared to the Hausdorff distance [*Moeckel and Murray*, 1997]. In addition, if corresponding areas of high probability do not fall in quite the same state-space location in two distributions, the transport distance's geometric properties make it sensitive to how far apart the two areas are. In contrast, the Kolmogorov metric does not directly measure such differences [*Dudley*, 1976]. The transportation distance is much less sensitive to the cell sizes used in the discretization of the state space, and to perturbations in the series, than is the method used by *Murray and Paola* [1996] in the preliminary test of the braided-stream model [*Moeckel and Murray*, 1997].

3.2. Similar Plots From Different Kinds of Braided Streams

Measuring a long series of widths under uniform conditions requires a long reach of a river without tributaries, topographic

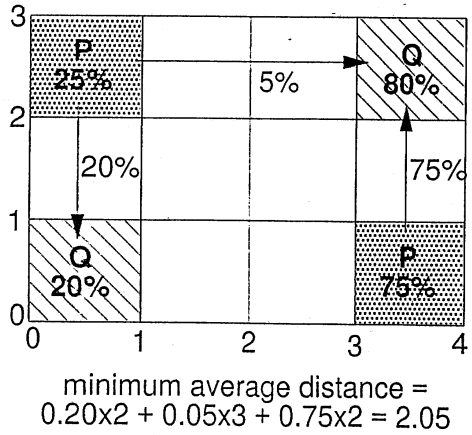

Figure 4. A simple illustration of the transportation distance between the discretized probability distributions P and Q. Numbers next to arrows show how much probability is transported in each step of transforming P into Q. If the distributions overlapped in some cells. the total of these numbers would be less than 100%.

obstacles, changes in slope, or changes in grain size. We have found such reaches on two gravel-bed braided rivers, the Aichilik and Hulahula Rivers on the North Slope of the Brooks Range in Alaska, and on one sand-bed river, the Brahmaputra River in Bangladesh. On the gravel rivers, measurements of surface grain size, using the method of *Wolman* [1954], show no significant downstream grain-size changes on the gravel-bed rivers (for Aichilik data, see *Murray and Paola* [1996]). We have not performed any field studies of the Brahmaputra. We also use data from a laboratory-scale braided stream that exhibits Froude number similarity to a gravel-bed braided river. We traced the discharge pattern of the Brahmaputra from a satellite image that had a poorer resolution relative to the river's size than the aerial photographs used for the other two rivers or the overhead photographs used for the laboratory stream. As a result, the smallest channels in the Brahmaputra were not traced.

These braided streams differ greatly in relative grain size, slope, and scale of flow (Table 1). One might expect that such different streams would have fundamentally different patterns (patterns that had very different typical downstream sequences of total widths, for instance). However, Figures 3a–3c show that all the plots of each total width versus the previous width are quite similar. Widths are normalized to units of the average total width $\overline{w_T}$ for each river, and cross sections have approximately the same relative spacing for each river (0.08 $\overline{w_T}$). Some of the details of these plots differ, especially in the presence or absence of a few wide loops, which show occasional abrupt downstream width changes. However, the areas where the data are dense in these plots are similar, indicating similar typical sequences of widths. A plot with these characteristics is not inevitable for any braided pattern; Figure 3d shows the results of a run of the braided-stream model that produces a braided pattern that does not result in a plot like those for the real streams. For instance, this plot extends farther from the diagonal in the lower left, indicating more abrupt downstream width changes when the width is relatively small. In addition, the model plot does not extend as far along the diagonal, reflecting a smaller variance in the widths.

Because the geometry at one cross section influences the geometry at successive sections via the mechanisms of flow and sediment transport, the similar sequences of widths shown by the plots in Figures 3a–3c suggest that fundamentally similar mechanisms operate in all these braided streams. Perhaps the large-scale interactions between flow and sediment are insensitive to the differences in relative grain size and flow characteristics among these streams. The state-space plots of downstream changes in width summarize what appears to be a robust, important aspect of real braided-stream patterns that can be used as a basis for model comparison.

Table 1. Hydrologic and Geomorphologic Characteristics of Brahmaputra, Aichilik, Hulahula, and Tanana Rivers

	Brahmaputra	Aichilik	Hulahula	Tanana
Reach width, km	15	0.5	0.7	1.8
Reach length, km	200	6.4	20	28.6
Mean channel depth, m	5	1	1	—
Slope	0.000077	0.001	0.0007	0.001
Braiding index*	3.8	6.8	5.2	4.6
Predominant type of the bedload	sand	gravel	gravel	gravel + sand
Fractal exponent ν_x	0.74	0.72	0.74	0.70–0.77†
Fractal exponent ν_z	0.51	0.51	0.52	0.47–0.50

*The braiding index (BI) for each river was computed as the average number of channels in cross sections of the photo image of the river.
†The fractal exponents for the Tanana River were estimated at three different times (different stages of the river).

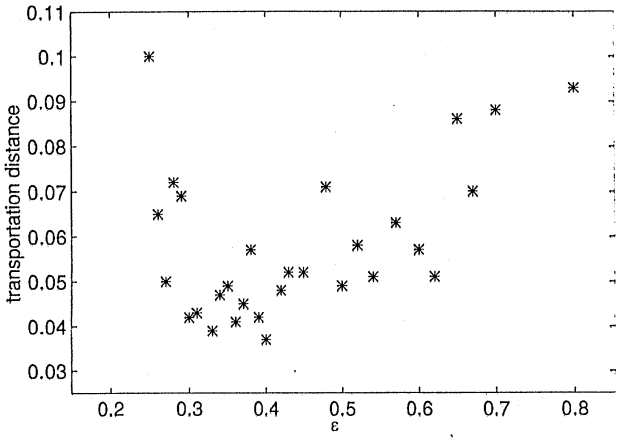

Figure 5. Transportation distances between the probability distribution representing the Hulahula River and those representing model runs with different values of ε in Q_s rule 4. Each point is an average over two to four snapshots of the model. The braid plain is 46 × 1000 cells in each run. (In section 3 we discuss the fact that some aspects of the model patterns using this sediment-discharge rule appear not to reach steady state until ~100,000 iterations. In this experiment we used snapshots from 20,000–65,000 iterations. However, in these runs, discharge is introduced in each cell in the first row, rather than in one fourth of the cells as in all the other model runs we discuss. The relatively larger discharge means that more material is moved each iteration, so that the patterns develop faster [see *Murray and Paola*, 1994]. In addition, larger values of ε mean that more material is transported in each iteration. We used snapshots from as few as 20,000 iterations only in the largest-ε runs.)

3.3. Quantitative Model Evaluations

Moeckel and Murray [1997] demonstrated that the transportation distance method of comparing state-space plots can be used to find the optimal value of an unconstrained model parameter. The term that allows sediment transport on flat and slightly uphill surfaces in Q_s rule 3 is physically motivated; flow momentum and therefore sediment transport should increase with increasing slopes and discharges into an area. However, the magnitude of this term, determined by ε, is only loosely constrained [*Murray and Paola*, 1994]. Figure 5 shows how the model realism varies with ε. Realism is measured here by the transportation distances between the state-space plot representing the Hulahula River and the plots representing the model. We show the results using the Hulahula data because it is the longest of our data sets (the longest reach, in units of the average total width, with uniform conditions), but experiments using other data sets show very similar results. Widths in the model are the number of cells in a cross section with discharge greater than a cutoff, which is 0.35% of the total discharge in these runs. Each data point in Figure 5 represents an average over two to four snapshots between 30,000 and 50,000 itera-

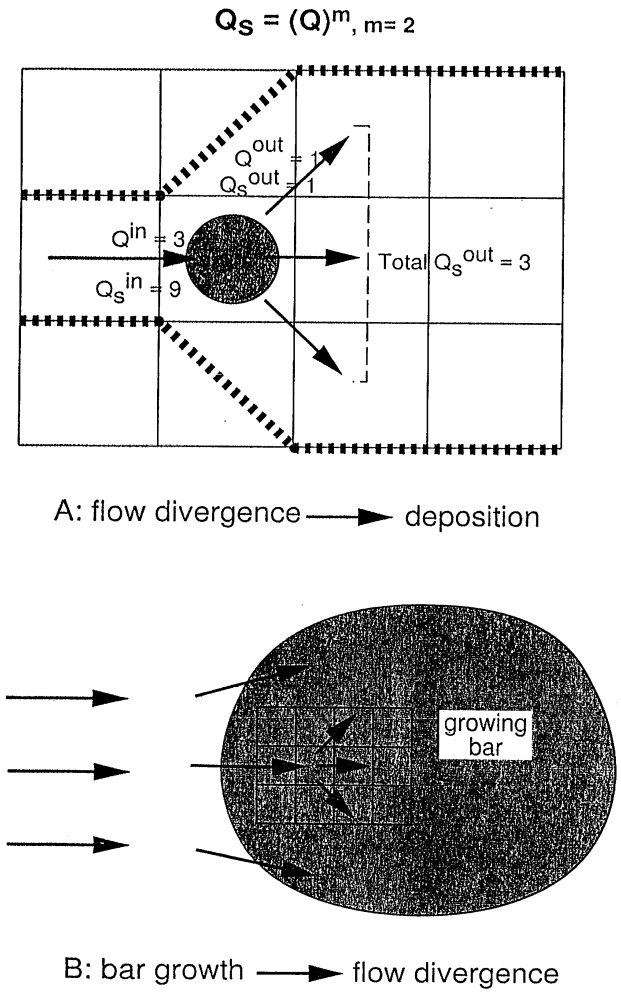

Figure 6. Schematic illustration of the effects of the nonlinear dependence of sediment transport on discharge in the model. For simplicity, in Figure 6a the slopes are assumed to be constant, so that the discharge spreads evenly into the downstream cells at the divergence. In this case, sediment transport is proportional to discharge raised to the power of m for either Q_s rule 3 or 4. We use $m = 2$ and a constant of proportionality of 1 for further simplicity. Figure 6b illustrates how a growing bar causes flow divergence and therefore a situation similar to that depicted in Figure 6a.

tions, with lattice dimensions of 1000 × 46 cells. The transportation distance reaches a minimum at a value of ε 0.3–0.4.

Figures 3a–3c and 3e show that the state-space plot of a model run using this value of ε shares the main characteristics of the plots of the real rivers. In the model the mechanism that is most essential to produce braiding is the nonlinear dependence of sediment transport on flow strength, specifically discharge, with the exponent $m > 1$ in the Q_s rule [*Murray and Paola*, 1994]. With this relationship, flow divergences tend to produce convergence in the sediment flux and therefore local deposition. Figure 6 illustrates this for a simple case and shows how the feedback of deposition enhancing flow divergence can lead to bar formation. The nonlinear relationship also causes the opposite instability: flow convergence tends to produce erosion and bed lowering, which enhances flow convergence at that location. The slope dependence of the stream power tends to oppose these instabilities. For example, it decreases the amount of sediment transported across the reduced or negative slopes out of low areas and onto barheads. The term that allows sediment transport over flat or slightly uphill slopes partially offsets this effect in the model, making it easier for sediment to move from a deep (and therefore usually narrow) section into an area of flow divergence and bar formation. We suggest that these large-scale mechanisms are also the most important processes in real braided streams, leading to the similarity in the downstream changes in width between real rivers and the model.

Table 2 shows, for each of several model images, the average transportation distance between that image and each of the three natural rivers. (The laboratory-stream data set has fewer points than any of the real-river data sets, so we leave it out of this analysis.) Seven of these model snapshots are from two different runs that used Q_s rule 4 with the optimal ε value (0.35). (These runs differed in the side boundary conditions: Q_s rule 4 run B had erodible banks between the braid plain and high side walls. These banks were not present in Q_s rule 4 run A. The braid plains in both runs spanned 1500 × 100 cells.) The transportation distances in Table 2 are slightly lower than the minimum shown in Figure 5 because for these images we traced the model output in the same way as we did for the natural patterns. Rather than automatically measuring the total width as the number of cells in a cross section with discharge above a cutoff, we applied the same standards to model patterns that we applied when tracing the real-river patterns. For instance, noncontinuous channels were not included in the patterns. The mean value of the transportation distance between real-river plots and all the images produced with Q_s rule 4 is 0.038, with a standard deviation of 0.014, in units of average total width.

Quantitatively assessing how realistic the width sequences in the model are requires a benchmark to judge this mean against. Table 3 lists the transportation distances between plots representing the three natural rivers. These distances measure the variability in typical sequences not only between different realizations of natural rivers but also between different types of natural rivers. The model is too simple to be a simulation of one of the types of rivers specifically; there is no explicit grain size or slope, for example [*Murray and Paola*, 1997]. The best that could be hoped for is that the plots representing model patterns match those representing real rivers as closely on average as the real-river plots match each other. The average distance between real-river plots is 0.026, with a standard deviation of 0.003 (Table 3). The difference between this value and the average transportation distances between model plots and real rivers (Table 2) suggests that the model does not always match the real rivers as closely as real rivers match each other. Although the sizes of the data sets are smaller than would be desired for a rigorous statistical treatment, we applied a two-sample Welch's t test, which measures the likelihood that two groups of numbers could really be derived from the same population, given the means, standard deviations, and number of samples in each group [*Miller*, 1986]. This test indicates that there is less than a 0.1% probability that the difference between the two means is not meaningful. This number should not be considered exact, because the assumption behind the test, that the underlying populations from which the samples are drawn are normally distributed, has not been proven to be valid. However, slight deviations from normality are unlikely to alter the basic conclusion that the model

Table 2. Transportation Distances Between Model and Real-River Plots and Scaling Statistics of Model Images

Model Image	Transportation Distances				Scaling Characteristics	
	Hulahula	Aichilik	Brahmaputra	Average	ν_x/ν_y	D
Q_s rule 3 87,000 iterations	0.044	0.029	0.039	0.034	1.55	1.50
Q_s rule 3 90,000 iterations	0.033	0.025	0.035	0.031	1.46	1.47
Q_s rule 3 138,000 iterations	0.034	0.027	0.040	0.035	1.95	1.62
Q_s rule 3 145,000 iterations	0.045	0.034	0.038	0.038	1.65	1.69
Q_s rule 4, run A 61,000 iterations	0.021	0.018	0.050	0.029	...	1.48
Q_s rule 4, run A 105,000 iterations	0.070	0.052	0.054	0.057	1.63	1.57
Q_s rule 4, run A 169,000 iterations	0.043	0.034	0.048	0.038	1.44	1.53
Q_s rule 4, run B 91,000 iterations	0.034	0.016	0.034	0.028	...	1.57
Q_s rule 4, run B 134,000 iterations	0.034	0.029	0.042	0.033	1.39	1.60
Q_s rule 4, run B 172,000 iterations	0.030	0.040	0.059	0.044	...	1.78
Q_s rule 4, run B 181,000 iterations	0.023	0.022	0.043	0.030	1.88	1.74

Run B had erodable banks between the braid plain and high side walls. These banks were not present in run A.

is probably not completely realistic. This is not surprising given the simplicity of the model.

Murray and Paola's [1996] preliminary analysis suggested that runs using Q_s rule 3 produced patterns with width sequences that were less realistic than those produced with Q_s rule 4. However, using the transportation-distance method of comparing state-space plots and the larger number of real-river data sets, Q_s rule 3 patterns match the real rivers at least as well as the Q_s rule 4 patterns do, on average; the average distance between plots representing these patterns and those representing real rivers is 0.035, with a standard deviation of 0.006 (Table 2). Applied to the mean for Q_s rule 3 patterns, the two-sample t test gives a <0.1% chance that this mean could be found for a sample of this size of the within-real-river population.

State-space plots of total widths characterize an important aspect of braided-stream patterns. However, this approach is not sensitive to the arrangement or number of channels. Section 4 addresses the realism of these aspects of the model patterns by analyzing self-affine scaling properties and channel shapes.

4. Self-Affine Scaling Approach

In a recent study, *Sapozhnikov and Foufoula-Georgiou* [1996] examined the spatial patterns of three natural braided rivers (aerial images of the Aichilik and Hulahula Rivers in Alaska and the satellite images of Brahmaputra River in Bangladesh)

Table 3. Transportation Distances Between Real-River State-Space Plots

River	Aichilik	Brahmaputra
Hulahula	0.022	0.030
Aichilik	...	0.027

and found that they exhibit anisotropic scaling (self-affinity). Similar results were obtained more recently for the Tanana River in Alaska using synthetic aperture radar (SAR) data [*Nykanen et al.*, 1998]. Self-affinity in a braided river implies that if a small part of the braided river is stretched differently in the direction of the river slope and in the perpendicular direction, then the stretched part looks statistically similar to a larger part of the braided river. Despite the large differences in scales (0.5–15 km), slopes (7×10^{-3} to 8×10^{-5}), and bed material (gravel to sand) the four analyzed braided rivers showed very similar spatial scaling with self-affine fractal exponents $\nu_x = 0.72$–0.77 and $\nu_y = 0.47$–0.52. This may indicate the presence of universal features in the underlying mechanisms responsible for the formation of the spatial structure of braided rivers. It is important to see whether self-affinity found in natural rivers is reproduced by a braided river model. The logarithmic correlation integral (LCI) method developed by *Sapozhnikov and Foufoula-Georgiou* [1995] enables one to test the presence of self-affinity in braided rivers and estimate the scaling exponents ν_x and ν_y. In section 4.1 a brief review of this method is presented followed by the results of self-affine analysis of natural and model-produced braided rivers. Then some additional properties of spatial patterns of braided rivers, such as island shapes, are evaluated and compared for natural and model-produced rivers.

4.1. The LCI Method for the Analysis of the Correlation Structure of Self-Affine Objects

The LCI method to test and quantitatively assess the presence of self-affinity in complex geometrical patterns, such as braided rivers, is based on the correlation integral function $M(X, Y)$, which measures the mass of an object within a rectangle (centered around a point of the object) of size $X \times Y$. For a self-affine object,

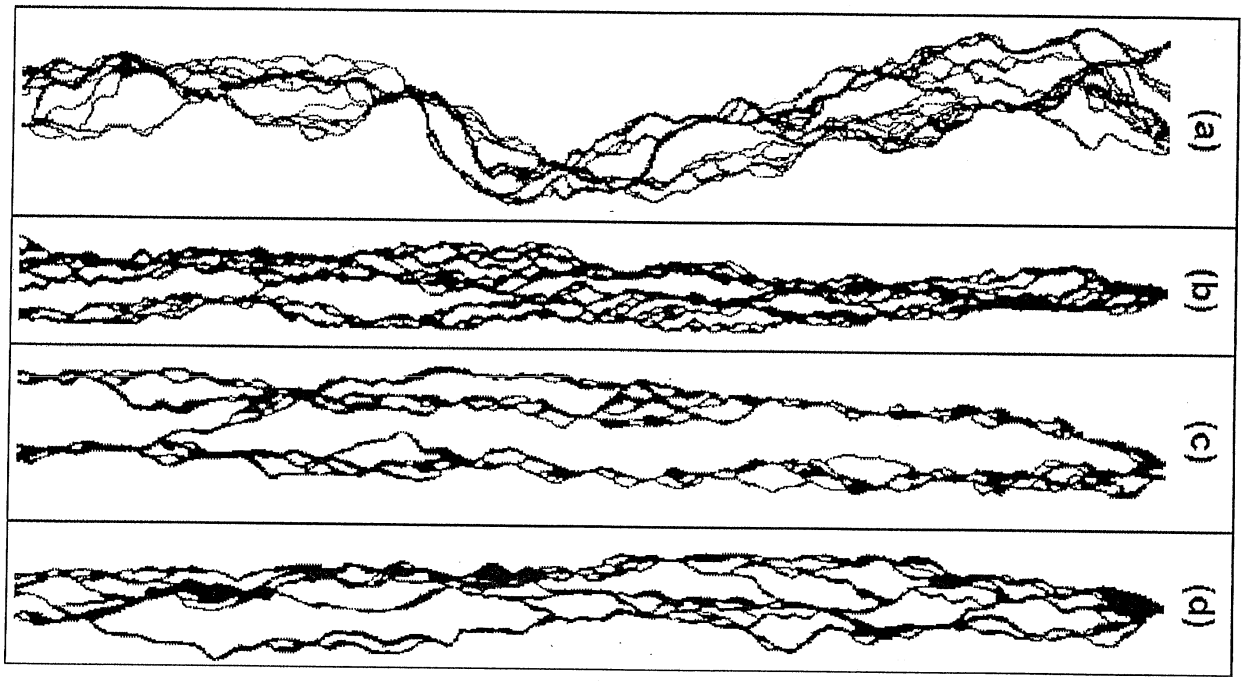

Figure 7. Digitized images of the (a) Aichilik River, (b) Q_s rule 3 model river (145,000 iterations), (c) Q_s rule 4 model river (61,000 iterations), and (d) Q_s rule 4 model river (105,000 iterations).

$$M(X, Y) \propto X^{1/\nu_x} \propto Y^{1/\nu_y} \tag{3}$$

where ν_x and ν_y are called the fractal exponents. *Sapozhnikov and Foufoula-Georgiou* [1995] showed that the function $z(x, y) = \log(M(X, Y))$, where $x = \log(X)$ and $y = \log(Y)$, satisfies the equation

$$\nu_x \frac{\partial z}{\partial x} + \nu_y \frac{\partial z}{\partial y} = 1 \tag{4}$$

and thus provides the means to test the presence of self-affinity in an object and estimate its fractal exponents ν_x and ν_y. Indeed, having a pattern of an object, one can estimate its logarithmic correlation integral $z(x, y)$ and use the derivatives $\partial z(x, y)/\partial x$ and $\partial z(x, y)/\partial y$ to find the values of ν_x and ν_y that satisfy (4), by a least squares method. The function $z(x, y)$ was called the logarithmic correlation integral (LCI) function, and the method was called the LCI method.

4.2. Self-Affine Scaling in Natural Braided Rivers

Application of the LCI method to the Brahmaputra, Aichilik, and Hulahula Rivers showed that (4) is satisfied for all three rivers fairly well, giving ν_x and ν_y values summarized in Table 1 together with other physical characteristics of these rivers [*Sapozhnikov and Foufoula-Georgiou*, 1996]. Interestingly, it was observed that despite the large differences in the scales of these rivers and their hydrologic properties, they all exhibited anisotropic scaling with almost the same fractal exponents ($\nu_x \simeq 0.72$ and $\nu_y \simeq 0.51$; X indicating the mainstream direction and Y the perpendicular one). This implies that if parts of a braided river are stretched by λ along the mainstream direction and by $\lambda^{\nu_y/\nu_x} \simeq \lambda^{0.7}$ along the perpendicular direction, the resulting images will look statistically similar to the each other (similarity within a braided river). At the same time, the invariance of ν_x and ν_y between braided rivers of different sizes and hydrology/sedimentology suggests that the same anisotropic scaling as above, applied to different rivers, will result in statistically similar images, except possibly for a normalization factor to account for the different mass of each river. Such scale invariances across a range of scales, apart from being interesting in their own right, have several fundamental implications. First, they may indicate the presence of universal features in the underlying mechanisms responsible for the spatial structure of braided rivers and suggest that this structure is due to the self-organizing nature of the flow and sediment flux rather than to specific local external influences and scale. Second, knowledge of which geometric attributes are scale invariant or scale dependent is useful when applying models of braided alluvial architecture deduced from one system to another of a completely different size. Finally, since these scale invariances are properties of real braided rivers, they should also be reproduced by any model of braided river that tries to simulate realistic braided-river patterns.

4.3. Self-Affinity in the Model Braided Rivers

Braided rivers manifest salient features of their spatial structure at scales where branching comes into play, that is, scales smaller than the braid plain width. Therefore, similarly to the previous study of natural braided rivers by *Sapozhnikov and Foufoula-Georgiou* [1996], we focused on scales smaller than the braid plain width. We used the traced discharge patterns of the modeled river (and not just the patterns formed by the cells with a discharge above some threshold), similarly to the previous analysis of natural rivers and in agreement with the dynamical-systems analysis of the model performed in this work where traced images have been used.

First, a traditional fractal analysis was applied. For example, the dependence of the "mass" M (number of nonempty cells) within a square box of size R, $(M(R))$ for the river produced by the model using Q_s rule 4 (Figure 7d) is presented in Figure

8 in log-log scale. The dependence follows a straight line up to the scale of the width of the river, with a slope of 1.57. Similar analysis was applied to several runs of the model (Q_s rule 3 and Q_s rule 4). It showed that the rivers exhibit fractal behavior up to the scale of their width, with fractal dimensions D = 1.5–1.7 for Q_s rule 3 and D = 1.5–1.75 for Q_s rule 4. The values of the fractal dimensions agree with the results of *Sapozhnikov and Foufoula-Georgiou* [1996], who found fractal dimension D = 1.5–1.6 for three natural rivers (Aichilik, Hulahula, and Brahmaputra), *Nykanen et al.* [1998], who found D = 1.5–1.6 for different stages of Tanana, and *Nikora et al.* [1995], who found D = 1.5–1.7 for several New Zealand braided rivers.

However, this traditional fractal analysis does not show whether the object is self-similar or self-affine. Indeed, as demonstrated by *Sapozhnikov and Foufoula-Georgiou* [1995, 1996], self-affine objects (i.e., objects with scaling anisotropy) can still show linear log-log dependence $M(R)$, with slope D, which is the global fractal dimension of the self-affine object related to ν_x and ν_y as $D_G = (\nu_y - \nu_x + 1)/\nu_y$. Applying the LCI method, however, not only enabled us to study the model rivers for scaling anisotropy but also revealed other important features of the spatial structure of the rivers.

To find the fractal exponents of the model rivers, we first estimated their logarithmic correlation integrals $z(x, y)$ from the patterns of the rivers. The X axis was oriented along the slope. From the correlation integral surfaces $z(x, y)$ we calculated numerically the derivatives $\partial z(x, y)/\partial x$ and $\partial z(x, y)/\partial y$ and plotted the dependencies $\partial z(x, y)/\partial y$ versus $\partial z(x, y)/\partial x$. Figure 9 presents these dependencies for the Aichilik River [see *Sapozhnikov and Foufoula-Georgiou*, 1996], the model river using Q_s rule 4 after 61,000 iterations and the same model river after 105,000 iterations.

Let us first consider the dependence for the Aichilik River. As was shown by *Sapozhnikov and Foufoula-Georgiou* [1996],

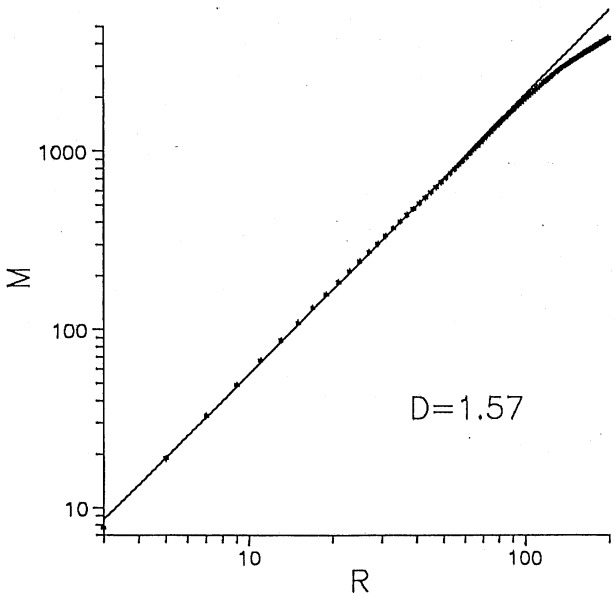

Figure 8. Spatial scaling in the Q_s rule 4, 105,000 iterations model-produced braided river indicated by the straight line log-log dependence of the "mass" M (number of nonempty cells) on the size R of the covering square box. The slope of the straight line gives the value of the fractal dimension D.

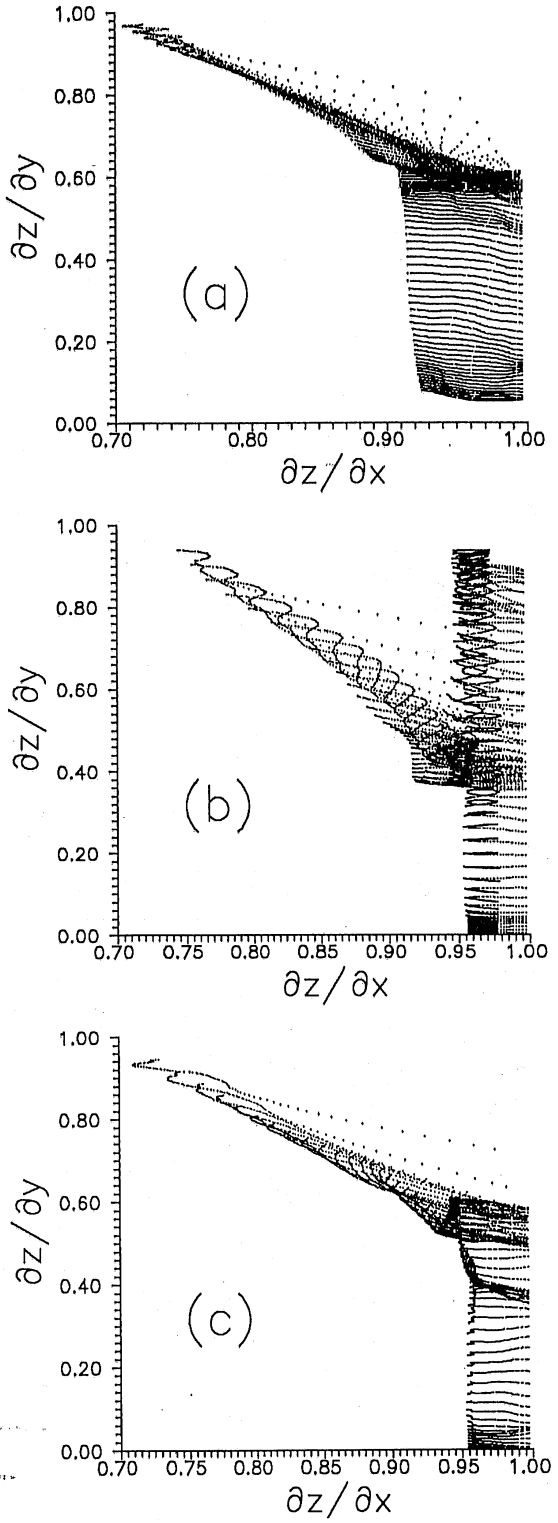

Figure 9. Dependence $\partial z(x, y)/\partial y$ versus $\partial z(x, y)/\partial x$ for (a) the Aichilik river, (b) the Q_s rule 4, 61,000 iterations model-produced river, and (c) the Q_s rule 4, 105,000 iterations model-produced river. The partial derivatives are estimated from the entire correlation integral surfaces $z(x, y)$ of the rivers.

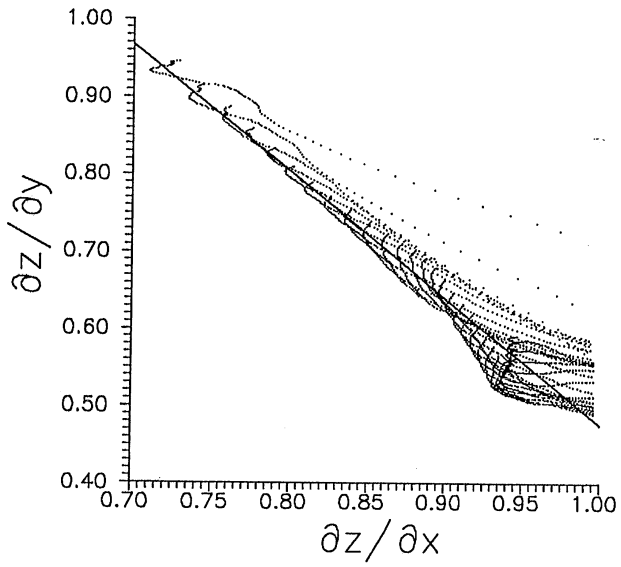

Figure 10. Estimation of the fractal exponents ν_x and ν_y for the Q_s rule 4 long run model produced river from the truncated part of the $z(x, y)$ surfaces (see text). The estimated values are $\nu_x = 0.77$ and $\nu_y = 0.47$.

the upper, linear part of the plot in Figure 9a comes from the scales up to the width of the river and indicates self-affinity in this range of scales (see equation (4)), whereas the lower part indicates a scaling break and comes from the scales exceeding the river width (similar to the scaling break in Figure 8 indicated by the deviation from the straight lines for large scales). Comparing the partial derivative plots in Figure 9, one can see that while the longer (105,000 iterations) run gives a plot quite similar to the Aichilik River (it is also similar to the plots for Brahmaputra and Hulahula shown by *Sapozhnikov and Foufoula-Georgiou* [1996]), the shorter (i.e., having undergone fewer iterations) run looks different: It has the scaling break area extending not only below but also above the log-log straight line in the plot (this feature is called here a "hat"). Similar behavior (having the "hat" appearing early in the model run and then disappearing) was observed in other model runs too. Our analysis showed that the "hat" comes from a peculiar feature of the model river at early stages: The channels tend to be parallel to each other and do not often converge. This makes the $z(x, y)$ function gain a significant magnitude at the value of y equal to the distance between the parallel channels, which leads to the high values of the partial derivatives $\partial z(x, y)/\partial y$ and forms the "hat." A close look at the pattern of the model river at the early stage (Figure 7c) confirms this conclusion. Given enough time, the model rivers evolved into a state that did not have this feature and thus became closer to natural rivers. It should be mentioned that rivers produced by Q_s rule 4 needed more time to develop the "realistic" (corresponding to natural rivers) pattern than the rivers produced by Q_s rule 3.

We then studied the linear part of the dependencies $\partial z(x, y)/\partial y$ versus $\partial z(x, y)/\partial x$ for model rivers. To check if the points in the plot where the linearity breaks come from the range of scales exceeding the river width, we cut off the part of the $z(x, y)$ surface corresponding to Y values higher than the width of the model river. Figure 10 shows the values of the partial derivatives coming from the rest of the $z(x, y)$ function for the model river produced by Q_s rule 4 after 105,000 iterations. The points show a good linear dependence, indicating that the river exhibits spatial scaling within the scale of its width. Similar analysis was performed for other runs and for Q_s rule 3. All revealed spatial scaling up to the scales of the width of each river. Using (4), the values of the fractal exponents were found to be $\nu_x = 0.72$–0.78 and $\nu_y = 0.40$–0.54 for Q_s rule 3 and $\nu_x = 0.75$–0.97 and $\nu_y = 0.47$–0.52 for Q_s rule 4. The scaling anisotropy was $\nu_x/\nu_y = 1.46$–1.95 for Q_s rule 3 and $\nu_x/\nu_y = 1.44$–1.88 for Q_s rule 4. These results imply that the model rivers are self-affine objects showing a high degree of anisotropy.

One can see that while the fractal dimension of the model rivers is close to that of the studied natural rivers, the anisotropy parameter ν_x/ν_y is on the average higher for the modeled rivers (1.44–1.95 versus 1.41–1.60 for the four studied natural rivers). It should be noted that the spread of the scaling parameters is higher in modeled rivers (especially for Q_s rule 4) than for natural rivers.

4.4. Island Shape Comparison

The LCI method reveals the scaling anisotropy of an object as a whole. Here we also studied the sizes of islands in the modeled rivers for scaling anisotropy. The size of each island in the direction of the slope, l_x, and in the perpendicular direction, l_y, was estimated as the root-mean-square of the deviation (in the corresponding direction) of pixels constituting the island from the center of mass of the island: $l_x = [(1/n)\Sigma_{i=1}^{n}(\bar{X} - X_i)^2]^{1/2}$ and $l_y = [(1/n)\Sigma_{i=1}^{n}(\bar{Y} - Y_i)^2]^{1/2}$, where n is the number of pixels in the island. Figure 11 shows the log-log plot of the sizes of the islands l_x and l_y in the X and Y directions, respectively, for the model river produced using Q_s rule 4 and after 105,000 iterations. The log-log linearity of the l_y versus l_x dependence indicates scaling. The slope of the log-log linear dependence is equal to 1.35. The fact that the slope is different from 1 indicates anisotropy in scaling of the islands in X and Y directions. The analysis of islands for scaling was performed for other runs of the model (both Q_s-rule 3 and

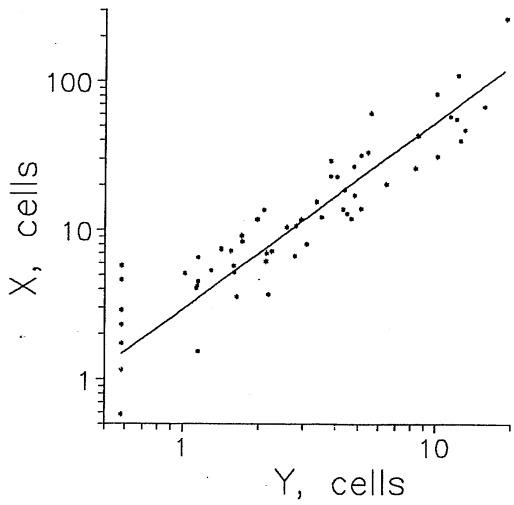

Figure 11. Scaling in the projections of the islands on the X and Y axes in the Q_s-rule 4, 105,000 iterations model produced river. The estimated value of the slope is 1.35, which is different from 1 indicating scaling anisotropy.

Q_s-rule 4). In all cases, anisotropic scaling of islands was found.

It should be noted that the scaling anisotropy of the islands was 10–20% lower than the scaling anisotropy of the modeled rivers as a whole obtained by the LCI method. This is in agreement with the results obtained previously by *Sapozhnikov and Foufoula-Georgiou* [1996] for natural rivers, where the scaling anisotropy of the sizes of islands in a river was also found to be 10–20% lower than the anisotropy of the river as a whole. In our opinion this difference implies that the scaling anisotropy of a braided river is only partially reflected by the anisotropy of islands. Part of the anisotropy in a braided river stems from the anisotropy in tortuosity of the river (same as anisotropy in tortuosity of single-channel rivers causing their scaling anisotropy). These two factors exist on scales that overlap and therefore cannot be separated.

5. Discussion and Conclusions

The state-space and the scaling analyses proposed here for braided river model validation complement each other. Indeed, the state-space analysis characterizes the river pattern in the dynamical-system theory framework, enabling one to follow how the total width of the river changes downstream. For example, the state-space analysis easily distinguishes sudden changes in the river width from gradual ones. Moreover, it shows whether abrupt or gradual changes occur more frequently in narrow or in wide sections: For example, compare the state-space plot of the Hulahula River (Figure 3a), showing abrupt changes (big loops) only in wide sections of the river, with the state-space plot of a run of the model river (Figure 3d), showing abrupt changes in both narrow and wide sections. The scaling analysis via the logarithmic correlation integral (LCI) method, on the other hand, characterizes correlation properties of the multiscale spatial structure of a braided river in different directions and reveals anisotropic scaling (self-affinity) in the river, something which the state-space analysis was not designed for. Besides, the state-space-plot method uses the total width at each cross section of the river. Therefore it does not include information of the width, shape, and relative position of the individual channels. These important characteristics of a braided river are reflected in the correlation structure of the river and captured by the LCI analysis. In fact, as we demonstrated in this article, the analysis of the correlation structure of braided rivers by the LCI method discloses subtle differences between the structure of the simulated and natural river patterns (such as, for example, the fact that channels of the modeled rivers tend to be more parallel at early stages of the model runs than at later stages and in natural rivers (see Figure 9)). Together the two methods provide a fairly comprehensive approach to testing how realistic a model-produced river pattern is. They reveal and quantify subtle characteristics of the river pattern, and thus they permit testing a model and determining the most realistic rules and parameters of that model.

The analysis of the modeled rivers using the cellular model of *Murray and Paola* [1994] showed that they eventually develop into a state exhibiting anisotropic spatial scaling (self-affinity). This is in agreement with the results of the analysis of natural braided rivers presented by *Sapozhnikov and Foufoula-Georgiou* [1996]. The presence of spatial scaling in natural braided rivers (which implies absence of a preferred scale) was interpreted by *Sapozhnikov and Foufoula-Georgiou* [1996] as a strong indication that the same physical mechanisms are responsible for the formation of braided pattern at different spatial scales, from the scale of the smallest channel to the scale of the braid plain width. The fact that model rivers, after they are left to evolve long enough, also exhibit spatial scaling definitely supports the validity of the model. Moreover, scaling anisotropy of natural braided rivers due to gravity is also present in model rivers, which also speaks in favor of the model. It should be mentioned that although the scaling anisotropy of modeled rivers is not very far from that of natural rivers, it is somewhat higher. We believe that the higher value of the scaling anisotropy parameter ν_x/ν_y in the modeled rivers is (at least partially) due to the fact that because of the restrictions of the simulated basin width they were forced to be rectilinear as a whole. The presence of the long-scale sinuosity in natural braided rivers (unless they are restricted by natural constraints) is an important component of their geometry which obviously produces a lower scaling anisotropy compared to the situation when the whole structure is strictly oriented in one direction. It remains to be determined whether the higher anisotropy of the modeled rivers is caused only by different external conditions (the imposed rectilinear shape of the basin) or is also due to the imperfection of the rules of the model. Also, the scaling anisotropy parameter shows higher variance for modeled rivers (1.44–1.95) than for the studied natural rivers (1.41–1.60). We believe this is due to the restricted size of the grid-modeled rivers, which lead to modeled rivers with fewer channels than the natural rivers and, correspondingly, more statistical noise.

In braided rivers, deep narrow sections of the river, which can carry more sediment and therefore cause erosion, are followed by wider and shallower sections where deposition occurs. The current loses much of its sediment in such divergent shallow sections and thus is capable of eroding the bed downstream, producing again a deep and narrow section. State-space analysis shows how such wide shallow and deep narrow sections of a river follow each other. Since these sequences are governed by the processes controlling deposition and erosion of the river, comparison of state-phase plots of modeled rivers with natural ones can tell us if the important features of the physical mechanisms in braided rivers are captured by the model. Our state-space analysis shows that for both Q_s rules 3 and 4, model realism depends on the parameters of the model (e.g., compare Figures 3d and 3e, or see Figure 5). For the best values of parameters the normalized distance between modeled rivers and natural rivers is not very much higher than the distance between the natural rivers themselves. This indicates that the physical mechanisms responsible for the geometry of braided rivers are mainly represented in the model (although some difference between modeled and natural rivers still remains). Our results suggest that model behavior is not sensitive to the difference between Q_s rules 3 and 4. In our opinion, this indicates that once physical mechanisms allow sediment to be transported over flat slopes (which is important), the details of how it happens are not critical. It should be noted, however, that some differences may still exist. Thus our fractal analysis of the spatial structure of the model rivers at different moments in time reveals that rivers produced by Q_s rule 4 needed more time to develop the "realistic" pattern (i.e., the pattern showing spatial scaling as natural rivers do) than the rivers produced by Q_s rule 3.

Although we believe that the state-space analysis and the self-affine fractal analysis presented in this paper together

make up a fairly comprehensive test for validating braided rivers models, there are other important issues not reflected in this analysis. We think that at least three other features of modeled braided rivers should be compared to natural ones: (1) the terrain produced by the river, (2) the hydrology of the river (e.g., distribution of the discharge between the channels), and (3) the evolution of the river (e.g., it was shown by *Sapozhnikov and Foufoula-Georgiou* [1997] that braided rivers exhibit dynamic scaling, an indicator of self-organized criticality). This work is currently under development.

Acknowledgments. The authors would like to thankfully acknowledge the support of this research by NSF grant EAR-9628393 and by NASA grant NAG-6191. Supercomputer resources were kindly provided by the Minnesota Supercomputer Institute.

References

Ashmore, P., Process and form in gravel braided streams: Laboratory modelling and field observations, Ph.D. thesis, Univ. of Alberta, Edmonton, 1985.

Blondeaux, P., and G. Seminara, A unified bar-bend theory of river meanders, *J. Fluid Mech.*, *157*, 449–470, 1985.

Dudley, R. M., Probabilities and metrics, *Lecture Note Ser. 45*, Mat. Insti. Arhus Univ., Arhus, Denmark, 1976.

Dudley, R. M., *Real Analysis and Probability*, Wadsworth, Belmont, Calif., 436 pp., 1989.

Fredsoe, J., Meandering and braiding of rivers, *J. Fluid Mech.*, *84*, 609–624, 1978.

Frish, U., B. Hasslacher, and Y. Pomeau, Lattice-gas automata for Navier-Stokes equation, *Phys. Rev. Lett.*, *56*, 1505–1508, 1986.

Hutchinson, J. E., Fractals and self-similarity, *Indiana Univ. Math. J.*, *30*, 713–747, 1981.

Kaneko, K., *Theory and Applications of Coupled Map Lattices*, 189 pp., John Wiley, New York, 1993.

Miller, R. G., Jr., *Beyond Anova: Basics of Applied Statistics*, 317 pp., John Wiley, New York, 1986.

Moeckel, R., and A. B. Murray, Measuring the distance between time series, *Physica D*, *102*, 187–194, 1997.

Murray, A. B., and C. Paola, A cellular automata model of braided rivers, *Nature*, *371*, 54–57, 1994.

Murray, A. B., and C. Paola, A new quantitative test of geomorphic models applied to a model of braided streams, *Water Resour. Res.*, *32*(8), 2579–2587, 1996.

Murray, A. B., and C. Paola, Properties of a cellular braided stream model, *Earth Surf. Processes Landforms*, *22*, 1001–1025, 1997.

Nikora, V. I., D. M. Hicks, G. M. Smart, and D. A. Noever, Some fractal properties of braided rivers, paper presented at 2nd International Symposium on Fractals and Dynamic Systems in Geoscience, Univ. of Frankfurt, Frankfurt/Main, Germany, April 4–7, 1995.

Nykanen, D. K., E. Foufoula-Georgiou, and V. B. Sapozhnikov, Study of spatial scaling in braided river patterns using synthetic aperture radar imagery, *Water Resour. Res.*, *34*(7), 1795–1807, 1998.

Parker, G., On the cause and characteristic scales of meandering and braiding in rivers, *J. Fluid Mech.*, *76*, 457–480, 1976.

Parker, G., Self formed rivers with equilibrium banks and mobile bed, 2, The Gravel River, *J. Fluid Mech.*, *89*, 127–146, 1978.

Parker, G., Lateral bed load transport on side slopes, *J. Hydrol. Eng.*, *110*, 197–199, 1984.

Salem, J., and S. Wolfram, Thermodynamics and hydrodynamics of cellular automata, in *Theory and Applications of Cellular Automata*, edited by S. Wolfram, pp. 326–366, World Sci., River Edge, N. J., 1986.

Sapozhnikov, V. B., and E. Foufoula-Georgiou, Study of self-similar and self-affine objects using logarithmic correlation integral, *J. Phys. A Math. Gen.*, *28*, 559–571, 1995.

Sapozhnikov, V. B., and E. Foufoula-Georgiou, Self-affinity in braided rivers, *Water Resour. Res.*, *32*, 1429–1439, 1996.

Sapozhnikov, V. B., and E. Foufoula-Georgiou, Experimental evidence of dynamic scaling and indications of self-organized criticality in braided rivers, *Water Resour. Res.*, *33*, 1983–1991, 1997.

Sauer, T. J., J. A. York, and M. Casdagli, Embedology, *J. Stat. Phys.*, *65*, 579–616, 1991.

Sugihara, G., Nonlinear forecasting for the classification of natural time series, *Philos. Trans. R. Soc. London, Ser. A*, *348*, 477–495, 1994.

Takens, F., Detecting strange attractors in turbulence, in *Dynamical Systems and Turbulence*, edited by D. A. Rand and L. S. Young, pp. 366–381, Springer-Verlag, New York, 1981.

Tennekes, H., and J. L. Lumley, *A First Course in Turbulence*, 300 pp., MIT Press, Cambridge, Mass., 1990.

Toffoli, T., Cellular automata model as an alternative to (rather than approximation of) differential equations in modeling physics, *Physica D*, *10*, 117–127, 1984.

Vichniac, G., Simulating physics with cellular automata, *Physica D*, *10*, 96–115, 1984.

Weigend, A. S., and Gershenfeld, N. A. (Eds.), *Time Series Prediction: Forecasting the Future and Understanding the Past, SFI Stud. Sci. Complexity*, 630 pp., Addison-Wesley, Reading, Mass., 1994.

Wolman, M. G., A method of sampling coarse riverbed material, *Eos Trans. AGU*, *35*, 951–956, 1954.

E. Foufoula-Georgiou and V. B. Sapozhnikov, Department of Civil Engineering, St. Falls Laboratory, University of Minnesota, Mississippi River at Third Avenue, SE, Minneapolis, MN 55414-2196. (e-mail: efi@mykonos.safhl.umn.edu; victor@mykonos.safhl.umn.edu)

A. B. Murray and C. Paola, Department of Geology and Geophysics, University of Minnesota, Minneapolis, MN 55455. (e-mail: brad@beaches.ucsd.edu; cpaola@maroon.tc.umn.edu)

(Received November 24, 1997; revised April 21, 1998; accepted May 18, 1998.)

St. Anthony Falls Laboratory
Tech. Paper No. 560-A, Series A

WATER RESOURCES RESEARCH, VOL. 34, NO. 7, PAGES 1795–1807, JULY 1998

Study of spatial scaling in braided river patterns using synthetic aperture radar imagery

Deborah K. Nykanen, Efi Foufoula-Georgiou, and Victor B. Sapozhnikov
St. Anthony Falls Laboratory, University of Minnesota, Minneapolis

Abstract. Synthetic aperture radar (SAR) imagery offers an appealing way of remotely monitoring the complex and rapidly changing forms of braided rivers. These rivers are often found in scarcely inhabited regions and are so dynamic that in situ measurements are almost impossible. In this paper, SAR imagery was used to extract braided river patterns such that their spatial scaling characteristics could be studied. From analysis of several reaches of a braided river in Alaska (the Tanana River), self-affine spatial scaling of the river patterns was found to be present under different flow rates and in different seasons when the river was undisturbed (free of external topographic controls). In regions where predominant geologic controls (i.e., mountains) or predominant flow paths (several tens of times the size of the other channels) were present, no spatial scaling was found. When scaling was found, the values of the anisotropic scaling exponents ν_x and ν_y had very similar values to those found by *Sapozhnikov and Foufoula-Georgiou* [1996] from traced and digitized aerial photographs of several braided rivers.

1. Introduction

Braided rivers consist of numerous alluvial channels that divide and rejoin around bars and islands, forming an intertwining structure that resembles a braid. The dynamic nature of a braided river causes these channels to shift and migrate across the river's braidplain. It is this dynamic nature that makes braided rivers both interesting and difficult to study, especially in a quantitative way. However, the need to build bridges across sections of braided rivers, to harvest the rich mineral deposits left on their bars and banks, and to study the ecological effects of the migrating channels has developed a pressing need for quantitative understanding and prediction of these complex hydrogeomorphological systems and their evolution.

There are several ways in which such large, complex systems could be quantitatively approached. Most research on braided rivers to date has concentrated on understanding the small-scale processes such as flow and sediment flux around an individual channel bar or confluence [*Ashmore and Parker*, 1983; *Ashmore et al.*, 1992; *Best*, 1986, 1988; *Bristow et al.*, 1993; *Mosley*, 1976, 1977; *Robert*, 1993]. These detailed studies of processes in a small area are valuable but do not necessarily lead to improved understanding of the mechanics of the entire system. Physically based studies and mechanistic modeling of braided rivers aimed at understanding the entire system would be too computationally intensive. A full solution of the governing equations for flow around a single confluence is intensive, and a braided river reach involves many such converging and diverging flow regimes around its numerous bars and islands. Also, there is relatively little quantitative information on how changes in one part of the system propagate to other parts and on which components of the small-scale flow and sediment dynamics contribute to the overall behavior of the system.

Recently, some alternative approaches to studying the morphology and dynamics of braided rivers have been proposed. These type of studies aim to determine which physical processes are critical and how they affect the dynamics of the system as a whole and then concentrate on detailed studies of these processes. *Murray and Paola* [1994] developed a cellular automaton model of a braided river using a simple, deterministic approach of water flow over a cohesionless bed. Their model reproduced the main spatial and temporal features of natural braided rivers. Their results suggested that the main factors essential for braiding were bedload sediment transport and laterally unconstrained free-surface flow. *Sapozhnikov and Foufoula-Georgiou* [1996, 1997] have shown that an effective and fruitful way to study interactions of small-scale and large-scale dynamics of complex natural systems is via statistical scaling analyses, i.e., analyses aimed at determining how morphological or dynamical properties of the system at one scale relate to those at another scale. Such scaling relationships are commonly found in natural systems, including single channels and river networks [e.g., *Tarboton et al.*, 1988; *La Barbera and Rosso*, 1989; *Nikora*, 1991; *Sapozhnikov and Nikora*, 1993; *Peckham*, 1995; *Beauvais and Montgomery*, 1996] but have not yet been fully developed or understood in braided rivers. Braided river systems manifest themselves over a large range of scales (e.g., from the smallest channels of a few meters to the whole braidplain width of tens of kilometers). The issue of scale is an essential element when applying the knowledge gained from a small part of a braided river to a larger part of it, from one braided river to another of different size, or from a laboratory model to a real braided river.

Sapozhnikov and Foufoula-Georgiou [1996] found, through analysis of the spatial structure of traced, digitized aerial photographs, that spatial scaling exists in the morphology of natural braided rivers. Spatial scaling implies that morphological properties (e.g., area covered by water) of the system at one scale relate to those at another scale via a transformation which involves only the ratio of the two scales. Through the production of a laboratory braided river in a small experimental facility (0.75 m × 5 m) at the St. Anthony Falls Laboratory,

Paper number 98WR00940.
0043-1397/98/98WR-00940$09.00

Sapozhnikov and Foufoula-Georgiou [1997] also found the presence of scaling in the temporal evolution of braided rivers, called dynamic scaling. Dynamic scaling implies that space and time can be appropriately rescaled such that the evolution of the spatial structure of a small part of a braided river is statistically indistinguishable from that of another larger part or of the whole river. Such relationships could be used, for example, to statistically predict large less frequently occurring changes in the river from smaller more frequent changes or could be used to make inferences about the underlying physical mechanisms controlling the evolution of braided rivers [e.g., see *Sapozhnikov and Foufoula-Georgiou*, 1997, section 5].

It is imperative that the above findings of dynamic scaling are further investigated and that the presence of spatial scaling is further verified using a wide range of natural braided rivers. Braided rivers often exist in scarcely inhabited, high-latitude, glaciated areas and are also constantly evolving, which makes it difficult to perform any sort of ground-based measurements. Also, obtaining aerial photographs at an adequate temporal resolution is difficult and often prohibiting for a single investigator. On the other hand, remote sensing is an attractive means of continually monitoring these complex systems from space. The technology of synthetic aperture radar (SAR) imagery has opened a door of opportunity in the area of quantitative studies of braided rivers, but only a very few studies have existed to date [e.g., *Smith et al.*, 1995, 1996]. The scope of this research is to investigate further the presence of spatial scaling relationships in natural braided river patterns using SAR imagery and to explore how this scaling might be affected by flow rate, braiding index, and large-scale topographic controls, such as mountains.

2. Extraction of Braided River Patterns From SAR Imagery for Quantitative Scaling Analysis

The SAR, being carried on an aircraft or spacecraft platform (i.e., satellite), transmits a signal toward Earth at an incidence angle and then measures how much of the signal is echoed back (called backscatter). The backscatter depends on the dielectric properties and surface roughness of the material on Earth being scanned by the radar. SAR's independence of solar illumination and cloud cover makes it especially useful in providing consistent seasonal and diurnal coverage, which is hard to do with aerial photographs or other remote sensors. Each pixel in a SAR image represents the radar backscatter for the area on the ground covered by that pixel. The radar backscatter is recorded as a brightness value, or intensity, which in a gray-scale mode ranges from 0 to 255. Brightness values in the lower end of the range (i.e., dark) are recorded for low radar backscatter, and values in the upper end of the range (i.e., bright) are recorded for high backscatter. In general, rough ground surfaces cause bright pixels, and smooth ground surfaces cause dark pixels in the image. Brightness increases with the wetness of the object, except for the case of a smooth (i.e., calm) body of water, which will appear dark. (See http://www.asf.alaska.edu, *Oliver* [1991], and *Olmsted* [1993] for more information on SAR imagery and its interpretation.)

In this study, SAR imagery acquired by the first European Remote Sensing Satellite (ERS-1) was used. ERS-1 was launched on July 17, 1991, by the European Space Agency (ESA). It carries a C-band (5.66 cm wavelength) SAR and has a spatial resolution of 30 m with a pixel spacing of 12.5 m and coverage of a 100 km × 100 km area in each image. The images used for this study were ERS-1 full-resolution images collected over the Tanana River in May through October of 1993. They were provided by the ESA and acquired through the Alaska SAR Facility (ASF).

The methodology for extracting the braided river patterns from the SAR images is based on the property of smooth bodies of water appearing dark. Although this may work well for single-channel rivers, the conditions of wet gravel on bars and banks and changes in backscattering intensity for narrower, shallower channels make it difficult to delineate active channels in braided rivers [*Smith et al.*, 1996]. The method of extraction developed here deals with these difficulties by combining a series of automated and manual steps and is therefore referred to as a semiautomated procedure. The method is broken down into four stages: (1) image processing, (2) image enhancement, (3) image classification, and (4) postimage processing.

2.1. Image Processing

The first step in working with SAR data is radiometric calibration. This is an adjustment to the brightness values in the image to compensate for the antenna pattern's, range-to-target's, and incidence angle's effect on the signal level. It permits comparison of brightness values between different images and also within a single image. The correction is based on the measured response to aluminum trihedral corner reflectors of known size, shape, orientation, and cross section placed on the ground at strategic locations within the ASF station mask. The ERS-1 SAR images used for this study were radiometrically calibrated using a software program provided by ASF called "calibrate." (See http://www.asf.alaska.edu and *Olmsted* [1993] for more information on radiometric calibration.) Another program provided by ASF called "sarautoreg" was used to automatically geocode the images. Geocoding simply means rotating the image from a swath reference frame, which is orientated along the flight path of the satellite, to a geographic coordinate system.

After the images have been radiometrically calibrated and geocoded they were filtered to reduce speckle noise. Speckle noise is an inherent feature of SAR and is produced when surface variations near the size of the radar's wavelength (e.g., small rocks, leaves, and ripples on a water surface) cause multiple scatters of the radar echo, which when added incoherently give a higher backscattering intensity. This net backscatter makes the object on the surface appear as a bright pixel in the SAR image. Although it is not feasible to completely remove speckle noise, it can be sufficiently reduced and smoothed using filtering algorithms. Through literature review [*Frost et al.*, 1982; *Lopes et al.*, 1990; *Hagg and Sties*, 1994; *Shi and Fung*, 1994] and informal comparative testing on an image clip, it was determined that the Frost filter [*Frost et al.*, 1982], with a 3 × 3 kernel and a coefficient of variation equal to that computed for the unfiltered image, worked best for suppressing speckle noise while preserving edge structures and linear features. Other filters considered in the informal comparative testing were Lee, Lee-Sigma, Maximum a Posteriori (MAP), and Median. (See *Lopes et al.* [1990] and *Shi and Fung* [1994] for a description of these filters.) Various kernel sizes, coefficients of variation, and numbers of passes were also tested for each filter. The filters were applied using the software package Imagine 8.2, developed and distributed by ERDAS®, Inc.

Following the Frost filter, the images were refiltered using a

2×2 mean filter to further smooth and suppress speckle noise. The images were also rotated so that the upstream and downstream end points of the river reach were vertically aligned, with the upstream end at the top of the image.

2.2. Image Enhancement

Since regions of calm water and other smooth surfaces appear dark in SAR images, ideally, all river channels would appear dark with an associated gray-scale brightness value of 0. However, nonuniform conditions and inconsistencies in backscatter returns cause the brightness values to range anywhere from 0 to 150 (on a scale of 0–255) and even greater in some cases. In order to decipher which pixels are occupied by water and which are not, image enhancement is needed to be able to follow tonal variations in a similar fashion as the human eye does.

The first step in the image enhancement stage was to adjust the contrast levels in the images. This is known as contrast enhancement, and it increases the differences (or contrast) between the reflectivity of two different materials. It is applied by setting all values below a lower threshold to 0 and values above an upper threshold to 255. The values between the upper and lower threshold are then stretched over the 1–254 range. (See *Jensen* [1996] for more information on contrast enhancement.) The most suitable upper and lower thresholds were determined by trial and error for each image, with the upper thresholds typically ranging around 200 and the lower thresholds ranging around 100. (See Appendix A for justification of the subjectivity in the threshold selection.) This linear contrast adjustment worked well for darkening water pixels and brightening nonwater pixels, resulting in an improved braided channel network. Pixels that were part of an active channel and had values below the lower threshold now became uniformly dark with an associated brightness value of 0. The pixels that were also part of an active channel but had values that fell above the lower threshold now had brightness values closer to 0. The SAR images were contrast-enhanced using Adobe Photoshop 3.0.

The next step in the image enhancement stage was to improve the channel connectivity. The technique used was to look at directional averages and fill-in channels (i.e., set their pixel value equal to 0) based on these averages. An algorithm was developed that computed the average brightness value over a user-specified number of pixels away from a center pixel in eight different directions. The direction of the smallest of the eight directional averages was taken as the preferred channel direction. If this smallest average was below a specified minimum average criterion, then the center pixel and a user-specified number of pixels away from the center pixel in the preferred direction (typically smaller than the number of pixels used for the directional averaging) were set equal to 0. The algorithm then moved to the next pixel and repeated the process. The result was an improved braid channel network but not yet completely connected.

2.3. Image Classification

In order to ensure a completely connected braid channel network some manual image manipulation was required. The image classification stage is the "semi" part of the semiautomated extraction procedure. The SAR images were loaded into the graphics program Neopaint 3.2a, developed and distributed by NeoSoft Corporation. The connected braid channels were filled with a user-specified color by clicking the upstream end of a known channel. All connected pixels with brightness values of 0 were automatically filled with the color. The disconnected sections that visually appeared to be part of active channels were then manually filled with the color by following the tonal variations. The degree of subjectivity here was that the user must determine which gaps are truly part of active channels and which are produced by overfill into inactive channels. However, in most cases the tonal variations made this determination fairly clear to the human eye. The result, after approximately 1 hour of manual image cleanup, was a completely connected braid channel network with inactive channels truncated and rough edges smoothed. The image files were then converted to a binary classification scheme where all pixels filled with the color where set equal to 1 (denoting a wet pixel) and all other pixels were set equal to 0 (denoting a dry pixel).

An Unsupervised Bayesian Classification algorithm was tried as an alternative to fully automate the extraction procedure (applied using Imagine 8.2, developed and distributed by ERDAS®, Inc.). However, the result was still a discontinuous channel network. Its performance was less desirable than the above described image-processing stages in that it tended to misclassify numerous nonwater pixels as water and vice versa.

2.4. Postimage Processing

The final stage of the extraction methodology used in this study was to run the binary classified file (i.e., 1s and 0s) through a modified median filter. This was done to further smooth channel edges and fill extraneous point bars. This filter works by counting the number of filled pixels (i.e., value of 1) in a 3×3 kernel. If the total number was ≥ 5 (majority of the box contains water pixels), then the center pixel was set equal to 1 or "wet." If the sum was ≤ 2 (largely a nonwater box), then the center pixel was set equal to 0 or "dry." At this point the image files were now ready for testing the presence of scaling and estimating the spatial scaling exponents.

3. Testing for Spatial Scaling and Estimation of Scaling Exponents

The presence of spatial scaling in an object means that statistical properties at one scale relate to the statistical properties at another scale via a transformation which involves only the ratio of the two scales. This is also known as scale invariance and means that the object is statistically indistinguishable under proper magnification or contraction. When the properties scale similarly in all directions, it is referred to as isotropic scaling, and the object is a self-similar fractal. However, when the properties scale differently in different directions, it is called anisotropic scaling, and the object is a self-affine fractal. *Sapozhnikov and Foufoula-Georgiou* [1995] developed a methodology to test and quantitatively assess the presence of self-affinity in any complex geometrical pattern, such as a braided river, and to estimate the fractal exponents that define its spatial scaling. This method is called the logarithmic correlation integral (LCI) method and is briefly presented here for sake of completeness.

Let X and Y be the sides of a rectangle and $M(X, Y)$ be the mass (e.g., the number of pixels covered by water) of the part of the object contained within the $X \times Y$ rectangle. Then, spatial scaling implies that

$$M(X,Y) \sim X^{1/\nu_x} \sim Y^{1/\nu_y} \tag{1}$$

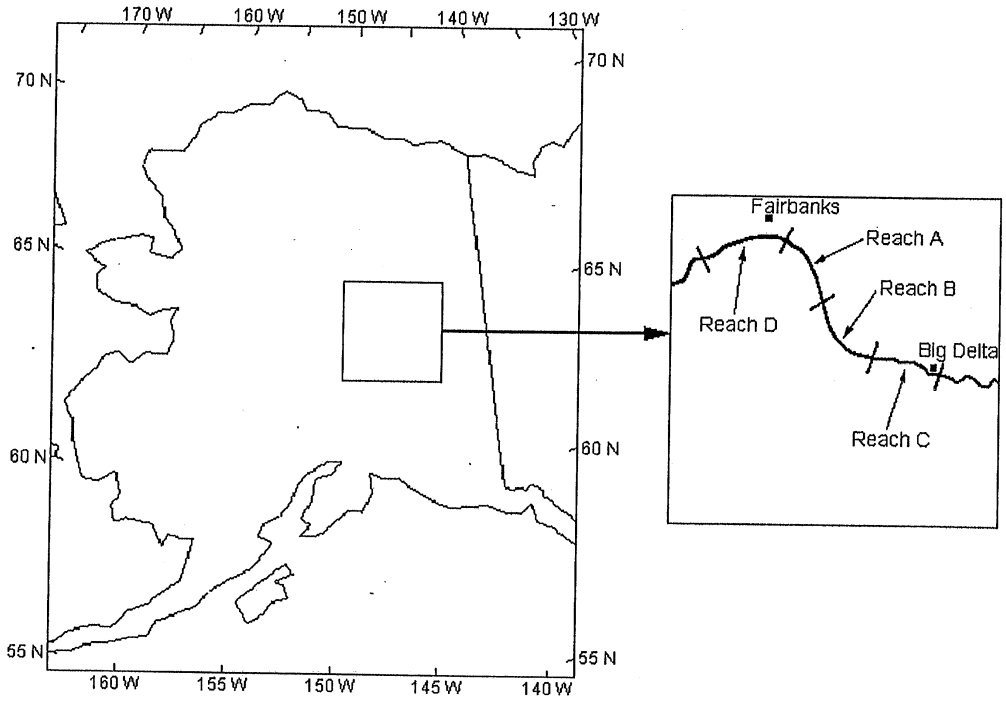

Figure 1. Location of Tanana River, Alaska, and studied sites.

where ν_x and ν_y are the fractal exponents corresponding to the X and Y directions, respectively. This equation can be written in the form

$$\left(\frac{X_2}{X_1}\right)^{1/\nu_x} = \left(\frac{Y_2}{Y_1}\right)^{1/\nu_y} = \left(\frac{M_2}{M_1}\right) \tag{2}$$

If we let $x = \log X$, $y = \log Y$, and $z = \log M$, we get

$$\frac{x_2 - x_1}{\nu_x} = \frac{y_2 - y_1}{\nu_y} = z_2 - z_1 \tag{3}$$

or

$$\frac{dx}{\nu_x} = \frac{dy}{\nu_y} = dz \tag{4}$$

The function $M(X, Y)$ is known as the correlation integral, and by analogy we call the function $z(x, y)$ the logarithmic correlation integral of the object under study. Comparing (4) with

$$\frac{\partial z}{\partial x}\,dx + \frac{\partial z}{\partial y}\,dy = dz \tag{5}$$

we obtain

$$\nu_x \frac{\partial z}{\partial x} + \nu_y \frac{\partial z}{\partial y} = 1 \tag{6}$$

This relationship provides a method for testing the presence of spatial scaling and for estimating the fractal exponents ν_x and ν_y of a self-affine object, as follows. Having estimated the logarithmic correlation integral $z(x, y)$ from a pattern of the object by direct calculation of the mass $M(X, Y)$ (i.e., pixels covered by water) within rectangles of sizes $X \times Y$, one can calculate the derivatives $\partial z(x, y)/\partial x$ and $\partial z(x, y)/\partial y$ and use them to test whether the linear relationship (6) is satisfied and, if yes, to find the values of ν_x and ν_y. As can be seen from the above equation, $1/\nu_y$ is the intercept of the linear best fit line with the vertical axis, and $-\nu_x/\nu_y$ is the slope. Ideally, only two

Table 1. ERS-1 Synthetic Aperture Radar (SAR) Images Used in This Study

ASF Data Identifier	Scene Indicator	Date	Time, UT	River Reaches Contained in Image	Flow Rate, cfs	Braiding Index
E1/S/09807.01	152993100	May 31, 1993	2106:34	A, B, D	35300	4.59, 4.23, 3.23
E1/S/10308.01	208531100	July 5, 1993	2106:39	A	49900	4.75
E1/S/11811.01	152999100	October 18, 1993	2021:47	A, B	unknown	4.06, 3.44
E1/S/10265.01	208527100	July 2, 1993	2101:05	C	51300	5.22
E1/S/10494.01	208588100	July 18, 1993	2058:11	C	60300	5.35
E1/S/10351.01	208533100	July 8, 1993	2112:21	D	49100	3.14

ASF, Alaska SAR Facility.

Table 2. Tanana River Reaches Used in This Study

Reach	Reach Length, km	Upstream Coordinates	Downstream Coordinates
A	28.6	64°34′, −147°04′	64°46′, −147°35′
B	34.25	64°18′, −146°43′	64°34′, −147°04′
C	25.8	64°10′, −145°53′	64°16′, −146°40′
D	32.2	64°35′, −147°40′	64°35′, −148°20′

points are needed to estimate v_x and v_y, but for a good estimation a least squares fit to the derivatives at all points of the surface $z(x, y)$ is preferable. Since both coordinates contain uncertainty in their values it is not appropriate to use the traditional least squares method, which minimizes the sum of the squares of the vertical distances between the fitted line and the actual data points, since this method is sensitive to the orientation of the coordinate system. Thus a method which minimizes the sum of the squares of the perpendicular distances was used. This method was implemented with the revised algorithm of *Alciatore and Miranda* [1995] which is numerically stable and gives a unique solution.

4. Analysis of the Spatial Scaling of the Tanana River, Alaska

The ERS-1 SAR images selected for analysis cover the Tanana River from Big Delta, Alaska, to just past Fairbanks, Alaska, and were taken between May 31 and October 18 of 1993. They were selected to cover various reaches of the Tanana River over different instants of time and flow rates (see Figure 1). Table 1 lists the images analyzed and their corre-

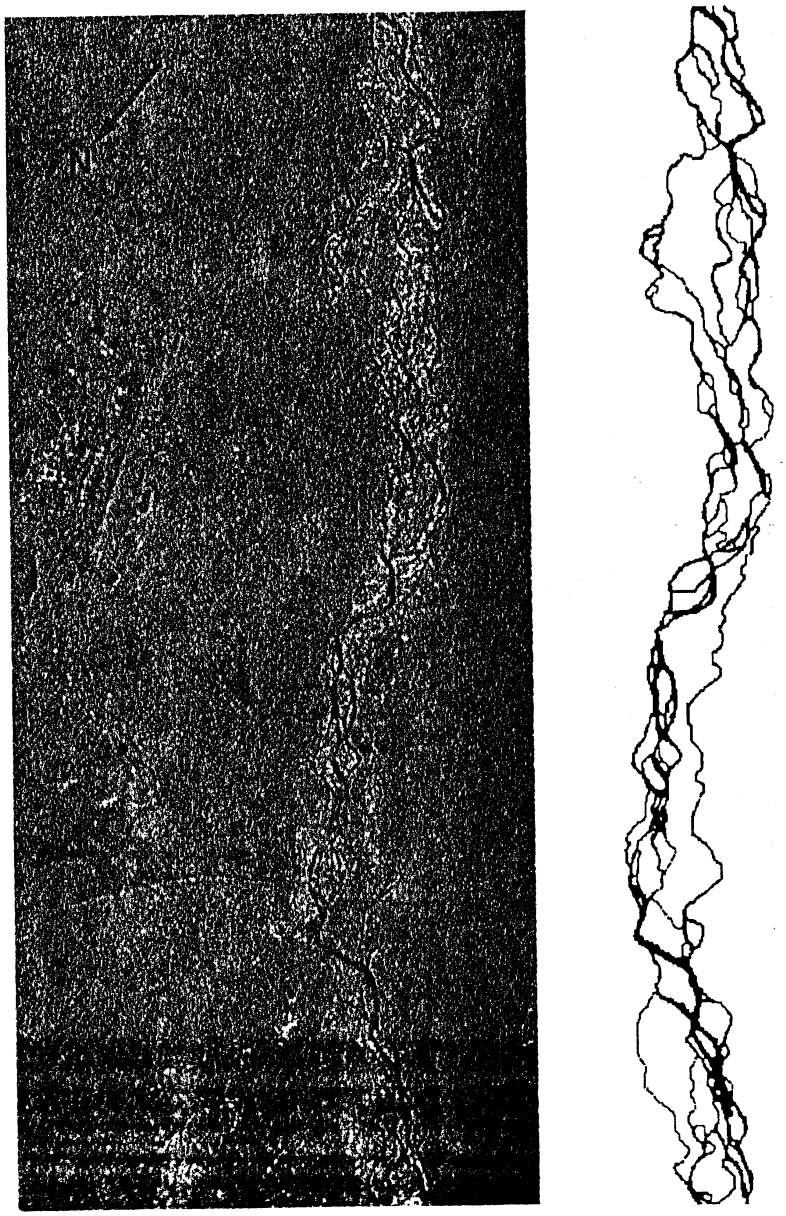

Figure 2. Original synthetic aperture radar (SAR) image and extracted braided river pattern of the Tanana River: reach A, image ID 152999100. Copyright ESA 1993.

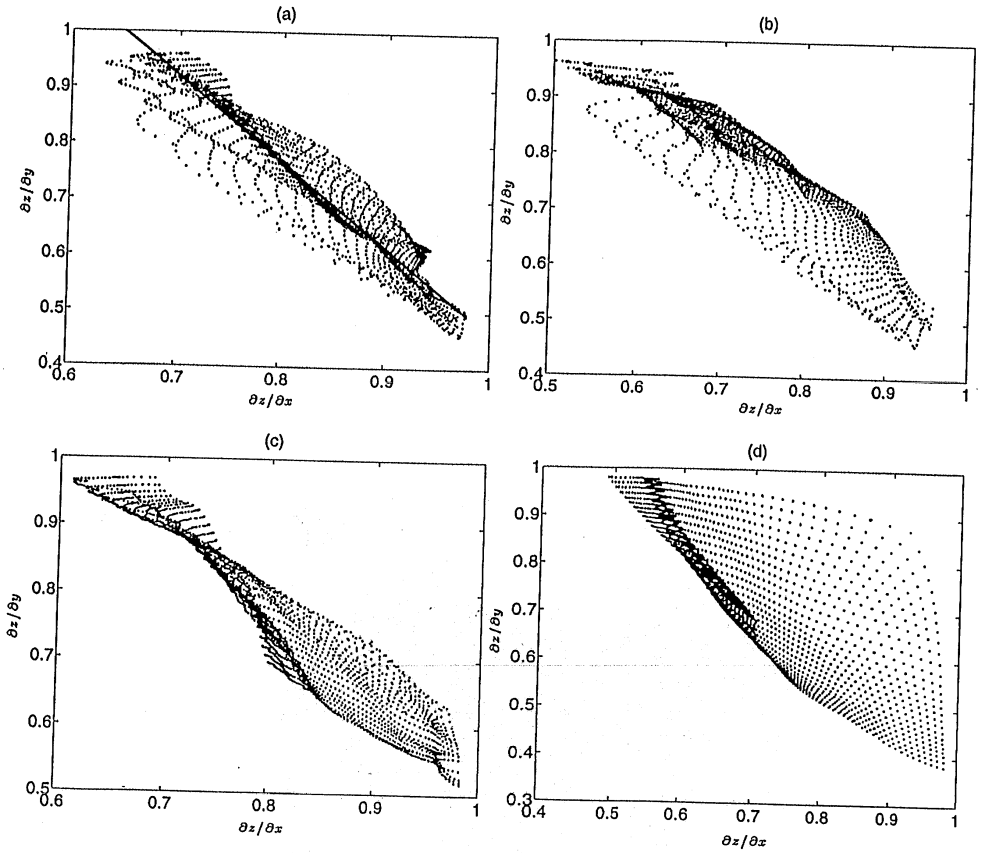

Figure 3. Testing the presence of spatial scaling and estimation of the fractal exponents ν_x and ν_y for the extracted braided river pattern of the Tanana River: (a) reach A, image ID 152999100, (b) reach B, image ID 152993100, (c) reach C, image ID 208527100, and (d) reach D, image ID 208533100.

sponding river reach, date, time, flow rate, and braiding index. Flow rates were obtained from the U.S. Geological Survey (USGS) records and were measured near Fairbanks, Alaska. The braiding index for each river reach was computed as the average number of channels in all cross sections of the extracted pattern. (Note that the braiding index does not reflect the relative width of these channels.) The length and coordinates of the four reaches analyzed are shown in Table 2. The patterns were extracted from each of the SAR scenes using the extraction methodology described in section 2 and validated in Appendix A, and their spatial scaling was analyzed using the logarithmic correlation integral method reviewed in section 3.

Three scenes were analyzed for reach A, the river reach stretching from south of the Eielson Air Force Base to Fairbanks. This reach is 28.6 km in length with an average braidplain width of 1 km and a slope of 0.0011. The original SAR scenes and the extracted braided river patterns for this reach are given by *Nykanen* [1997]. Here only the October 18, 1993, scene of this reach is shown in Figure 2. All three scenes exhibited good scaling within scales corresponding to the width of the smallest individual channels up to the whole braidplain width. We show here the scaling results of only the October 18, 1993, scene (see Figure 3a) and summarize the results for all three scenes in Table 3. The flow rate for the July 5th scene is ~15,000 cfs more than the May 31st scene. The flow rate for the October 18th scene is unknown but was estimated from the method of *Smith et al.* [1996] (see Appendix B) to be 7800 cfs, which is substantially lower than the other two scenes. It is interesting to note that despite the large range in flow rates the spatial scaling stills holds for all three scenes of reach A and with similar scaling exponents. The ν_x and ν_y values were 0.74–0.77 and 0.47–0.50, respectively, as shown in Table 3.

Table 3. Spatial Scaling for the Tanana River, Reach A (South of Eielson Air Force Base to Fairbanks)

Scene Indicator	Date	Flow Rate, cfs	Braiding Index	ν_x	ν_y	Correlation Coefficient	Average |error|	Standard Deviation |error
152993100	May 31, 1993	35300	4.59	0.74	0.47	−0.929	0.0175	0.0122
208531100	July 5, 1993	49900	4.75	0.70	0.50	−0.844	0.0205	0.0189
152999100	October 18, 1993	7800*	4.06	0.77	0.50	−0.953	0.0158	0.0143

*Flow rate estimated using W_e − Q relationship developed by *Smith et al.* [1996] (see Appendix B).

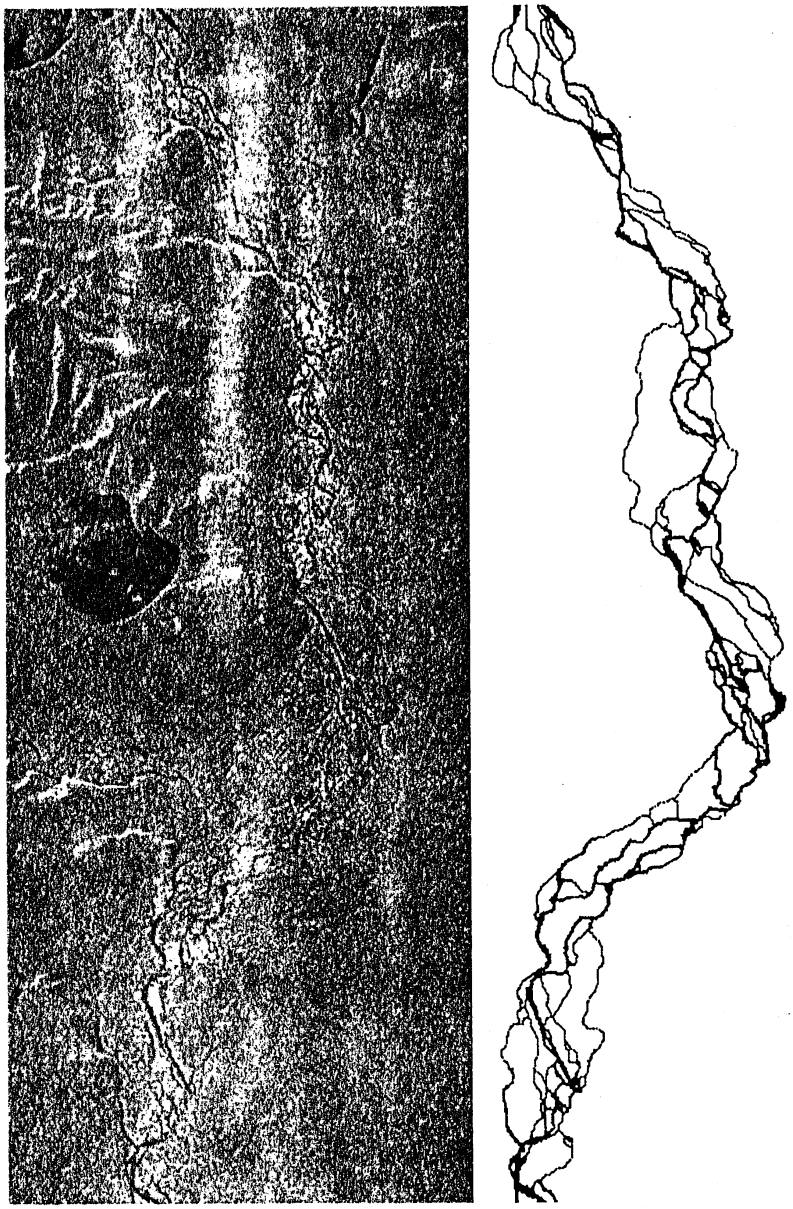

Figure 4. Original SAR image and extracted braided river pattern of the Tanana River: reach B, image ID 152993100. Copyright ESA 1993.

This stability in scaling structure for different flow rates was also found by *Nikora et al.* [1995] in a study of braided rivers as self-similar objects with reported fractal dimension $D = 1.5–1.7$. They found universality of the channel pattern fractal dimension under various water discharge rates for the Ohau River in New Zealand and related this universality to the appearance of new anabranches on big islands compensating the flooding of small islands when the water discharge increases.

Contrary to reach A, reaches B and C of the Tanana River displayed relatively poor scaling for all scenes analyzed. For example, Figures 3b and 3c show the scaling results from the May 31, 1993, scene of reach B and the July 2, 1993, scene of reach C, respectively. Figures 4 and 5 show the SAR images of these reach B and C scenes, respectively. The cloud of points in Figures 3b and 3c are very different from the typical curve of Figure 3a. In both Figures 3b and 3c the main body of the cloud takes on a concave shape. Figures 3b and 3c also lack the fullness and even distribution of points throughout the cloud mass that is seen in Figure 3a. The reason for this poor scaling might be the interaction of the physical mechanisms controlling the braidplain morphology with external factors imposed on the river. In both reaches B and C a mountainous region adjacent to the river affected strongly the path of the river (see Figures 4 and 5 and *Nykanen* [1997] for all scenes of reaches B and C). When the braidplain of a river reach is forced by an external factor, it is definitely other mechanisms besides braiding that control the resulting morphology of the river. It appears that the prerequisite for spatial scaling is that the river is allowed to evolve in a natural, self-organized way such that the spatial structure of the river is determined by the same mechanisms at all scales. Any interference with this self-organization can break the underlying spatial scaling. Indeed, large-

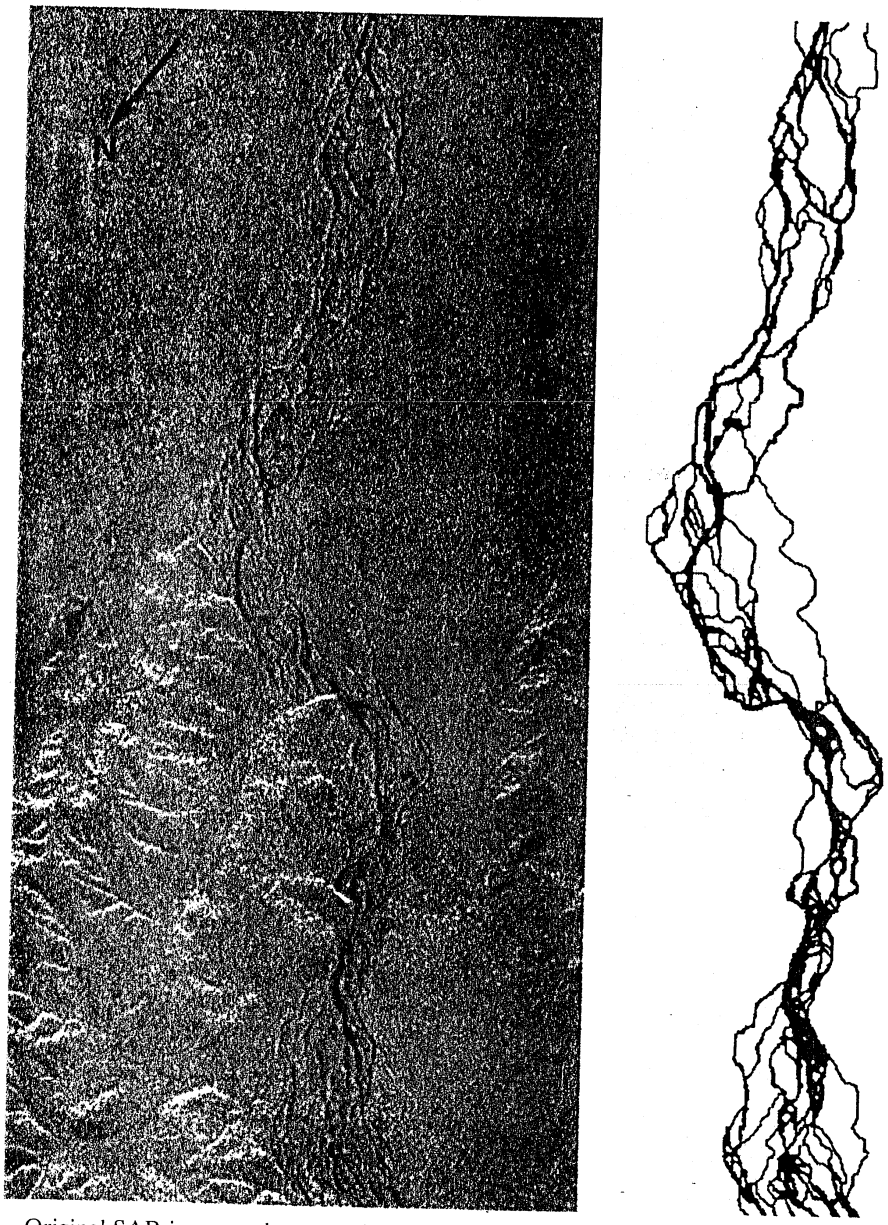

Figure 5. Original SAR image and extracted braided river pattern of the Tanana River: reach C, image ID 208527100. Copyright ESA 1993.

scale perturbations caused by external factors (e.g., mountains) are shown here to affect the scaling properties of the river pattern at all scales (even scales smaller than the scale of the external factor). This holds true, in general, for self-affine objects because they possess anisotropy at all scales but would not be true for self-similar objects. For example, rotating half of a self-similar object by 90° would break the scaling in the object at the scale of the rotation only but not at smaller scales. However, rotating half of a self-affine object by 90° would destroy the scaling anisotropy at all scales.

Reach D, located downstream of Fairbanks, is different from the other reaches in that the slope is more gradual and the braiding index is lower. The original SAR image for the July 8, 1993, scene of this reach is shown in Figure 6. It was found that spatial scaling also did not hold in this reach (see Figure 3d). In this case, however, there appeared to be no morphological constraints that would interfere with self-organization of the braidplain. The reach is characterized by braiding with a predominant channel throughout the reach. The width of this main channel is only 4 times smaller than the whole braidplain width and ~10 times greater than the next biggest channel; that is, channels of intermediate widths are missing from this river reach. Our analysis shows that such rivers, which are braided but have a predominant channel, do not exhibit self-affine scaling. It should be mentioned that lack of scaling here is due to the fact that not enough scales are present to detect scaling. It does not necessarily imply the presence of a different shaping mechanism compared to braided rivers with a large braiding index. Braided rivers with a low braiding index and a predominant flow path (channel width) can be seen as a transitional case between the class of simple meandering rivers and braided rivers with all scales of

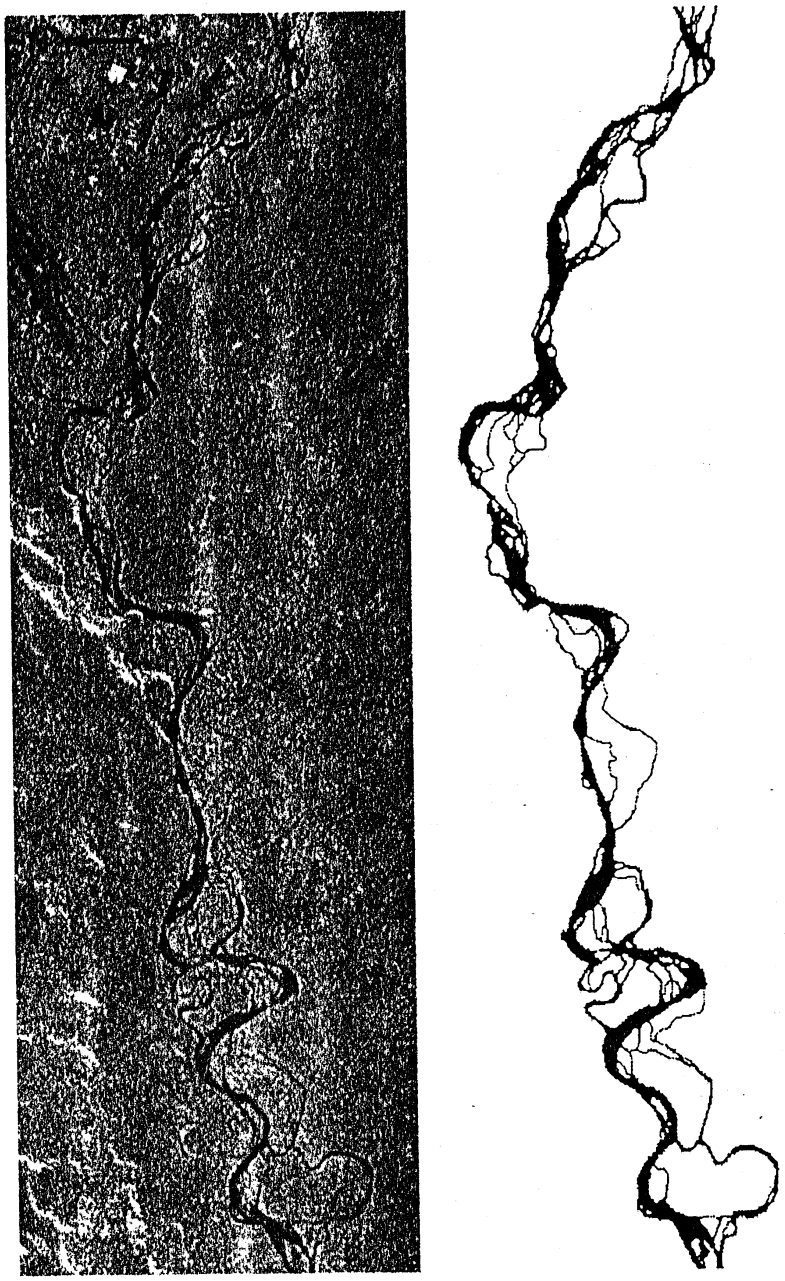

Figure 6. Original SAR image and extracted braided river pattern of the Tanana River: reach D, image ID 208533100. Copyright ESA 1993.

channels present. In fact, reach D is also geographically a transitional river reach, connecting a braided regime (with all scales of channels present) to a single meandering river regime. Note that although self-affine spatial scaling has been found to hold for these two classes of rivers in undisturbed environments (with different scaling exponents) [e.g., see *Sapozhnikov and Foufoula-Georgiou*, 1996, Table 3], it was found here to fail for "transitional rivers," i.e., braided rivers with channels of a few predominant scales only.

5. Conclusions

Several conclusions can be drawn from this study of spatial scaling in braided river patterns from SAR imagery, which are as follows:

1. It was found through this research that a fully automated extraction procedure for extracting braided river patterns from SAR imagery is not feasible because of the limitations of using SAR imagery in a quantitative way. A semiautomated scheme involving several stages of speckle noise reduction, channel enhancement, and some manual image interpretation worked satisfactorily in extracting a reasonable and spatially consistent braid channel network suitable for spatial scaling analysis.

2. Self-affine spatial scaling for braided rivers was found to hold over different flow rates and instants of time when the river was free of topographic controls (e.g., mountains). It was found to be relatively poor in regions where a characteristic of the morphology, mountains in our case, prevents the river from

evolving and developing its braidplain in a natural (undisturbed) fashion.

3. Self-affine spatial scaling behavior was also not found to be present for a braided pattern with a predominant flow path, or main channel, several tens of times the size of the other channels in the braidplain. Lack of scaling in these patterns was argued not to imply necessarily the presence of different shaping mechanisms of braiding compared to braided patterns with enough scales of channel present.

4. Within the scales of its braidplain width and without the presence of morphological constraints the Tanana River was found to exhibit self-affine scaling with fractal exponents ν_x = 0.74–0.77 and ν_y = 0.47–0.50. Previously, *Sapozhnikov and Foufoula-Georgiou* [1996] found spatial scaling exponents of 0.72–0.74 for ν_x and 0.51–0.52 for ν_y from traced and digitized aerial photographs of three natural braided rivers (Brahmaputra River in Bangladesh and Hulahula and Aichilik Rivers in Alaska). The similarity in the exponents found previously to those found in this study is one step further in indicating that the spatial structure of braided rivers may be determined by universal features in the physical mechanisms shaping these rivers.

Although the physical implications and practical utility of scaling relationships are not fully understood yet, unraveling scale invariant relationships from complex natural patterns is interesting in its own right. The fact that these scale invariances in braided rivers seem to be present (and with universal parameters) in undisturbed systems which had the chance to self-organize themselves laterally and vertically to an equilibrium state but are not present in systems subject to other external controls implies that the physical mechanisms responsible for braiding are universal (independent of many specifics of the system like bed material, slope, etc.) and the same over a range of scales. It cannot be determined directly from ν_x and ν_y exactly what these mechanisms are. However, if we believe that self-affinity is a universal property of braided rivers, any physical model of braided rivers should exhibit this property. Thus modeling of braided rivers in conjunction with the revealed self-affinity can provide a powerful tool for understanding the mechanisms responsible for the formation of braided patterns.

More challenging than studying the planform morphology of braided rivers is studying the dynamics of their evolution in terms of space-time scale invariances. Such a study was recently performed by *Sapozhnikov and Foufoula-Georgiou* [1997], who found the presence of dynamic scaling in an experimentally produced braided river. It remains to be seen whether SAR imagery can provide the necessary data needed to verify or dispute the presence of dynamic scaling in natural braided rivers too and subsequently to study the conditions under which such spatiotemporal invariances in braided rivers seem to be present.

Appendix A: Validation of the Semiautomated Extraction Procedure

The semiautomated braided river pattern extraction methodology, developed in section 2, was tested and validated by comparing extracted river patterns to some form of ground truth. Typically, tracings of aerial photographs are accepted as valid ground truth. However, obtaining aerial photographs or ground-based observations of the same reaches of the Tanana River and at the same instants of time as on the ERS-1 SAR images was not feasible. Therefore the ground truth was taken as a tracing of a hardcopy of a full-resolution SAR image that was then digitized to produce an image consisting of black and white pixels, indicating the presence or absence of active channels. The question to be answered was could the semiautomated extraction method produce a braided river pattern comparable to a manual tracing in terms of visual appearance and spatial scaling analysis?

The scene used for verification was an ERS-1 SAR image taken on May 31, 1993, over the Tanana River, Alaska, just upstream of Fairbanks (reach A). The stages of image processing and image enhancement were automatically applied to that scene. Then, the manual stage of image classification was applied at three different levels. Level 1 involved ~30 min of manual image interpretation, while levels 2 and 3 involved an additional 15 min each. The incremental time between levels was used to consider more carefully tonal variation and to make the image more visually appealing (i.e., smoothing of channel edges and insuring complete channel connectivity). Obviously, the three levels correspond to different amounts of subjectivity and provide a means of testing the sensitivity of the spatial scaling results to subjective decisions in the extraction methodology. All images were subjected to the postimage processing stage applying the filtering discussed in section 2.

The extracted braided river patterns from semiautomated levels 1, 2, and 3, along with the pattern obtained by tracing, are shown in Figure 7. Visually, the level 3 pattern is most comparable to the digitized tracing, but visual comparison alone is not enough to validate the extraction methodology. Further validation involved comparing the spatial scaling results for the patterns obtained using the three levels of semiautomation to that of the traced pattern (which was considered the ground truth). For that purpose the logarithmic correlation method (LCI) of *Sapozhnikov and Foufoula-Georgiou* [1995] was applied to each of the patterns to test the presence of spatial scaling. The X axis was oriented in the streamwise direction and aligned to connect the upstream and downstream ends of the river reach. The Y axis was perpendicular to the X axis. From the correlation integral surface $z(x, y)$ the derivatives $\partial z(x, y)/\partial x$ and $\partial z(x, y)/\partial y$ were numerically computed from the part of the $z(x, y)$ surface corresponding to scales (Y) ranging between the smallest individual channel to the average width of the braidplain. The dependence of $\partial z(x, y)/\partial y$ versus $\partial z(x, y)/\partial x$ for each of the patterns is shown in Figure 8. The linear dependence (presence of scaling) is measured quantitatively by the correlation coefficient between $\partial z(x, y)/\partial y$ and $\partial z(x, y)/\partial x$ and the absolute error between the actual data points and the best fit line (or the spread of the cloud of points) (see Table 4). As can be seen from Figure 8a, which represents the ground truth, the cloud of points is well fitted by a straight line which confirms the presence of spatial scaling in this river pattern. Figures 8b, 8c, and 8d (see also Table 4) confirm also the presence of scaling for levels 1, 2, and 3 of the extraction methodology. The differences in the shape of the clouds reflect the subjectivities in the extraction methodology. Notice that in all cases the clouds of points are evenly distributed around the best fit lines and do not show the tendency of concavity as was the case in Figures 3b and 3c. The fact that scaling basically holds for all three of the extracted patterns is encouraging and verifies that the extraction methodology itself does not induce an artifical scaling break.

Despite the presence of scaling in all of the extracted patterns, there are some substantial qualitative differences be-

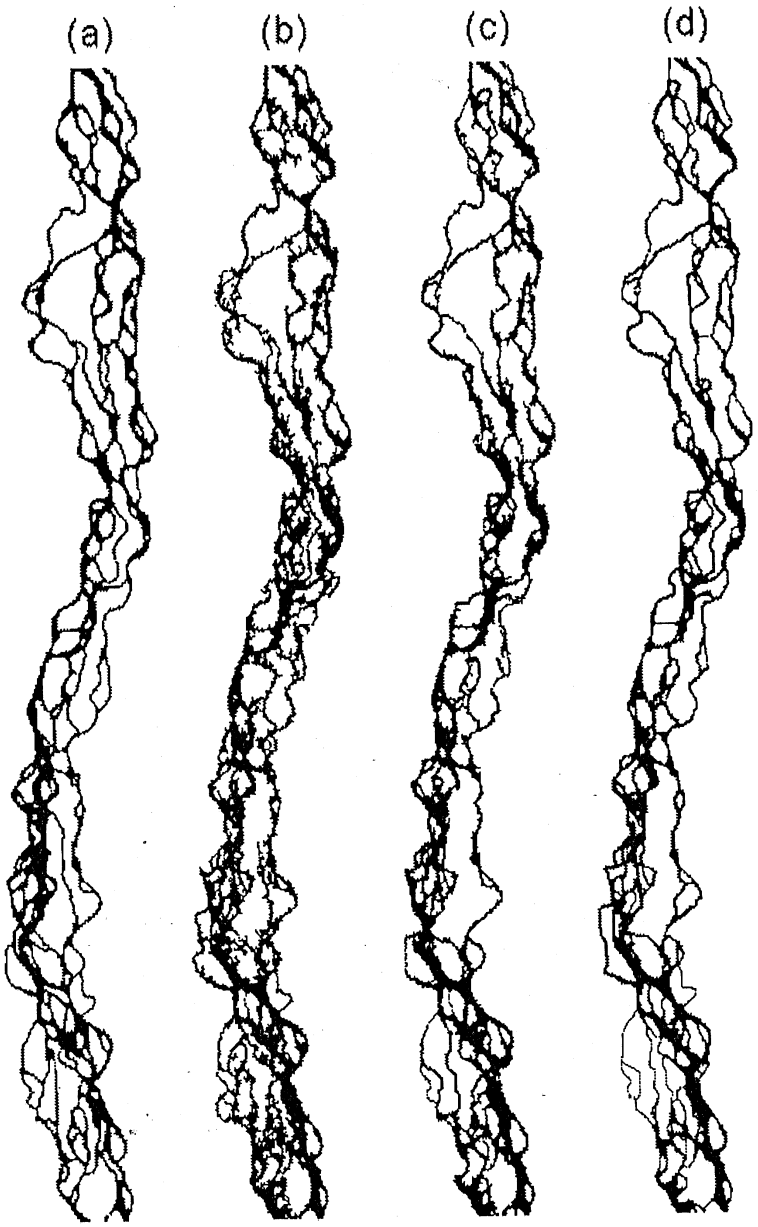

Figure 7. Braided river patterns of the Tanana River, reach A, image ID 152993100, for various extraction methodologies: (a) digitized tracing, (b) semiautomated level 1, (c) semiautomated level 2, and (d) semiautomated level 3.

tween the plots that correspond to the different extraction methodologies as compared to that of the ground truth. For example, the level 1 pattern (Figure 8b) does not include features which give $\partial z(x, y)/\partial y$, $\partial z(x, y)/\partial x$ values in the upper left region (boxed area) of the plot as do levels 2 and 3 and the traced patterns (see Figures 8a, 8c, and 8d). This region represents features which were most likely lost because of overfill into inactive channels, which caused jagged edges and discontinuity in the level 1 extracted pattern. This sensitivity in the level 1 pattern versus the level 2 and 3 patterns should be recognized and care should be taken in making the braided river patterns look somewhat natural. The similarity in the plots of the dependence of $\partial z(x, y)/\partial y$ versus $\partial z(x, y)/\partial x$ for semiautomated levels 2 and 3 to each other and to that of the traced pattern shows that once a reasonable pattern is obtained, further image cleanup, although producing a more visually appealing result, is insignificant for spatial scaling analysis and inferences. This signifies a robustness in the manual part of the semiautomated extraction procedure in that a few superfluous features (e.g., mild roughness and small gaps in connectivity) do not adversely affect the scaling analysis results.

To estimate the scaling exponents ν_x and ν_y, the best fit lines in the plots $\partial z(x, y)/\partial y$ versus $\partial z(x, y)/\partial x$ are needed. This was done using the algorithm of *Alciatore and Miranda* [1995] mentioned in section 3. The estimated scaling exponents are reported in Table 4 along with the measures of linear dependence. The ν_x and ν_y values were 0.72–0.75 and 0.44–0.48,

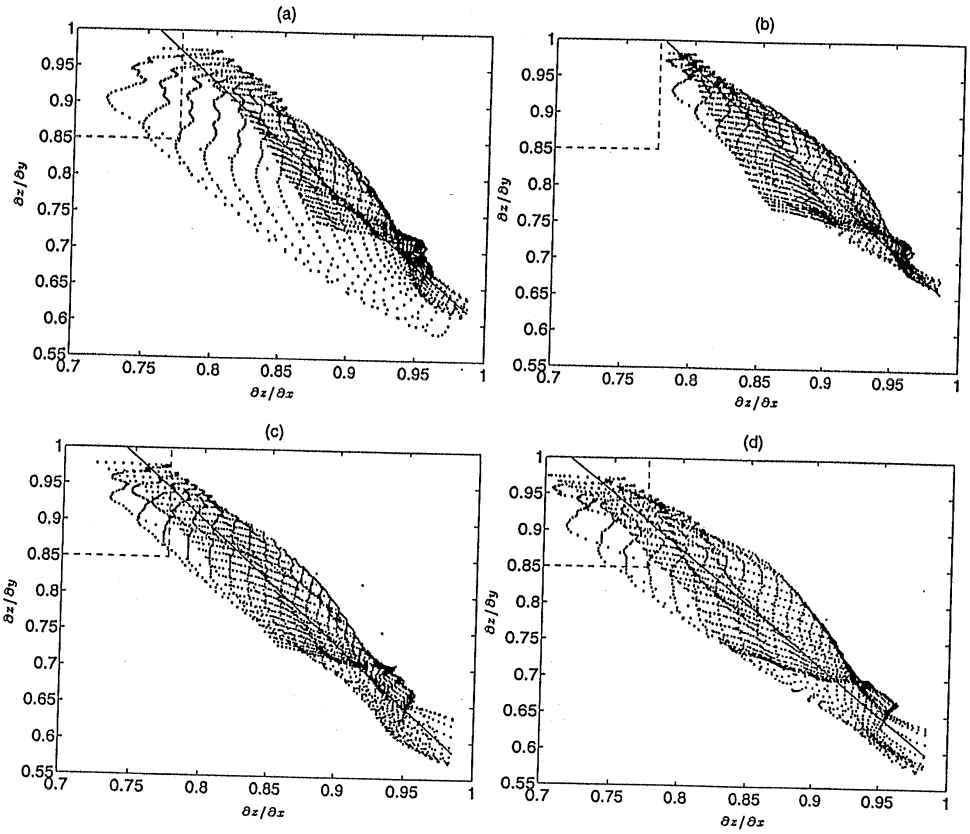

Figure 8. Dependence of $\partial z(x, y)/\partial y$ versus $\partial z(x, y)/\partial x$ for (a) digitized tracing, (b) semiautomated level 1, (c) semiautomated level 2, and (d) semiautomated level 3 of the Tanana River, reach A, image ID 152993100. Fractal exponents ν_x and ν_y are estimated from the best fit line and are shown in Table 4.

respectively. The closeness in spatial scaling exponents along with the visual similarity of the patterns validates the semiautomated braided river extraction methodology developed for use with full-resolution SAR images. The semiautomated procedure used for this study was constrained to greater than or equal to manual interpretation level 2.

Appendix B: Relationship of Discharge and Effective Width

Recently, *Smith et al.* [1995, 1996] derived for braided rivers an empirical relationship between discharge Q and "effective width" W_e, where W_e is defined as the total area covered by water in a control section divided by the length of that section. The relationship followed a typical power law form where W_e equalled a coefficient times the discharge raised to a power. The coefficient and discharge exponent were found to vary from river to river. These power functions were determined based on satellite-derived rating curves. *Smith et al.* [1996] derived such an empirical relationship for the Tanana River as

$$W_e = 50.45Q^{0.38} \qquad (7)$$

where W_e is in meters and Q is in cubic meters per second.

The flow rates listed in Table 1 correspond to gaged measurements taken from the Tanana River at Fairbanks, Alaska. One of the four reaches analyzed in this study is located just upstream of Fairbanks. A test was performed to compare the W_e computed from the braided river patterns extracted using the semiautomated scheme to W_e computed using the known discharge and the relationship developed by *Smith et al.* [1996].

For example, the effective width calculated for the May 31, 1993, extracted braided river pattern from SAR was 608 m.

Table 4. Spatial Scaling for Various Extraction Methodologies

Scheme	ν_x	ν_y	Correlation Coefficient	Average |error|	Standard Deviation |error|
Traced	0.74	0.44	−0.895	0.0166	0.0152
SemiAutomated					
Level 1	0.72	0.44	−0.934	0.0125	0.0099
Level 2	0.75	0.44	−0.947	0.0144	0.0094
Level 3	0.72	0.48	−0.933	0.0179	0.0113

Using the derived $W_e - Q$ relationship and the known discharge of 35,300 cfs (1000 cubic meters per second), a W_e of 696 m was obtained. The difference between these two is ~90 m in terms of effective width. This is an acceptable range of error considering the resolution and geolocation accuracy of SAR and the fact that the $W_e - Q$ relationships are empirically derived. This difference in W_e corresponds to a difference in estimated discharge of 300 $m^3 s^{-1}$. The error in the relationship derived by *Smith et al.* [1996] for the Tanana River was stated to range from tens to hundreds of cubic meters per second. This is further evidence that the empirical relationship derived for the Tanana River holds within the specified range and with relative robustness to the braided river pattern used to compute W_e since the pattern used by Smith et al. and the pattern used here were derived in somewhat different ways [see *Smith et al.* 1995, 1996].

The measured flow rate of the October 18, 1993, scene is unknown. On the basis of the agreement between the W_e of the semiautomated extracted patterns with the relationships developed by *Smith et al.* [1996] the discharge for this scene can be estimated using the computed effective width. The discharge estimated using (7) was 220 $m^3 s^{-1}$ (or 7800 $ft^3 s^{-1}$).

Acknowledgments. This research was supported by NSF grant EAR-9628393 and NASA grant NAG5-6191. ERS-1 data were acquired by the European Space Agency and provided by NASA through the Alaska SAR Facility. We thank the Minnesota Supercomputer Institute for providing computer facilities for our research. We also thank J. Bell, of the University of Minnesota, who allowed our use of computing facilities for image processing and L. Smith of the Department of Geography, UCLA, for helpful discussions and insights regarding SAR applications.

References

Alciatore, D., and R. Miranda, The best least-squares line fit, in *Graphics Gems V*, edited by A. W. Paeth, pp. 91–97, Academic, San Diego, Calif., 1995.

Ashmore, P., and G. Parker, Confluence scour in coarse braided streams, *Water Resour. Res.*, *19*, 392–402, 1983.

Ashmore, P. E., R. I. Ferguson, K. L. Prestegaard, P. J. Ashworth, and C. Paola, Secondary flow in anabranch confluences of a braided, gravel-bed stream, *Earth Surf. Processes Landforms*, *17*, 299–311, 1992.

Beauvais, A. A., and D. R. Montgomery, Influence of valley type on the scaling properties of river planforms, *Water Resour. Res.*, *32*, 1441–1448, 1996.

Best, J. L., The morphology of river channel confluences, *Prog. Phys. Geogr.*, *10*, 157–174, 1986.

Best, J. L., Sediment transport and bed morphology at river channel confluences, *Sedimentology*, *35*, 481–498, 1988.

Bristow, C. S., J. L. Best, and A. G. Roy, Morphology and facies models of channel confluences, in *Alluvial Sedimentation*, edited by M. Marzo and C. Puigdefabregas, pp. 91–100, Blackwell Sci., Cambridge, Mass., 1993.

Frost, V. S., J. A. Stiles, K. S. Shanmugan, and J. C. Holtzman, A model for radar images and its application to adaptive digital filtering of multiplicative noise, *IEEE Trans. Pattern Anal. Mach. Intel.*, *4*, 157–166, 1982.

Hagg, W., and M. Sties, Efficient speckle filtering of SAR images, in *International Geoscience and Remote Sensing Symposium*, vol. 4, pp. 2140–2142, Calif. Inst. of Technol., Pasadena, 1994.

Jensen, J. R., *Introductory Digital Image Processing: A Remote Sensing Perspective*, Prentice Hall, Englewood Cliffs, N. J., 1996.

La Barbera, P., and R. Rosso, On the fractal dimension of stream networks, *Water Resour. Res.*, *25*, 735–741, 1989.

Lopes, A., R. Touzi, and E. Nezry, Adaptive speckle filters and scene heterogeneity, *IEEE Trans. Geosci. Remote Sens.*, *28*, 992–1000, 1990.

Mosley, M. P., An experimental study of channel confluences, *J. Geol.*, *84*, 535–562, 1976.

Mosley, M. P., Stream junctions: A probable location for bedrock placers, *Econ. Geol.*, *72*, 691–697, 1977.

Murray, A. B., and C. Paola, A cellular model of braided rivers, *Nature*, *371*, 54–57, 1994.

Nikora, V. I., Fractal structures of river plan forms, *Water Resour. Res.*, *27*, 1327–1333, 1991.

Nikora, V. I., D. M. Hicks, G. M. Smart, and D. A. Noever, Some fractal properties of braided rivers, paper presented at Second International Symposium on Fractals and Dynamic Systems in Geoscience, Johann Wolfgang Goethe-Univ., Frankfurt am Main, Germany, 1995.

Nykanen, D. K., Study of the morphology and spatial scaling of braided rivers using synthetic aperture radar imagery, M. S. thesis, Univ. of Minnesota, Minneapolis St. Paul, 1997.

Oliver, C. J., Information from SAR images, *J. Phys. D Appl. Phys.*, *24*, 1493–1514, 1991.

Olmsted, C., Alaska SAR facility scientific user's guide, *Rep. ASF-SD-003*, Alaska SAR Facility, Fairbanks, July 1993.

Peckham, S. D., New results for self-similar trees with application to river networks, *Water Resour. Res.*, *31*, 1023–1029, 1995.

Robert, A., Bed configuration and microscale processes in alluvial channels, *Prog. Phys. Geogr.*, *17*, 123–136, 1993.

Sapozhnikov, V. B., and E. Foufoula-Georgiou, Study of self-similar and self-affine objects using logarithmic correlation integral, *J. Phys. A Math. Gen.*, *28*, 559–571, 1995.

Sapozhnikov, V. B., and E. Foufoula-Georgiou, Self-affinity in braided rivers, *Water Resour. Res.*, *32*, 1429–1439, 1996.

Sapozhnikov, V. B., and E. Foufoula-Georgiou, Experimental evidence of dynamic scaling and indications of self-organized criticality in braided rivers, *Water Resour. Res.*, *33*, 1983–1991, 1997.

Sapozhnikov, V. B., and V. I. Nikora, Simple computer model of a fractal river network with fractal individual watercourse, *J. Phys. A Math. Gen.*, *26*, L623–L627, 1993.

Shi, Z., and K. B. Fung, A comparison of digital speckle filters, in *Proceedings of the International Geoscience and Remote Sensing Symposium*, vol. 4, pp. 2129–2133, Calif. Inst. of Technol., Pasadena, 1994.

Smith, L. C., B. L. Isacks, R. R. Forster, A. L. Bloom, and I. Presuss, Estimation of discharge from braided glacial rivers using ERS 1 synthetic aperture radar: First results, *Water Resour. Res.*, *31*, 1325–1329, 1995.

Smith, L. C., B. L. Isacks, A. L. Bloom, and A. B. Murray, Estimation of discharge from three braided rivers using synthetic aperture radar satellite imagery: Potential applications to ungaged basins, *Water Resour. Res.*, *32*, 2031–2034, 1996.

Tarboton, D. G., R. L. Bras, and I. Rodriguez-Iturbe, The fractal nature of river networks, *Water Resour. Res.*, *24*, 1317–1322, 1988.

E. Foufoula-Georgiou, D. K. Nykanen, and V. B. Sapozhnikov, St. Anthony Falls Laboratory, Mississippi River at Third Avenue SE, University of Minnesota, Minneapolis, MN 55414-2196. (e-mail: efi@mykonos.safhl.umn.edu; deborah@mykonos.safhl.umn.edu; sapoz001@maroon.tc.umn.edu)

(Received August 1, 1997; revised March 13, 1998; accepted March 17, 1998.)

WATER RESOURCES RESEARCH, VOL. 34, NO. 4, PAGES 863–867, APRIL 1998

ST. ANTHONY FALLS LABORATORY
Technical paper No. 549, Series A

Anisotropic scaling in braided rivers: An integrated theoretical framework and results from application to an experimental river

Efi Foufoula-Georgiou and Victor B. Sapozhnikov

St. Anthony Falls Laboratory, University of Minnesota, Minneapolis

Abstract. Dynamic scaling in braided rivers is reexamined under an extended theoretical framework, developed herein, which explicitly incorporates the self-affinity (scaling anisotropy) in the spatial structure of braided rivers. It is shown that in structures exhibiting anisotropic spatial scaling, dynamic scaling (if present) is necessarily anisotropic. Through analysis of the behavior of an experimental braided river, the presence of anisotropic dynamic scaling in braided rivers was revealed. This implies that there exists a pair of dynamic exponents z_x and z_y enabling one to rescale space (differently in the direction X of the slope and in the perpendicular direction Y) and time, such that the evolution of a smaller part of a braided river looks statistically identical to that of a larger one. The presence of such a space-time scale invariance provides an integrated framework for describing simultaneously the spatial and temporal structure of braided rivers and may be explored toward statistical prediction of large and rare changes from the statistics of smaller and frequent ones.

1. Introduction

The morphology and dynamics of braided rivers have been studied over the years using river-mechanics, experimental, empirical, and computer-simulation approaches [e.g., see *Howard et al.*, 1970; *Schumm and Khan*, 1972; *Ashmore*, 1982, 1991; *Kuhnle*, 1981; *Leddy et al.*, 1993; *Barzini and Ball*, 1993; *Murray and Paola*, 1994; *Smith et al.*, 1995, 1996]. In a recent study, *Sapozhnikov and Foufoula-Georgiou* [1997] analyzed the spatio-temporal structure of braided rivers and presented evidence that they exhibit dynamic scaling. Dynamic scaling implies that a small part of a braided river evolves identically (in a statistical sense) to a larger one provided that time is renormalized by a factor depending only on the ratio of the spatial scales of those parts. In those developments, *Sapozhnikov and Foufoula-Georgiou* [1997] considered braided rivers as self-similar objects characterized by one fractal dimension D. However, it is known [*Sapozhnikov and Foufoula-Georgiou*, 1996] that braided rivers exhibit spatial scaling anisotropy, i.e., are objects characterized by two scaling exponents ν_x and ν_y, or equivalently two fractal dimensions D_G and D_L (see *Sapozhnikov and Foufoula-Georgiou* [1995] for relations between D_G, D_L, and ν_x, ν_y). The reason that self-similarity was assumed in the dynamic scaling developments of *Sapozhnikov and Foufoula-Georgiou* [1997] was that no theoretical framework existed yet to integrate the notions of dynamic scaling and self-affinity.

The scope of this paper is to present such a framework, i.e., extend the theory of dynamic scaling to self-affine objects, and report the results of reanalyzing braided rivers under this integrated and more consistent framework. To avoid repetition, relies heavily on the paper of *Sapozhnikov and Foufoula-Georgiou* [1997] for the basic ideas on dynamic scaling and the details of the experimental setting. The reader is advised to read the present paper in conjunction with the previous one for a complete understanding of this work.

Paper number 98WR00216.
0043-1397/98/98WR-00216$09.00

2. Dynamic Scaling in Self-Affine Objects

The idea of dynamic scaling in a self-affine object can be qualitatively presented as follows. Suppose there is a self-affine object characterized by fractal exponents ν_x and ν_y, which evolves in time (such that its fractal characteristics are preserved at all times). The self-affinity (anisotropic spatial scaling) of the object implies that if one takes a picture of a part of the object of size $X_1 \times Y_1$, and a picture of a part of the same object of size $X_2 \times Y_2$, such that

$$\left(\frac{X_2}{X_1}\right)^{1/\nu_x} = \left(\frac{Y_2}{Y_1}\right)^{1/\nu_y}, \tag{1}$$

and projects these two parts onto two screens of the same size. (this would require different stretching of each image in X and Y directions) the images on the screens will be statistically indistinguishable. Suppose now that one makes another step and, instead of taking still pictures, videotapes the two regions and observes the evolution of the images on the two screens. In contrast to the still pictures, the movies will not be statistically indistinguishable. The rate of evolution will be different (slower for the larger scale). If, however, there exists a pair of dynamic exponents z_x and z_y such that for every X_1, Y_1 and X_2, Y_2 satisfying (1) it is possible to rescale the time as

$$\frac{t_2}{t_1} = \left(\frac{X_2}{X_1}\right)^{z_x} = \left(\frac{Y_2}{Y_1}\right)^{z_y}, \tag{2}$$

or, in other words, to play the movies at different speeds, such that the rate of the evolution is the same on both screens, then we say that in addition to static (spatial) scaling the system also shows dynamic scaling. Comparison of (1) and (2) bounds the values of the fractal exponents ν_x, ν_y and the dynamic exponents z_x, z_y by

$$\frac{z_x}{z_y} = \frac{\nu_y}{\nu_x}. \tag{3}$$

Thus we see that dynamic scaling in self-affine objects is necessarily anisotropic.

Following the developments of *Sapozhnikov and Foufoula-Georgiou* [1997], let us characterize the evolution of a fractal stationary object by "changes" in its pattern, where changes are defined as parts of the space which were not occupied by the object at a certain moment of time but became occupied after some time lag t. Although changes in a river are three-dimensional, as is the river itself, we only considered in our previous work and here their horizontal projections. Thus changes in a braided river reflect parts of the river where water depth changed (including dry areas which became covered with water and water-covered areas which became exposed). Let $n(X, Y, x, y, t)$ denote the number of changes exceeding size x in the X direction and size y in the Y direction after some time lag t in a region of size $X \times Y$. Because the object is stationary and fractal, with constant fractal exponents ν_x and ν_y, the number of changes scales with the size of the observed region (see Appendix in *Sapozhnikov and Foufoula-Georgiou* [1997]) as

$$n(X_2, Y_2, x_1, y_1, t_1) = n(X_1, Y_1, x_1, y_1, t_1)\left(\frac{X_2}{X_1}\right)^{1/\nu_x}$$

$$= n(X_1, Y_1, x_1, y_1, t_1)\left(\frac{Y_2}{Y_1}\right)^{1/\nu_y} \tag{4}$$

provided that (1) holds.

The presence of dynamic scaling, implying the same rate of evolution after rescaling space and time according to (2), means that if (2) and (1) hold, the number of changes exceeding the same relative size $x \times y$ such that

$$\frac{x_1}{x_2} = \frac{X_1}{X_2}, \qquad \frac{y_1}{y_2} = \frac{Y_1}{Y_2} \tag{5}$$

is the same on both screens, i.e.,

$$n(X_1, Y_1, x_1, y_1, t_1) = n(X_2, Y_2, x_2, y_2, t_2) \tag{6}$$

Suppose now that we fix the scale of the region of interest to $X_2 \times Y_2$ and instead of zooming to different scales we follow the distribution of changes in this region as the object evolves. From (6) and (4) we obtain for the distribution of changes in the region $X_2 \times Y_2$

$$n(X_2, Y_2, x_2, y_2, t_2) = n(X_2, Y_2, x_1, y_1, t_1)\left(\frac{X_1}{X_2}\right)^{1/\nu_x}$$

$$= n(X_2, Y_2, x_1, y_1, t_1)\left(\frac{Y_1}{Y_2}\right)^{1/\nu_y} \tag{7}$$

provided that (1) and (2) hold. The variables X_2 and Y_2 are the same in both sides of (7) and therefore can now be dropped. Replacing X_1/X_2 by x_1/x_2 and Y_1/Y_2 by y_1/y_2 from (5) yields

$$x_1^{1/\nu_x} n(x_1, y_1, t_1) = x_2^{1/\nu_x} n(x_2, y_2, t_2) \tag{8}$$

$$y_1^{1/\nu_y} n(x_1, y_1, t_1) = y_2^{1/\nu_y} n(x_2, y_2, t_2). \tag{9}$$

Finally, we obtain the condition for the distribution of changes in a system showing dynamic scaling: there exists a pair of dynamic exponents z_x and z_y (bound by (3)) such that if (2) is true, i.e., $t/X^{z_x} = \text{const}$ and $t/Y^{z_y} = \text{const}$ (which according to (5) also implies $t/x^{z_x} = \text{const}$ and $t/y^{z_y} = \text{const}$), then $x^{1/\nu_x} n(x, y, t) = \text{const}$ and $y^{1/\nu_y} n(x, y, t) = \text{const}$, or in other words the distribution of changes in such systems can be expressed as

$$n(x, y, t) = x^{-1/\nu_x} g_x\left(\frac{t}{x^{z_x}}, \frac{t}{y^{z_y}}\right) = y^{-1/\nu_x} g_y\left(\frac{t}{x^{z_x}}, \frac{t}{y^{z_y}}\right), \tag{10}$$

where $g_x(\cdot)$ and $g_y(\cdot)$ are some functions.

The two conditions: $t/x^{z_x} = \text{const}$ and $t/y^{z_y} = \text{const}$, can be presented as $t/x^{z_x} = \text{const}$ and $x^{z_x}/y^{z_y} = \text{const}$. With (3) the second condition can be rewritten as $x^{1/\nu_x}/y^{1/\nu_y} = \text{const}$ and (10) can be rewritten as

$$n(x, y, t) = x^{-1/\nu_x} h_x\left(\frac{t}{x^{z_x}}, \frac{y^{1/\nu_y}}{x^{1/\nu_x}}\right) = y^{-1/\nu_y} h_y\left(\frac{t}{y^{z_y}}, \frac{x^{1/\nu_x}}{y^{1/\nu_y}}\right). \tag{11}$$

Note that (10) and (11) are equivalent to each other.

Since $n(x, y, t)$ is a joint probability of exceedance, the distribution $n(x, t)$ for all possible values of y, is $n(x, t) \equiv n(x, 0, t)$. Therefore from (11) we obtain

$$n(x' > x, t) \equiv n(x, t) = x^{-1/\nu_x} h_x\left(\frac{t}{x^{z_x}}, 0\right) = x^{-1/\nu_x} f_x\left(\frac{t}{x^{z_x}}\right). \tag{12}$$

Similarly,

$$n(y' > y, t) \equiv n(y, t) = y^{-1/\nu_y} f_y\left(\frac{t}{y^{z_y}}\right). \tag{13}$$

Note that $n(x' > x, t)$ is the number of changes of size greater than x in the X direction (and having any size in the Y direction) and $n(y' > y, t)$ has similar meaning for the Y direction. Equations (12) and (13) are the equations of dynamic scaling of a self-affine object. They imply that if a self-affine object of scaling exponents ν_x and ν_y exhibits dynamic scaling, then there exist exponents z_x and z_y such that $n(x' > x, t)x^{1/\nu_x}$ versus t/x^{z_x} and $n(y' > y, t)y^{1/\nu_y}$ versus t/y^{z_y} collapse to the same curves f_x and f_y, respectively, for all x, y, t.

3. Analysis of an Experimental Braided River

Recognizing the lack of data for studying the evolution of natural braided rivers, *Sapozhnikov and Foufoula-Georgiou* [1997] proposed as a starting point to analyze the evolution of experimental braided rivers so that theories can be developed and tested until more accurate and frequent remote sensing data are available for application of these theories to natural systems. Thus, a small experimental basin of 5 m × 0.75 m was established at the St. Anthony Falls Laboratory and experimental braided rivers were successfully produced and monitored over time. The details of the experimental and monitoring procedures were extensively discussed by *Sapozhnikov and Foufoula-Georgiou* [1997] and are not repeated here. The same data of "changes" as in our previous paper are used here but subject to analysis under the extended theory of anisotropic dynamic scaling as developed in the previous section. For example, from the monitored changes over time the probabilities of exceedance $n(x' > x, t)$ and $n(y' > y, t)$ as needed in (12) and (13) were estimated now instead of the probability $n(l' > l, t)$, $l = \sqrt{\text{area}}$ used in the self-similar dynamic scaling analysis. The X direction is the direction of the slope and Y is the perpendicular direction.

It is noted that in principle, if the self-affine exponents ν_x and ν_y could be estimated directly from the river pattern using for example, the Logarithmic Correlation Integral (LCI)

method developed by the authors earlier [*Sapozhnikov and Foufoula-Georgiou*, 1995], then the dynamic exponents z_x and z_y could be estimated from (12) and (13) directly. That is, by nonlinear optimization the value of z_x that minimizes the spread of the points $n(x' > x, t)x^{1/\nu_x}$ versus t/x^{z_x} (so that all curves collapse to a single curve f_x) can be found. The z_y exponent could be found in the same way. However, as in the self-similar analysis we preferred to take advantage of a stepwise estimation approach suggested by the data. An additional reason for taking such an approach in the self-affine case is that ν_x and ν_y presented difficulty in their direct estimation from the experimental rivers because it was hard to separate the river from the colored sediment in the video images (dye was introduced in the water to monitor the evolution of the river). Therefore thus tracings of the river patterns could not reveal small channels thus restricting the range of analyzed scales. Note that determining the changes in the river pattern was not a problem because the colored sediment was zeroed by subtraction (see *Sapozhnikov and Foufoula-Georgiou* [1997] for details).

Changes in the experimental braided rivers, e.g., see Figure 2 of *Sapozhnikov and Foufoula-Georgiou* [1997], were followed over time and the sizes x and y of each change in the direction X of the slope and in the perpendicular direction Y were estimated as the root-mean square of the deviation of pixels (x_i, y_i) constituting the change, from the center of mass of the change (x_c, y_c): $x = [1/N \sum_{i=1}^{N} (x_c - x_i)^2]^{1/2}$ and $y = [1/N \sum_{i=1}^{N} (y_c - y_i)^2]^{1/2}$, correspondingly, where N is the number of the pixels in the change. Then cumulative probability distributions of the sizes x and y of changes were estimated. The distribution of changes was followed over time and Figure 1 shows these distributions for time lags of 3, 4, 5, 7, 9 and 15 s. Notice that the number of changes of size greater than x or y in a time lag t, $n(x' > x, t)$ and $n(y' > y, t)$, respectively, are plotted instead of the probability. As can be seen from Figure 1, these distributions can be well approximated by power laws for different time lags and the slopes of the log-log plots of the distributions found for different time lags are very close. Thus the distributions can be presented in the form

$$n(x' > x, t) = \psi_x(t)x^{-k_x}, \tag{14}$$

$$n(y' > y, t) = \psi_y(t)y^{-k_y}, \tag{15}$$

where $\psi_x(t)$ and $\psi_y(t)$ are functions of time lag t. The log-log plots of $n(x' > x, t)x_x^k$ and $n(y' > y, t)y_y^k$ against t shown in Figure 2 suggest that for small values of t, $\psi_x(t)$ and $\psi_y(t)$ show power law dependencies

$$\psi_x(t) \sim t^{\beta_x} \tag{16}$$

$$\psi_y(t) \sim t^{\beta_y}. \tag{17}$$

Combining (14) and (16), and (15) and (17) we see that

$$n(x' > x, t) \sim t^{\beta_x}x^{-k_x} \tag{18}$$

$$n(y' > y, t) \sim t^{\beta_y}y^{-k_y}. \tag{19}$$

For small values of t, such that the power law relationships (16) and (17) hold, the functions f_x and f_y can be approximated by power laws. Thus, comparing the conditions of dynamic scaling (12) and (13) with (18) and (19), results in

$$z_x = (k_x - 1/\nu_x)/\beta_x \tag{20}$$

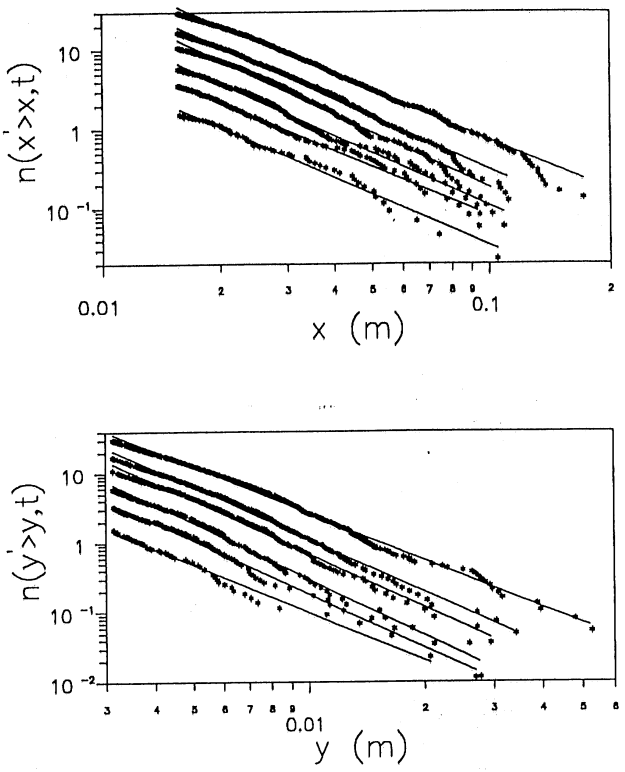

Figure 1. Number of changes of size greater than x, $n(x' > x, t)$, and greater than y, $n(y' > y, t)$, in the direction of slope X and the perpendicular direction Y, respectively. The numbers of changes are plotted for time lags t of 3, 4, 5, 7, 9, and 15 s (from bottom to top), and the solid lines represent the best least squares fit lines for each time lag t. Note that the numbers of changes are fractional numbers, some less than one, since they represent average values over multiple realizations, each realization corresponding to a particular time lag but to different time instances. The plots suggest that the distributions have broad central regions that are well approximated by power laws, and their slopes for different time lags are very close to each other for each of the two directions.

$$z_y = (k_y - 1/\nu_y)/\beta_y. \tag{21}$$

We estimated the values of k_x and k_y from the power-law distributions of changes (Figure 1 and (14) and (15)) as $k_x = 2.17$ and $k_y = 2.47$ (k_x and k_y represent the average of the slopes of the corresponding five lines in Figure 1). The values of β_x and β_y were estimated from the power law dependence of $\psi_x(t)$ and $\psi_y(t)$ (Figure 2 and (16) and (17)) as $\beta_x = 1.68$ and $\beta_y = 1.95$.

As mentioned before, our experimental data did not permit a direct estimation of ν_x and ν_y via the LCI method. However, we were able to estimate the fractal dimension of the experimental braided river D from one pattern of the river by the "mass-in-a-box" method (which is much less data demanding) as 1.7 (see Figure 5 of *Sapozhnikov and Foufoula-Georgiou* [1997]). This value of D relates to ν_x and ν_y by the expression [see *Sapozhnikov and Foufoula-Georgiou*, 1995]

$$D_G \equiv D = (\nu_y - \nu_x + 1)/\nu_y. \tag{22}$$

Combining the above equation with (3), (20), and (21) results in

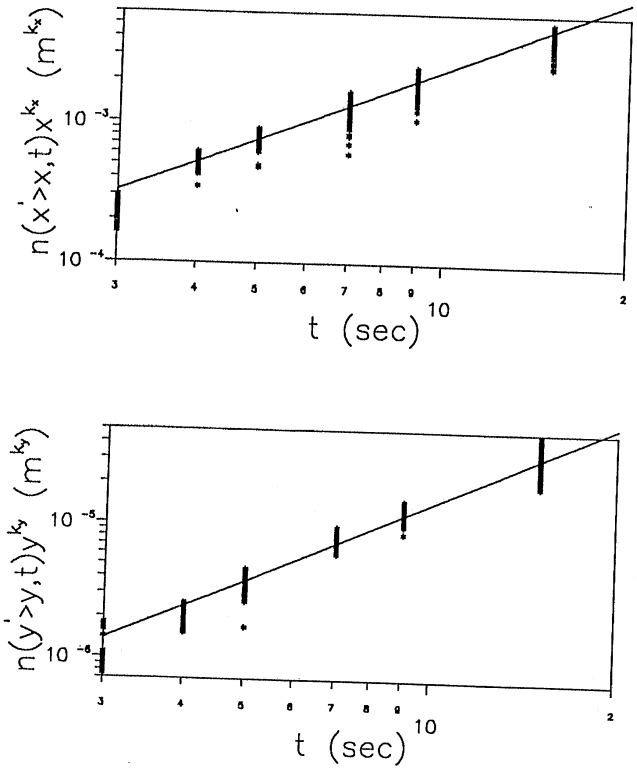

Figure 2. Evolution of the distribution of changes shown by the time dependence of the functions $n(x' > x, t)x^{k_x}$ and $n(y' > y, t)y^{k_y}$ for the X and Y directions, respectively. For every time lag, each point on the plots shows the (rescaled by x^{k_x} or y^{k_y}) number of changes exceeding size x or y, respectively. The plots suggest that power law dependence applies in both directions well over a major part of the range.

$$\nu_x = \frac{k_y\beta_x + (\beta_y - \beta_x)(D-1)}{k_x\beta_y(D-1) + k_y\beta_x} \tag{23}$$

$$\nu_x = \frac{\beta_x - \beta_y + k_x\beta_y}{k_x\beta_y(D-1) + k_y\beta_x}. \tag{24}$$

The above equations enabled us to estimate indirectly the fractal exponents of the experimental river as $\nu_x = 0.61$ and $\nu_y = 0.55$. Finally, from (20) and (21) we found the dynamic exponents of the braided river as $z_x = 0.32$ and $z_y = 0.35$. Thus it was concluded that the experimental river exhibits anisotropic dynamic scaling with anisotropy ratio $z_y/z_x = \nu_x/\nu_y = 1.1$.

It is important to note that although for small time lags Figure 2 shows reasonably good temporal scaling, it deviates from the power law behavior for bigger time lags (i.e., for time lags $t > 15$ s not shown in Figure 2). It should be stressed however, that this does not indicate the loss of dynamic scaling expressed by the general equations for dynamic scaling (12) and (13). In fact, even though the functions f_x and f_y, from (12) and (13), follow power laws at small values of the argument, they have to level off at big values of the argument. Indeed, for big enough time lags such that the object decorrelates completely between the snapshots, the difference between the two patterns of the object (and therefore the distribution of changes $n(x' > x, t)$ and $n(y' > y, t)$) does not depend on time anymore. This necessarily leads to the loss of power law dependencies in relations (16) and (17) but not loss of dynamic scaling. In fact, to confirm that the distributions corresponding to different time lags satisfy the general equations for dynamic scaling (12) and (13), we plotted for the estimated values of ν_x, ν_y, z_x, and z_y, the values of $n(x' > x, t)x^{-1/\nu_x}$ versus t/x^{z_x}, and $n(y' > y, t)y^{-1/\nu_y}$ versus t/y^{z_y}, for different time lags up to 1 min, in Figure 3. As one can see, in both cases all curves satisfactorily collapse to a single curve (the $f_x(t/x^{z_x})$ and $f_y(t/y^{z_y})$ curve, respectively).

This further corroborates the presence of dynamic scaling and the adequacy of the estimated dynamic exponents $z_x = 0.32$ and $z_y = 0.35$ in the experimental braided river. Notice that this last confirmation of dynamic scaling, i.e., that the general equations for dynamic scaling (12) and (13) hold, did not directly use the assumption of power-law distribution of changes (equations (14) and (15)) or power law dependence of $\psi_x(t)$ and $\psi_y(t)$ for small values of t (equations (16) and (17)). These two special forms of dependencies (suggested directly from the experimental data in Figures 1 and 2) were conveniently used only to estimate z_x and z_y in a stepwise manner via equations (20) and (21). After the values of z_x and z_y were estimated, plotting $n(x' > x, t)x^{-1/\nu_x}$ versus t/x^{z_x} and $n(y' > y, t)y^{-1/\nu_y}$ versus t/y^{z_y}, and seeing that in each case all curves collapse to one, the f_x or f_y curve respectively, provides an additional and independent evidence for anisotropic dynamic scaling.

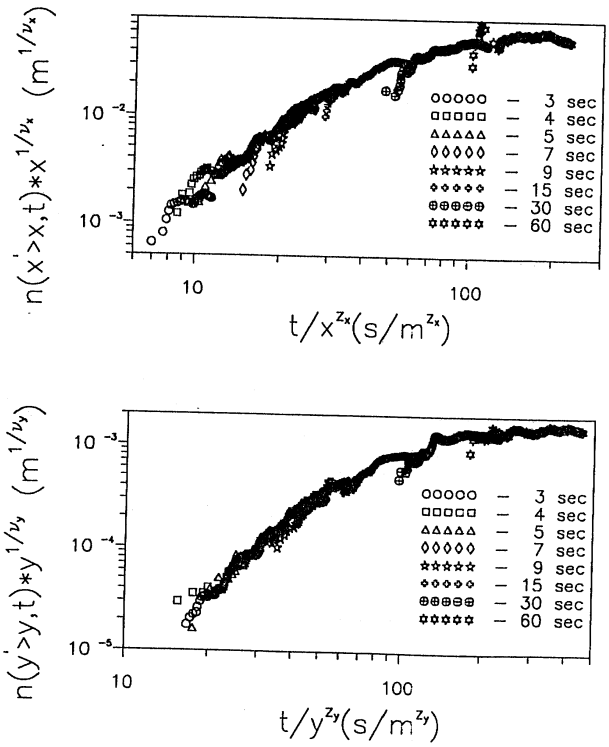

Figure 3. Plot showing that the rescaled distributions of changes collapse into a single curve, f_x and f_y, for each direction X and Y, respectively. Time lags from 3 to 60 s (bottom left to top right) are shown in each plot. This further corroborates the presence of anisotropic dynamic scaling and the adequacy of the estimated values of z_x and z_y.

4. Discussion and Conclusions

In a previous study by *Sapozhnikov and Foufoula-Georgiou* [1997], evidence was presented that braided rivers exhibit dynamic scaling with scaling exponent $z \simeq 0.5$. In that study, braided rivers were analyzed as self-similar objects despite the existing evidence that they exhibit spatial scaling anisotropy, i.e., that they are self-affine objects [*Sapozhnikov and Foufoula-Georgiou*, 1996]. The reason for exploring dynamic scaling in braided rivers within the self-similarity framework first, was that developing the corresponding theory was easier conceptually in that case and its extension to self-affinity was not trivial. The results were interpreted considering D (the fractal dimension of a self-similar object) as a surrogate parameter for D_G (the global fractal dimension of a self-affine object) which relates to ν_x and ν_y via (22).

In this paper, the theoretical framework for describing dynamic scaling was extended to self-affine objects and was applied to the same experimental braided river data as in *Sapozhnikov and Foufoula-Georgiou* [1997]. The results indicated the presence of anisotropic dynamic scaling in braided rivers and gave us estimates of the dynamic exponents $z_x = 0.32$ and $z_y = 0.35$. The approach presented in this paper is more general than the one by *Sapozhnikov and Foufoula-Georgiou* [1997] as it is capable of taking into account the self-affinity of the analyzed object. At the same time, it can also be used for the analysis of self-similar objects as a special case. We consider this approach more consistent for the analysis of braided rivers and believe that it is the values of z_x and z_y (rather than the single value of z) that really characterize the dynamic scaling in braided rivers.

The physical interpretation of the dynamic exponent z was extensively discussed by *Sapozhnikov and Foufoula-Georgiou* [1997] and was interpreted as an indication that evolution of small channel patterns is to a large extent forced by the evolution of larger channels. The exact same interpretation applies here for the z_x and z_y values, each one associated with the evolution of channels along the slope and in perpendicular direction, respectively.

It should be noted that in the experimental river, the estimated scaling anisotropy parameter $\nu_x/\nu_y = 1.1$ is considerably lower than the value of 1.4 to 1.5 estimated for natural rivers using the LCI method. It remains to be determined whether this discrepancy reflects differences in the spatial structure of natural versus laboratory produced rivers or is due to the differences in the estimation methods (one based on the static images only versus the other based on system dynamics). It is emphasized that in this work the fractal exponents ν_x and ν_y were not explicitly estimated from the braided river pattern as was done for natural rivers. Rather they were estimated implicitly from the analysis of changes. Thus the developed approach enables one to estimate the values of the fractal exponents of the spatial structure of a braided river from the dynamics of the river. As such, it takes advantage of the data collected during some time interval, rather than relying on the analysis of one snapshot only using, for example the LCI method. The two estimation methods should be compared to each other so that the properties of their estimates of ν_x and ν_y can be better understood. Such a comparison was not possible with the experimental data used in this study since, as was discussed, the dye procedure did not allow for many scales to be resolved in the static patterns, as needed for the LCI method. Different techniques giving higher-resolution experimental data or remote sensing images of natural braided rivers might permit such a comparison in the near future.

As a closing remark, it is noted that the presence of spatial and dynamic scaling was interpreted by *Sapozhnikov and Foufoula-Georgiou* [1997] as indication of self-organized criticality (SOC) in braided rivers. In view of the results of this article where anisotropic dynamic scaling was established, braided rivers are further interpreted as SOC systems showing spatio-temporal anisotropy in the critical state. To our knowledge, this type of behavior has never been found in classical systems i.e., systems brought to a critical state not by self-organization, but by tuning of a critical parameter (e.g., temperature). Thus a general problem that remains open to investigation is the development of theoretical frameworks for the description of the critical state of self-affine objects.

Acknowledgments. This research was supported by NSF grant EAR-9628393 and NASA grant NAG5-6191. Supercomputer resources were kindly provided by the Minnesota Supercomputer Institute.

References

Ashmore, P. E., Laboratory modelling of gravel braided stream morphology, *Earth Surf. Proc. Landforms*, *7*, 201–225, 1982.

Ashmore, P. E., How do gravel-bed rivers braid?, *Can. J. Earth Sci.*, *28*, 326–341, 1991.

Barzini, G. N., and R. C. Ball, Landscape evolution in flood—A mathematical model, *J. Phys. A Math. Gen.*, *26*, 6777–6787, 1993.

Howard, A. D., M. E. Keetch, and C. L. Vincent, Topological and geometrical properties of braided streams, *Water Resour. Res.*, *6*, 1674–1688, 1970.

Kuhnle, R. A., An experimental study of braiding in gravel-bed streams, M.S. thesis, Univ. Illinois, Chicago, 1981.

Leddy, J. O., P. J. Ashworth, and J. L. Best, Mechanisms of anabranch avulsion within gravel-bed braided rivers: Observations from a scaled physical model, in *Braided Rivers*, edited by J. L. Best and C. S. Bristow, pp. 119–127, Geol. Soc. of London, London, 1993.

Murray, A. B., and C. Paola, A cellular automata model of braided rivers, *Nature*, *371*, 54–57, 1994.

Sapozhnikov, V., and E. Foufoula-Georgiou, Study of self-similar and self-affine objects using logarithmic correlation integral, *J. Phys., A Math. Gen.*, *28*, 559–571, 1995.

Sapozhnikov, V., and E. Foufoula-Georgiou, Self-affinity in braided rivers, *Water Resour. Res.*, *32*, 1429–1439, 1996.

Sapozhnikov, V. B., and E. Foufoula-Georgiou, Experimental evidence of dynamic scaling and indications of self-organized criticality in braided rivers, *Water Resour. Res.*, *33*, 1983–1991, 1997.

Schumm, S. A., and H. R. Khan, Experimental study of channel patterns, *Geol. Soc. Am. Bull.*, *83*, 1755–1770, 1972.

Smith, L. C., B. L. Isacks, R. R. Forster, A. L. Bloom, and I. Preuss, Estimation of discharge from braided glacial rivers using ERS 1 synthetic aperture radar: First results, *Water Resour. Res.*, *31*, 1325–1329, 1995.

Smith, L. C., B. L. Isacks, A. L. Bloom, and A. B. Murray, Estimation of discharge from three braided rivers using synthetic aperture radar satellite imagery: Potential application to ungaged basins, *Water Resour. Res.*, *32*, 2031–2034, 1996.

E. Foufoula-Georgiou and V. B. Sapozhnikov, St. Anthony Falls Laboratory, University of Minnesota, Mississippi River at Third Avenue, SE, Minneapolis, MN 55414-2196. (efi@mykonos.safhl.umn.edu)

(Received November 18, 1997; revised January 12, 1998; accepted January 14, 1998.)

WATER RESOURCES RESEARCH, VOL. 33, NO. 8, PAGES 1983–1991, AUGUST 1997

Experimental evidence of dynamic scaling and indications of self-organized criticality in braided rivers

Victor B. Sapozhnikov and Efi Foufoula-Georgiou
Saint Anthony Falls Laboratory, University of Minnesota, Minneapolis

Abstract. The evolution of an experimental braided river produced in our laboratory has been monitored and analyzed. It has been shown that in addition to the spatial scaling revealed by *Sapozhnikov and Foufoula-Georgiou* [1996a], braided rivers also exhibit dynamic scaling. This implies that a smaller part of a braided river evolves identically (in the statistical sense) to a larger one provided the time is renormalized by a factor depending only on the ratio of the spatial scales of those parts. The small value of the estimated dynamic exponent z is interpreted as an indication that the evolution of small channels in a braided river system is to a large extent forced by the evolution of bigger channels. The presence of dynamic scaling is further interpreted as indicating that braided rivers may be in a critical state and behave as self-organized critical systems.

1. Introduction

In a recent paper [*Sapozhnikov and Foufoula-Georgiou*, 1996a] evidence was presented that natural braided rivers exhibit anisotropic scaling (self-affinity) in their geometrical structure, within a range of scales spanning the width of the narrowest channel to the width of the braid plain. In simple words, within these scales, if a small part of a braided river is stretched in a certain way along the mainstream direction and a certain different way along the perpendicular direction, then this stretched part looks statistically the same as a bigger part of the river. Such anisotropically scaled objects are called self-affine fractals and are characterized by two fractal exponents ν_x and ν_y. The ratio ν_x/ν_y characterizes the scaling anisotropy, and the fractal dimension $D = (\nu_y - \nu_x + 1)/\nu_y$ [e.g., see *Sapozhnikov and Foufoula-Georgiou*, 1995] indicates how densely the object fills the space.

In *Sapozhnikov and Foufoula-Georgiou* [1996a], three natural braided rivers of different scales and different hydrological and sedimentological characteristics (Aichilik and Hulahula in Alaska and Brahmaputra in Bangladesh) were analyzed for spatial scaling using the logarithmic correlation integral (LCI) method developed by *Sapozhnikov and Foufoula-Georgiou* [1995]. Interestingly enough, it was observed that despite their different scales (0.5–15 km in braid plain width), slopes (7×10^{-3}–8×10^{-5}), and types of bed material (gravel to sand), all three rivers exhibited anisotropic spatial scaling with almost the same fractal exponents: $\nu_x = 0.72$–0.74 and $\nu_y = 0.51$–0.52, the x axis being oriented along the river and the y axis being in the perpendicular direction. In simple terms this implies that if parts of a braided river are stretched by λ along the mainstream direction and by $\lambda^{\nu_y/\nu_x} \simeq \lambda^{0.7}$ along the perpendicular direction, the resulting images will look statistically similar to each other (similarity within a braided river). At the same time the invariance of ν_x and ν_y between braided rivers of different sizes and hydrology/sedimentology suggests that the same anisotropic scaling as above applied to different rivers will result in statistically similar images, apart, possibly, from a normalization factor to account for the different mass of each river. (Note that "mass" here refers to the area, i.e., number of pixels, covered with water.) The presence of such a statistical scale invariance in the spatial structure of braided rivers, apart from being interesting in its own right, might indicate the presence of universal features in the underlying mechanisms responsible for the formation of braided rivers and deserves further theoretical and experimental investigation.

Braided rivers, besides their complex geometry at any instant of time, are also highly dynamic systems characterized by intensive erosion, sediment transport and deposition, and frequent channel shifting as they evolve. Predicting the evolution of braided rivers in terms of frequency and magnitude of channel shifting is of paramount importance where hydraulic structures or land developments are planned or where field use must be made of maps and air photos. It is of great practical and theoretical value therefore to study the evolution of braided rivers in addition to their spatial structure. In view of the evidence for spatial (static) scaling in braided rivers the question is asked here as to whether they also show dynamic scaling. The presence of dynamic scaling would imply that space and time can be appropriately rescaled such that the evolution of the spatial structure of parts of the river of different size would be statistically indistinguishable. The presence of dynamic scaling would also provide a highly desirable integrated framework for studying, simultaneously, the spatial and temporal structure of braided rivers.

2. Dynamic Scaling: A Theoretical Framework

The idea of dynamic scaling can be qualitatively presented as follows. Suppose there is a fractal object, of fractal dimension D, which evolves in time such that its fractality is preserved at all times. In our case the fractal object is the spatial pattern of the active channels constituting a braided river which was shown to exhibit spatial scaling by *Sapozhnikov and Foufoula-Georgiou* [1996a]. The fractality (spatial scaling) of the object implies that if one takes a picture of a part of the object of size $L_1 \times L_1$ and a picture of a larger part of the same object of size $L_2 \times L_2$ and projects these two pictures onto two screens of the same size, the images on the screens will be statistically

Paper number 97WR01233.
0043-1397/97/97WR-01233$09.00

indistinguishable. Suppose now that one makes another step and, instead of taking still pictures, videotapes the two regions and observes the evolution of the images on the two screens. In contrast to the still pictures the movies will not be statistically indistinguishable. The rate of the evolution will be different (slower for the larger scale). If, however, there exists a dynamic exponent z such that for every L_1 and L_2 it is possible to rescale the time as

$$\frac{t_2}{t_1} = \left(\frac{L_2}{L_1}\right)^z \tag{1}$$

or, in other words, to play the movies at different speeds such that the rate of the evolution is the same on both screens, then we say that in addition to static (spatial) scaling, the system also shows dynamic scaling.

Let us characterize the evolution of a stationary fractal object by "changes" in its pattern, where changes are defined as parts of the space which were not occupied by the object at a certain moment of time but became occupied after some time lag t. Let $n(L, l' > l, t)$ denote the number of changes exceeding size l after some time lag t in a region of size $L \times L$. By definition, changes can only occur in parts of the space occupied by the object. In other words, changes follow the pattern of active channels, and thus, at every scale they are not present in those parts of the space where active channels are not present. Because the object is fractal, with a fractal dimension D, the number of changes scales with the size of the observed region (see appendix) as

$$n(L_2, l' > l, t) = n(L_1, l' > l, t)\left(\frac{L_2}{L_1}\right)^D \tag{2}$$

The presence of dynamic scaling, implying the same rate of evolution after rescaling (equation (1)) is applied, means that the number of changes exceeding sizes l_1 and l_2 after time lags t_1 and t_2 in the regions of size $L_1 \times L_1$ and $L_2 \times L_2$, respectively, is the same on both screens, i.e.,

$$n(L_1, l' > l_1, t_1) = n(L_2, l' > l_2, t_2) \tag{3}$$

provided that the changes are of the same relative size, i.e.,

$$\frac{l_1}{L_1} = \frac{l_2}{L_2} \tag{4}$$

and time and space have been rescaled such that

$$\frac{t_1}{L_1^z} = \frac{t_2}{L_2^z} \tag{5}$$

We stress here that L_1 and L_2 are not the sizes of two different systems but sizes of two different regions of the same system.

Suppose now that we fix the scale of the region of interest to L_2 and that instead of zooming to different scales, we follow the distribution of changes in this region as the object evolves. From (2) and (3) we obtain for the distribution of changes in the region $L_2 \times L_2$

$$n(L_2, l' > l_1, t_1)\left(\frac{L_1}{L_2}\right)^D = n(L_2, l' > l_2, t_2) \tag{6}$$

which is true provided (4) and (5) hold. The variable L_2 is the same in both sides of (6) and therefore can now be dropped. Replacing L_1/L_2 by l_1/l_2 (because of relation (4)) yields

$$l_1^D n(l' > l_1, t_1) = l_2^D n(l' > l_2, t_2) \tag{7}$$

Finally, we obtain the condition for the distribution of changes in a system showing dynamic scaling: there exists a dynamic exponent z such that if (5) is true, i.e., $t/L^z = \text{const}$ (which according to (4) also implies $t/l^z = \text{const}$), then $l^D n(l' > l, t) = \text{const}$, or, in other words, the distribution of changes in such systems can be expressed as

$$n(l' > l, t) = l^{-D} f\left(\frac{t}{l^z}\right) \tag{8}$$

where $f(\ )$ is some function.

To understand the form of that distribution, let us now consider the asymptotic properties of the function $f(t/l^z)$. This function has to level off at big values of the argument t/l^z. Indeed, for big enough time lags, such that the object decorrelates completely between two snapshots, the difference between the two patterns of the object (and therefore the distribution of changes $n(l' > l, t)$) does not depend on time anymore. This implies that $f(t/l^z) = \text{const}$, and, consequently, that $n(l' > l, t) = \text{const} \times l^{-D}$, for big enough values of t/l^z. For time lag $t = 0$, there are no changes in the object, which implies that $n(l' > l, 0) = 0$ and, correspondingly, that $f(0) = 0$. If for small values of the argument the function f can be approximated by a power law, with some exponent β, then the condition (8) for dynamic scaling takes the form

$$n(l' > l, t) \sim t^{\beta} l^{-D-\beta z} \tag{9}$$

It is noted here that the theoretical framework for the description of dynamic scaling of stationary fractal objects as developed above differs from the existing frameworks for dynamic scaling of nonstationary growing objects which has been extensively investigated in the past. For example, dynamic scaling of simulated growing interfaces has been studied by *Edwards and Wilkinson* [1982], *Family* [1986], *Meakin et al.* [1986], *Kardar et al.* [1986], and others [see also *Family and Vicsek*, 1991; *Vicsek*, 1992]. Recently *Czirok et al.* [1993] demonstrated experimentally dynamic scaling in a micromodel of landscape evolution. In these studies the evolution of a fractal surface is described by two exponents α and β corresponding to the spatial and temporal scaling of the surface roughness. In particular, the width or the standard deviation $w(L, t)$ of a surface of linear extent L scales as L^{α} for long times and as t^{β} at the early stages of the process. According to the corresponding dynamic scaling theory, the width follows a double-scaling equation $w(L, t) \sim L^{\alpha} f(t/L^{\alpha/\beta})$ where $f(\ )$ is some function. (The fractal dimension of the rough surface D relates to α as $D = d - \alpha$, where d is the embedding dimension.)

As one can see, the theoretical framework for dynamic scaling of nonstationary growing objects is based on the analysis of the systematic change of a "macroscopic" parameter (width of the surface in the case described above) which essentially describes, in a statistical sense, the nonstationarity of such objects. Obviously, such an approach is not applicable to stationary objects where macroscopic parameters do not change systematically (although they can fluctuate around some average value). Therefore, in the theoretical framework of dynamic scaling of stationary fractal objects developed here we introduced the concept of changes in an evolving stationary object and expressed its dynamic scaling in terms of space-time scale invariance of the probability distribution of these changes. It is believed that the developed framework will be useful for the study of dynamic scaling in natural objects that could not be studied so far under the existing frameworks.

3. Experimental Study of Braided Rivers

One of the reasons that field workers have primarily focused on the detailed study of flow and sediment flux in small areas of braided rivers is the logistical difficulty of studying a complex, continually evolving river system over a large area. The fundamental problems in obtaining data sets characterizing the statistical properties of braided rivers are the high degree of variability in local quantities such as flow depth or sediment flux and the rapidity with which these change with time if the system is active. Thus field data from in situ measurement are difficult to find. Field data can, however, be obtained relatively easily (although tediously) on the static planform morphology of natural braided rivers by determining the presence or absence of water from an air photo or satellite image. For example, the data for the three braided rivers used in the study by *Sapozhnikov and Foufoula-Georgiou* [1996a] were obtained by the tracing of air photos and the digitization of the traced images. Even then, however, care must be taken to insure that data are taken from river sections in which downstream changes in discharge, grain size, vegetation, etc., are minimal so that each reach may be taken as statistically stationary. In the near future it is hoped that improved satellite technology will offer the means of obtaining accurate and frequent monitoring of the spatially and temporally variable flow distribution of natural braided river systems [e.g., see *Smith et al.*, 1995, 1996]. To allow study of the detailed structure of braided rivers, higher resolution satellite images than those available today and wider coverage of areas of interest are needed.

Laboratory models of braided rivers can offer an excellent means of advancing our understanding of the complex dynamics of braided rivers. They offer an environment which permits us to control the physical parameters governing the evolution of the river and to obtain high-resolution images (e.g., see *Schumm et al.* [1987] for an interesting discussion of the advantages of using laboratory experiments in addition to monitoring natural rivers). Braiding is relatively easy to reproduce in the laboratory, and previous studies [*Ashmore*, 1991; *Kuhnle*, 1981; *Leddy et al.*, 1993; *Schumm and Khan*, 1972] have shown that laboratory-scale streams exhibit qualitative features and behavior similar to natural rivers. Quantitative similarity can also be attained but only for gravel bed prototypes [*Ashmore*, 1982, 1985]. Given our emphasis on global statistical properties of braided rivers, both at one instant and as a function of time, experiments provide a useful way of obtaining additional data that can help us to understand the dynamics of braided rivers. The Saint Anthony Falls Laboratory at the University of Minnesota offers an ideal setting for such experiments. In fact, it houses the recently established Experimental Facility for the Study of Large Scale River Morphology and Landscape Evolution funded by NSF's Academic Research Infrastructure Program.

The size of our experimental basin is 5 m × 0.75 m. Sediment and water were supplied continuously at a precisely controlled rate using a constant rate AccuRate auger feeder and a constant height water tank. The sediment and the water were combined together in a mixing funnel before injection into the basin. The grain size of the supplied sediment was 0.12 ± 0.03 mm. The water discharge was 20 g s^{-1}, and sediment supply was 0.6 g s^{-1}. The river was left to evolve until its slope (calculated from the bed elevations measured by point gauge) stabilized at the value of 0.15, which happened 8 days after the initiation of the experiment. The same sediment was used throughout the experiment (i.e., while building up the slope and afterward). The walls of the experimental basin were covered with rough rubber material to reduce the attraction of channels to the walls. To minimize the boundary effects, the data on the river evolution were collected in periods when the river did not touch the walls. Video camera and still cameras recorded the evolution of the system. To visualize the river and monitor its depth, dye was supplied continuously during each videotaping session. For that the sediment supply was switched to another AccuRate auger feeder where the sediment was mixed with the dye powder. This provided the same sediment supply rate as the first feeder, within an accuracy of 5%. After each videotaping session the dye was left to be flushed out of the system and the basin was dye-free in a few hours. We started collecting data 6 days after the slope stabilized, and three videotapes, each covering approximately 40 min of the river evolution in different days, were collected. The studied region was 0.75 m × 1.0 m, starting 3 m downstream from the injection point. The recording time of an image was 1/60 s. The video camera produced images of 240 lines with 1125 points in each line. The recorded data were then digitized for treatment and analysis. The digitized images had 480 × 640 pixels. Therefore the resultant digitized images resolved 240 pixels across the river and 640 pixels along the river. For the studied region size (0.75 m × 1.0 m) this implies a resolution of 3 mm across the river and 1.5 mm along the river. The vertical distance between the camera and the river was 3.1 m. A different angle of observation of the central part and lateral parts of the basin distorts the image (the image of an object in a lateral part of the basin is smaller than the image of an object of the same size in the central part). We measured this distortion and found that it was approximately 2%. The experimental rivers showed a high degree of braiding (e.g., see Figure 1) and active dynamics. Significant changes were recorded in periods of less than 1 min. Here we present the results of analysis of the river evolution recorded in one of the videotapes with the best quality of the image. Similar results were obtained from the analysis of the other two videotapes.

Extracting the river patterns for statistical analysis presented significant difficulties because very soon the sediment was colored with the same dye as the water. However, extracting changes in the river patterns by subtracting images taken at different moments of time proved feasible and quite robust. These changes (depicted as differences in the darkness of the images) are the result of water depth increase or decrease which includes the cases of covering with water a previously dry area or exposing a previously covered area. We used these changes to characterize the evolution of the braided river following the approach developed in section 2. For short enough time lags (such that the colored sediment patterns are almost the same and get zeroed when subtracted) the differences in the two images represent only true changes in the active channel patterns. However, the time lag cannot be made too short (less then approximately 3 s) because in that case the difference between two pictures of the river is small and becomes comparable to the noise introduced by the video camera. At the same time we could not use long time lags (more than approximately 1 min) because in these time lags the patterns of the colored sediment change significantly and subtracting the two images creates spurious (i.e., not caused by the river pattern evolution) changes which erroneously contribute to the probability distribution of changes.

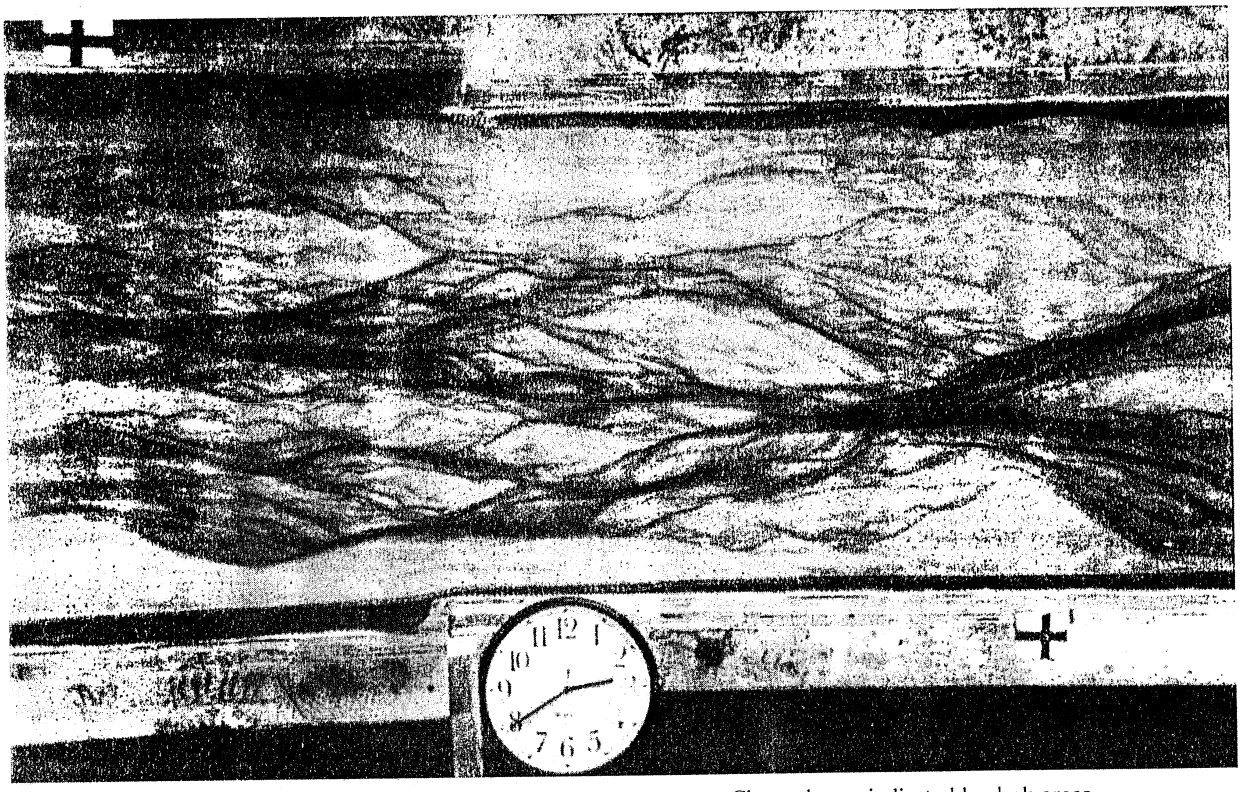

Figure 1. A braided river produced in our laboratory. Channels are indicated by dark areas.

4. Dynamic Scaling in the Experimental Braided River

To study scale relationships in the evolution of braided rivers and test the presence of dynamic scaling, we monitored the changes in our experimental braided river as it evolved and did a statistical analysis of these changes. By monitoring the evolution of the river, we collected 90 frames with a time step of 1 s. The collected patterns were digitized, and, by subtracting these patterns from each other, changes in the braided river were obtained for different time lags (3 s to 1 min). For example, Figure 2a shows a picture of a part of the experimental braided river, and Figure 2b shows the same region 15 s later. Figure 2c displays parts of the basin that were covered with water in Figure 2a but became shallower or exposed in Figure 2b 15 s later ("old" changes). Figure 2d shows parts of the basin that were shallower or not covered with water at all in Figure 2a but became deeper or covered in Figure 2b ("new" changes). Thus, although changes in a river are three-dimensional structures, as is the river itself, in this study we only consider their projections onto a horizontal plane (i.e., when we say "sizes of changes in the river" we imply sizes of their projections). We then apply to the projections the theoretical framework developed in section 2 for two-dimensional objects. In doing that, changes (i.e., parts of the space whose occupancy status switched after some time) are treated equally no matter whether they were located at the elevation of the river bed (e.g., when water conquered dry areas) or higher (e.g., when water level rose in some area). See also section 7 for further discussion of this issue.

It should be noted that dye does not go away immediately from the regions left by active channels, which complicates the observation. Therefore, for quantitative analysis we chose "new" changes (shown in Figure 2d) and not "old" changes (Figure 2c). We made sure (by direct observation of chosen areas) that when colored water conquered a dry area, the area became darker even if its sediment was already colored so we did not miss the new changes. We kept the periods of dye influx short to prevent the sediment from becoming too dark. To eliminate the noise introduced by the video camera, the pixels where the difference between the two subtracted images was very small (less than 24 out of 256 degrees of brightness) were zeroed. Then the cumulative probability distributions of the sizes of changes (characterized by the square root of their areas) were estimated. The distribution of changes was followed over time, and Figure 3 shows these distributions for time lags of 3, 4, 5, 7, 9, and 15 s. Notice that the number of changes of size greater than l in a time lag t, $n(l' > l, t)$, is plotted instead of the probability. As can be seen from Figure 3, these distributions can be well approximated by power laws for different time lags, and the slopes of the log-log plots of the distributions found for different time lags are very close, so they can be viewed as being related by a parallel shift in the log-log scale. In other words, the distributions can be presented in the form

$$n(l' > l, t) = g(t)l^{-k} \tag{10}$$

where $n(l' > l, t)$ is the number of new changes (Figure 2d) of size greater than l for time lag t and $g(t)$ is a function of time lag t.

The log-log plot of $n(l' > l, t)l^k$ against t shown in Figure 4 suggests that for small values of t, $g(t)$ shows a power law dependence

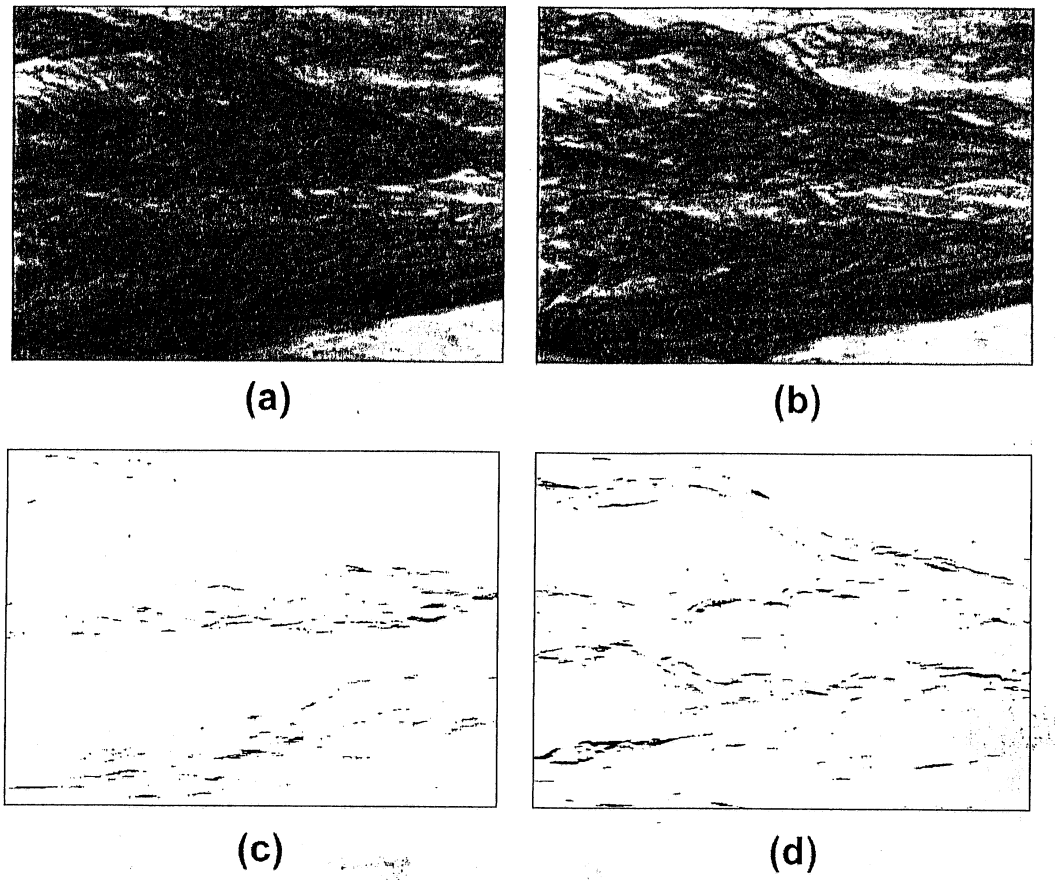

Figure 2. (a) Image of a part of the experimental braided river; (b) the same region 15 s later; (c) parts of the basin that were covered with water in Figure 2a but became shallower or exposed in 15 s (old changes); (d) parts of the basin that were shallower or not covered with water at all in Figure 2a but became deeper or covered in Figure 2b (new changes).

$$g(t) \sim t^{\beta} \tag{11}$$

Equations (10) and (11) can be combined in one equation showing the temporal evolution of the distribution of changes

$$n(l' > l, t) \sim t^{\beta} l^{-k} \tag{12}$$

It is easy to see that this equation coincides with (9) expressing dynamic scaling (for small values of t/l^z) with the dynamic exponent z given as

$$z = (k - D)/\beta \tag{13}$$

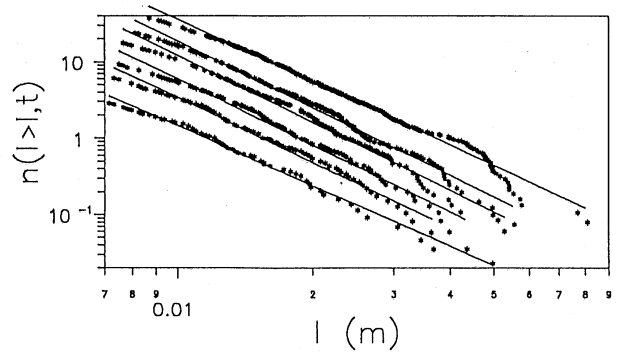

Figure 3. Number of solid areas in Figure 2d (new changes), $n(l' > l, t))$ of size greater than l for time lags t of 3, 4, 5, 7, 9, and 15 s (from bottom to top). The sizes of changes are measured as the square root of their areas. The plot suggests that the distributions have broad central regions that are well approximated by power laws, and their slopes for different time lags are very close.

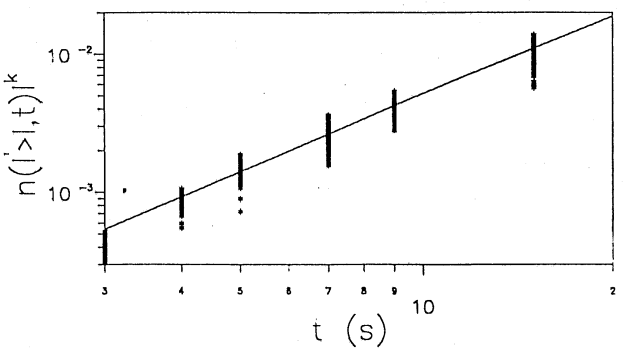

Figure 4. Evolution of the distribution of changes shown by the time dependence of the function $n(l' > l, t)l^k$. The plot suggests that power law dependence applies well over a major part of the range.

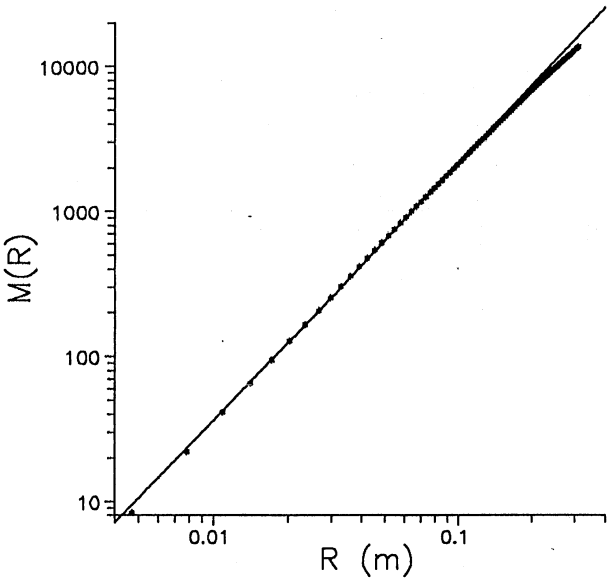

Figure 5. Spatial scaling in the experimental braided river indicated by straight line log-log dependence of its mass M (the number of pixels covered with water) within a square box versus the size of box R. The estimated value of D is 1.75.

Equations (1) and (8), in general, and (1), (12), and (13), in particular (the power law dependence (equation (12)) being suggested by the braided river data for small values of t/l^z), integrate spatial and temporal scaling characteristics under the unifying framework of dynamic scaling.

In principle, the parameter z (dynamic exponent) can be estimated directly from (8). That is, by nonlinear optimization the value of z that minimizes the spread of the points $n(l' > l, t)l^D$ versus t/l^z (so that all curves collapse to a single curve f) can be found. However, we preferred to take advantage of the power law dependence (equation (12)) suggested by the data and to follow a stepwise estimation approach. Namely, we use the power law distribution of changes (Figure 3 and equation (10)) to estimate k and the power law dependence of $g(t)$ (Figure 4 and equation (11)) to estimate β. Then z is estimated from (13). Specifically, from the slopes of the plots shown in Figures 3 and 4 the exponent k in (10) was estimated as 2.8 and the exponent β in (11) was estimated as 2.0. The fractal dimension of the experimental braided river D was estimated from one pattern of the river by the "mass-in-a-box" method [e.g., see *Mandelbrot*, 1982] as 1.75 (see Figure 5). These estimates gave an estimate of the dynamic scaling exponent from (13) as $z \simeq 0.5$.

It is important to note that although for small time lags Figure 3 shows reasonably good temporal scaling, it deviates from the power law behavior for bigger time lags. It should be stressed, however, that this does not indicate the loss of dynamic scaling (expressed by the general equation for dynamic scaling (8)). Indeed, as discussed in section 2, even if the function f, from (8), follows a power law at small values of the argument, it has to level off at big values of the argument which necessarily leads to the loss of power law dependence in relation (11) but not to the loss of dynamic scaling. In fact, to confirm that the distributions corresponding to different time lags satisfy the general equation for dynamic scaling (8), we plotted for $z = 0.5$ the values of $n(l' > l, t)l^D$ versus t/l^z for different time lags up to 1 min in Figure 6. As one can see, all curves satisfactorily collapse to a single curve (the $f(t/l^z)$ function). This further corroborates the presence of dynamic scaling and the adequacy of the estimated dynamic exponent $z \simeq 0.5$ in the experimental braided river. Notice that this last confirmation of dynamic scaling, i.e., that the general equation for dynamic scaling (equation (8)) holds, did not directly use the assumption of power law distribution of changes (equation (10)) or power law dependence of $g(t)$ for small values of t (equation (11)). These two special forms of dependencies (suggested directly from the experimental data in Figures 3 and 4) were conveniently used only to estimate z in a stepwise manner via (13). After the value of z was estimated, plotting $n(l' > l, t)l^D$ versus t/l^z and seeing that all curves collapse to a single curve provides additional and independent evidence of dynamic scaling.

We would like to point out that on the basis of the study of *Sapozhnikov and Foufoula-Georgiou* [1996a], the experimental braided river is expected to be a self-affine object (characterized by two scaling exponents ν_x and ν_y) and not a self-similar object (characterized by a single fractal dimension D). Despite this, the above developments of dynamic scaling were presented in terms of a single fractal dimension D. This is because, as discussed also later in section 7, extension of the dynamic scaling theory to self-affine objects has not yet been achieved and should form the focus of further research. Moreover, it is noted that even if that theory were available at present, our experimental data did not even permit an estimation of ν_x and ν_y for two main reasons: (1) the river segment was too short to get an accurate estimate via the LCI method, and (2) it was hard to separate the river from the colored sediment in the video images in order to produce reliable tracings of the river pattern. Note that this was not a problem for changes in the river pattern because the colored sediment was zeroed by subtraction. Despite the above limitations, we note that the presented dynamic scaling developments are still valid for a self-affine object, and D can be seen as a surrogate parameter for D_G (global fractal dimension) of the braided river which relates to ν_x and ν_y via the expression given by *Sapozhnikov and Foufoula-Georgiou* [1995]: $D_G = (\nu_y - \nu_x + 1)/\nu_y$. Of course, further refinement of the developed framework to self-affine objects characterized by ν_x and ν_y is desirable, but this is an issue for further study.

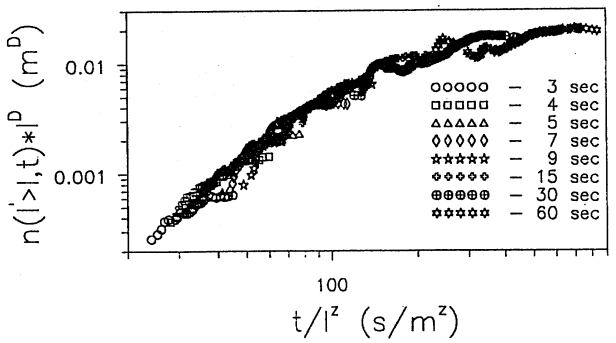

Figure 6. Plot showing that the rescaled distributions of changes collapse into a single curve (equation (8)). Time lags from 3 to 60 s (bottom left to top right) are shown. This further corroborates the presence of dynamic scaling and the adequacy of the estimated value of the dynamic exponent as $z \simeq 0.5$ for the experimental braided river.

5. Physical Interpretation of Dynamic Scaling

In any natural phenomenon, large-scale statistical symmetries or scale invariances, if found present, are believed and hoped to be related to the physical mechanisms that created the space-time structure of the process at hand, although establishing and understanding these relations very often turns out to be a nontrivial task. So what does the value of the dynamic exponent indicate for the physical mechanisms of a braided river? First, on the basis of (1) the estimated value of the dynamic exponent $z \simeq 0.5$ implies that if one increases the spatial scale by, say, 10 times, the evolution of the system slows down by $10^{0.5} \simeq 3$ times. In other words, for instance, it implies that the lifetime of the channels in a braided river system scales with channel size such that 10 times smaller channels disappear approximately 3 times faster. Furthermore, the low value of the dynamic exponent $z \simeq 0.5 \ll 2$ indicates a relatively weak dependence of the rate of evolution on the spatial scale. This provides insight into the physical processes governing the evolution of braided rivers. Indeed, this value of z is significantly lower than the typical values of the dynamic exponent, which are usually 2 or higher [e.g., see *Ma*, 1976]. For example, as a simple case, if the lifetime of a channel were controlled by a diffusion-type process, it would be proportional to the square of the scale, which would imply that $z = 2$. On the other hand, if we hypothetically imagine as a limiting case that the small channels do not evolve by themselves at all and only appear or disappear because (and when) the bigger channels feeding them appear or disappear, then the lifetime of smaller and bigger channels would be the same, which would mean that no temporal rescaling is required when going from one spatial scale to another. This would imply that $z = 0$. Thus the small value of z obtained for braided rivers indicates strong correlation between the evolution of large and small channels within a braided river system. This leads to the conjecture that the evolution of small channel patterns is to a great extent forced by the evolution of larger channels. Notice that further support for this conjecture is provided by the fact that the other way around, i.e., changes in small channels forcing changes in large channels, would require a spontaneous synchronization in evolution of small channels which feed a larger one, and this does not seem feasible. Indeed, for a larger channel to disappear as a result of the disappearance of the smaller channels feeding it, smaller channels would have to disappear at the same time. At this point we do not see a mechanism for such a synchronization.

6. Are Braided Rivers Self-Organized Critical Systems?

The self-organized criticality (SOC) concept introduced by *Bak et al.* [1987] states that many nonlinear systems with extended degrees of freedom self-organize into a critical state in a natural way, i.e., without any tuning parameter (e.g., temperature) which is needed to bring traditional equilibrium systems to a critical state [see, e.g., *Ma*, 1976; *Patashinskii and Pokrovskii*, 1979]. The concept of SOC has been found useful in many scientific and engineering applications, for example, earthquake prediction, snow avalanche prediction, description of solar flares, description of forest fires, etc. [see *Bak and Paczuski*, 1993]. In the past few years the SOC concept has been explored for drainage network landscape evolution [e.g., *Takayasu and Inaoka*, 1992; *Rinaldo et al.*, 1993] and, recently, has been claimed by *Stølum* [1996] for dynamics in the fluid mechanical model of a meandering river developed by G. Parker, A. E. Howard and coworkers [e.g., see *Parker and Andrews*, 1986; *Howard and Knutson*, 1984].

In a recent publication, *Sapozhnikov and Foufoula-Georgiou* [1996b] have questioned the applicability of the SOC concept to models of erosional landscape evolution. They have argued that none of the states of these modeled landscapes can be considered critical and that the resulting landscapes show scaling in space characterized by fractal geometry but not scaling in time as they do not allow any changes under perturbations let alone "catastrophic" changes possible for a system in a critical state. However, we believe that braided rivers are systems where the SOC concept naturally applies. Braided rivers (1) are nonlinear systems, (2) obviously have an enormous number of degrees of freedom, (3) show collective behavior which is a crucial feature of systems in a critical state, (4) exhibit spatial scaling [see *Sapozhnikov and Foufoula-Georgiou*, 1996a], and (5) undergo significant changes over a wide range of scales even when they are statistically in equilibrium. Moreover, evidence was presented in this study for the presence of dynamic scaling as well, which is an important characteristic of systems at the critical state. It should be noted that the experimental braided river system brought itself to the state at which it showed dynamic scaling by just being uniformly supplied with water and sediment, i.e., without tuning any physical parameter of the experimental model. It happened in the same way as in the sandpile model [*Bak*, 1987], where the system builds up itself without any tuning and shows spatial and temporal scaling. For all of the above reasons we conjecture that braided rivers may be self-organized critical systems.

Studying braided river dynamics under the SOC framework offers the potential of using the apparatus of the theory of critical state which provides a general framework for description and understanding of all critical phenomena and enables one to apply results obtained for known systems (e.g., magnetic fields and percolation clusters) to new systems less well known. An example of this idea is presented by *Tang and Bak* [1988]. Strictly speaking, to firmly establish SOC, one would also need to follow the behavior of the braided river as it approaches the critical state (perhaps with the critical slope playing the role of critical temperature here). Such experiments, however, are very hard to perform (even in other more controlled physical systems), and thus spatial and dynamic scaling of the type presented here is usually considered adequate evidence for SOC. Nevertheless, more data analysis of the braided river before, as it approaches stationarity, and after its slope stabilizes, is needed to firmly establish whether and under what conditions braided rivers can be considered self-organized critical systems.

7. Conclusions and Open Problems

In a previous study, *Sapozhnikov and Foufoula-Georgiou* [1996a] presented evidence that braided rivers exhibit spatial (static) scaling in their morphology. In this study we presented evidence that braided rivers exhibit dynamic scaling too, which implies that it is possible to renormalize space and time such that a smaller part of a braided river evolves identically (in a statistical sense) to a larger part of the river. The presence of dynamic scaling is not only interesting in its own right but also promises to shed light upon the space-time dynamics of braided rivers by unraveling statistical similarities between pat-

terns at smaller space-time scales and those at larger space-time scales. The dynamic scaling relationships established here can also be used to statistically predict long-term changes of the system at a larger spatial scale on the basis of monitored short-term changes at a smaller spatial scale. The evidence for dynamic scaling was further interpreted as an indication that braided rivers may be in a critical state and behave as self-organized critical systems. From experimental braided river data produced in our laboratory the value of the dynamic exponent z for the space-time rescaling in (1) was established to be approximately equal to 0.5. This value of z was interpreted as an indication of a relatively weak dependence of the rate of evolution on the spatial scale in braided rivers. In particular, it lead us to conjecture that changes in small channel patterns are to a great extent forced by the changes in larger channels.

Our analysis presents a first attempt to study the large-scale dynamics of braided rivers and to seek spatiotemporal invariances in those systems. Of course, more theoretical, empirical, and experimental research is needed to fully study the space-time evolution of these complex systems and their scale relations. Some open problems follow.

In our analysis the evolution of the braided river system has been characterized by the horizontal sizes of changes. An interesting direction for further research is the introduction of the third dimension, i.e., consideration of the depth of changes in addition to their horizontal sizes. This approach would enable one to explore braided rivers for "dynamic multiscaling."

In our study we analyzed changes in the river by subtracting two images of the river taken at different moments of time. In doing that we did not distinguish between changes caused (1) by the flooding of previously dry areas of the basin and (2) by the increase of water depth in areas which were already covered with water. This separation was not feasible with our data because sediment coloring did not allow us to determine with certainty from the darkness of the image whether a particular location was or was not covered with water. A more detailed analysis which would include separation of these two cases may be of interest, but this would require a different technology than sediment coloring which would permit accurate determination of water depth (and not water depth change only) at every point of the basin. Such data would permit study of the space-time structure of water depth too and thus characterization of the hydrology in addition to the morphology of braided rivers.

Also, an important issue for future study should be the extension of the developed theoretical framework of dynamic scaling to self-affine objects. That is, if the underlying object is self-affine and is characterized by two fractal exponents ν_x and ν_y, expressions of dynamic scaling should be developed in terms of ν_x and ν_y (or in terms of the two fractal dimensions D_G and D_L) (see *Sapozhnikov and Foufoula-Georgiou* [1995, 1996a] for the connection of ν_x and ν_y to D_G and D_L). An associated open problem is the theoretical description of the critical state of self-affine objects. Such a theory does not exist to our knowledge, probably because there was no need for it in traditional (not self-organized) critical systems. Another important issue to be explored is the connection of dynamic scaling not only to the fractal geometry of braided rivers but also to other scaling characteristics of natural and simulated braided rivers, such as power law distributions in channel widths and bar sizes [e.g., see *Howard et al.*, 1970; *Barzini and Ball*, 1993; *Murray and Paola*, 1994; *Sapozhnikov and Foufoula-Georgiou*, 1996a].

It should be stressed that our analysis applies to the comparison of small and large parts of one river system and not of one system with another. The latter would require inclusion of other physical parameters which govern the evolution of rivers. For example, slope plays a crucial role in the rate of the evolution of rivers (the greater the slope, the faster the evolution). For example, the slope of Brahmaputra is 2000 times lower than that of our experimental river, which significantly affects their relative rates of evolution. Other important factors are total water and sediment flux in a river (the greater the imposed flux, the faster the evolution) [*Ashmore*, 1985] and the type of the sediment. Thus, to relate the rate of the evolution of different systems, (1) has to be extended. Under a scaling hypothesis one could conjecture that it would take the form

$$\frac{t_2}{t_1} = \left(\frac{L_2}{L_1}\right)^z \left(\frac{s_2}{s_1}\right)^\gamma \cdots \tag{14}$$

where s is the slope of a river and the dots imply that other parameters could enter this equation in a power law multiplicative way. Toward establishing the precise form of (14), study through laboratory experiments of the effect of the sedimentological and hydrological characteristics (slope, input water and sediment discharge, and grain size) on the evolution and scaling exponents of braided rivers is needed, and this is an important issue for future research. Such studies will permit transferability of results from one system to another and from laboratory to nature.

8. Appendix: Scaling of the Number of Changes in a Fractal Object With the Size of the Observed Region

Here we will illustrate by example that the number of changes scales with the size of the observed region as written in (2). Consider, for example, a 3×3 Sierpinsky carpet with one square taken out (black area) such that every bigger square contains eight smaller ones and is a replication of the smaller squares at a larger scale (see Figure 7). The fractal dimension of this Sierpinsky carpet is $D = \log 8/\log 3$. Let us allow evolution of this carpet. The details of the evolution rules are not important for our purpose as long as the fractal dimension of the carpet is preserved. Similarly to what we did for braided rivers, we define changes in the evolving Sierpinsky carpet as parts of the space which were not occupied by the carpet at a certain moment of time but became occupied after some time lag. Since by definition the changes can only occur in the parts of the space occupied by the object (i.e., in the eight white squares), the cumulative number of changes in the 3 times larger square is 8 times the number of changes in a smaller square: $n_{\text{larger}}/n_{\text{smaller}} = (L_{\text{larger}}/L_{\text{smaller}})^D = 8$. In other words, the cumulative number of changes scales with the size of the observed region, with the scaling exponent equal to the fractal dimension of the generating fractal object. To avoid confusion, it should be noted that fractality of the spatial pattern of changes is not needed for the cumulative number of changes to scale as written in (2). For example, in the Sierpinsky carpet the cumulative number of islands (black parts) of a given size scales with the size of observation, with an exponent D (it increases $3^D = 8$ times when the scale is increased 3 times). However, the spatial pattern of the islands is not a fractal object at all (it has a nonzero Lebesgue measure).

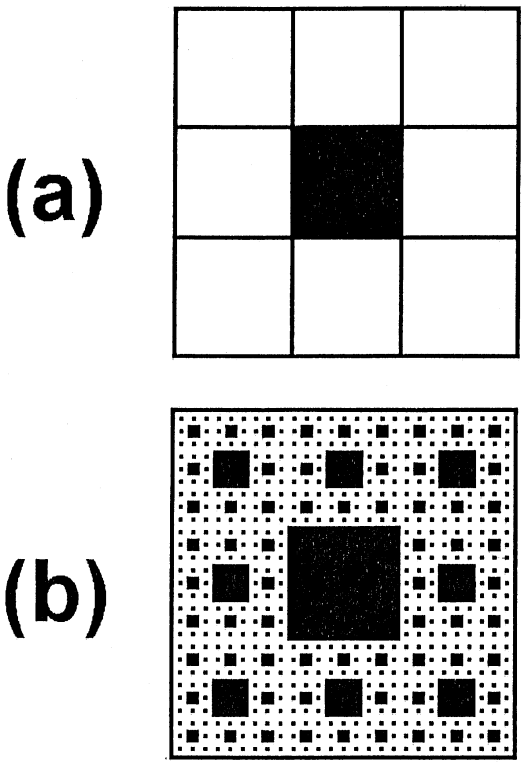

Figure 7. (a) The generator of a 3 × 3 Sierpinsky carpet with one square taken out (solid area) and (b) the Sierpinsky carpet.

Acknowledgments. This research was partially supported by NSF grant EAR-9628393. Supercomputer resources were kindly provided by the Minnesota Supercomputer Institute. We would like to thank Chris Paola, Gary Parker, and Alin Carsteanu for very helpful discussions, A. Brad Murray for tracing the image of the experimental braided river, and David Mohrig and Ben Erickson for help with the experimental equipment and setup. We would also like to thank the three anonymous reviewers for their helpful comments which resulted in an improved presentation of our developments.

References

Ashmore, P. E., Laboratory modelling of gravel braided stream morphology, *Earth Surf. Processes Landforms*, *7*, 201–225, 1982.

Ashmore, P. E., Process and form in gravel braided streams: Laboratory modelling and field observations, Ph. D. thesis, Univ. of Alberta, Edmonton, Alberta, Canada, 1985.

Ashmore, P. E., How do gravel-bed rivers braid?, *Can. J. Earth Sci.*, *28*, 326–341, 1991.

Bak, P., and M. Paczuski, Why nature is complex, *Phys. World*, *12*, 39–43, 1993.

Bak, P., C. Tang, and K. Wiesenfeld, Self-organized criticality: An explanation of 1/*f* noise, *Phys. Rev. Lett.*, *59*, 381–384, 1987.

Barzini, G. N., and R. C. Ball, Landscape evolution in flood—a mathematical model, *J. Phys. A Math Gen.*, *26*, 6777–6787, 1993.

Czirok, A., E. Somfai, and T. Vicsek, Experimental evidence for self-affine roughening in a micromodel of geomorphological evolution, *Phys. Rev. Lett.*, *71*, 2154–2157, 1993.

Edwards, S., and D. Wilkinson, The surface statistics of a granular aggregate, *Proc. R. Soc. London A*, *381*, 17–31, 1982.

Family, F., Scaling of rough surfaces: Effect of surface diffusion, *J. Phys. A Math Gen.*, *19*, L441–L446, 1986.

Family, F., and T. Vicsek (Eds.), *Dynamics of Fractal Surfaces*, World Sci., River Edge, N. J., 1991.

Howard, A. E., and T. R. Knutson, Sufficient conditions for river meandering: A simulation approach, *Water Resour. Res.*, *20*, 1659–1667, 1984.

Howard, A. D., M. E. Keetch, and C. L. Vincent, Topological and geometrical properties of braided streams, *Water Resour. Res.*, *6*, 1674–1688, 1970.

Kadanoff, L. P., S. R. Nagel, L. Wu, and S. Zhou, Scaling and universality in avalanches, *Phys. Rev. A*, *39*, 6524–6537, 1989.

Kardar, M., G. Parisi, and Y. Zhang, Dynamic scaling of growing interfaces, *Phys. Rev. Lett.*, *56*, 889–892, 1986.

Kuhnle, R. A., An experimental study of braiding in gravel-bed streams, M.S. thesis, Univ. of Illinois, Chicago, 1981.

Leddy, J. O., P. J. Ashworth, and J. L. Best, Mechanisms of anabranch avulsion within gravel-bed braided rivers: Observations from a scaled physical model, in *Braided Rivers*, edited by J. L. Best and C. S. Bristow, pp. 119–127, Geol. Soc. of London, London, England, 1993.

Ma, S. K., *Modern Theory of Critical Phenomena*, Benjamin, White Plains, N. Y., 1976.

Mandelbrot, B., *The Fractal Geometry of Nature*, 468 pp., W. H. Freeman, New York, 1982.

Meakin, P., P. Ramanlal, L. Sander, and R. Ball, Ballistic deposition on surfaces, *Phys. Rev. A*, *34*, 5091–5103, 1986.

Murray, A. B., and C. Paola, A cellular automata model of braided rivers, *Nature*, *371*, 54–57, 1994.

Parker, G., and E. D. Andrews, On the time development of meander bends, *J. Fluid Mech.*, *162*, 139–156, 1986.

Patashinskii, A. Z., and V. L. Pokrovskii, *Fluctuation Theory of Phase Transitions*, 321 pp., Pergamon, Tarrytown, N. Y., 1979.

Rinaldo, A., I. Rodriguez-Iturbe, R. Rigon, E. Ijjasz-Vasquez, and R. L. Bras, Self-organized fractal river networks, *Phys. Rev. Lett.*, *70*, 822–825, 1993.

Sapozhnikov, V. B., and E. Foufoula-Georgiou, Study of self-similar and self-affine objects using logarithmic correlation integral, *J. Phys. A Math Gen.*, *28*, 559–571, 1995.

Sapozhnikov, V. B., and E. Foufoula-Georgiou, Self-affinity in braided rivers, *Water Resour. Res.*, *32*, 1429–1439, 1996a.

Sapozhnikov, V. B., and E. Foufoula-Georgiou, Do the current landscape evolution models show self-organized criticality?, *Water Resour. Res.*, *32*, 1109–1112, 1996b.

Schumm, S. A., and H. R. Khan, Experimental study of channel patterns, *Geol. Soc. Am. Bull.*, *83*, 1755–1770, 1972.

Schumm, S. A., M. P. Mosley, and W. E. Weaver, *Experimental Fluvial Geomorphology*, chap. 1, pp. 1–7, Wiley-Interscience, New York, 1987.

Smith, L. C., B. L. Isacks, R. R. Forster, A. L. Bloom, and I. Preuss, Estimation of discharge from braided glacial rivers using ERS 1 synthetic aperture radar: First results, *Water Resour. Res.*, *31*, 1325–1329, 1995.

Smith, L. C., B. L. Isacks, A. L. Bloom, and A. B. Murray, Estimation of discharge from three braided rivers using synthetic aperture radar satellite imagery: Potential application to ungaged basins, *Water Resour. Res.*, *32*, 2031–2034, 1996.

Stølum, H. H., River meandering as a self-organization process, *Nature*, *271*, 1710–1713, 1996.

Takayasu, H., and H. Inaoka, New type of self-organized criticality in a model of erosion, *Phys. Rev. Lett.*, *68*, 966–969, 1992.

Tang, C., and P. Bak, Critical exponents and scaling relations for self-organized critical phenomena, *Phys. Rev. Lett.*, *60*, 2347–2350, 1988.

Vicsek, T., *Fractal Growth Phenomena*, World Sci., River Edge, N. J., 1992.

E. Foufoula-Georgiou and V. B. Sapozhnikov, Saint Anthony Falls Laboratory, University of Minnesota, Mississippi River and 3rd Avenue SE, Minneapolis, MN 55414. (e-mail: efi@mykonos.safhl.umn.edu)

(Received October 31, 1996; revised February 2, 1997; accepted April 23, 1997.)

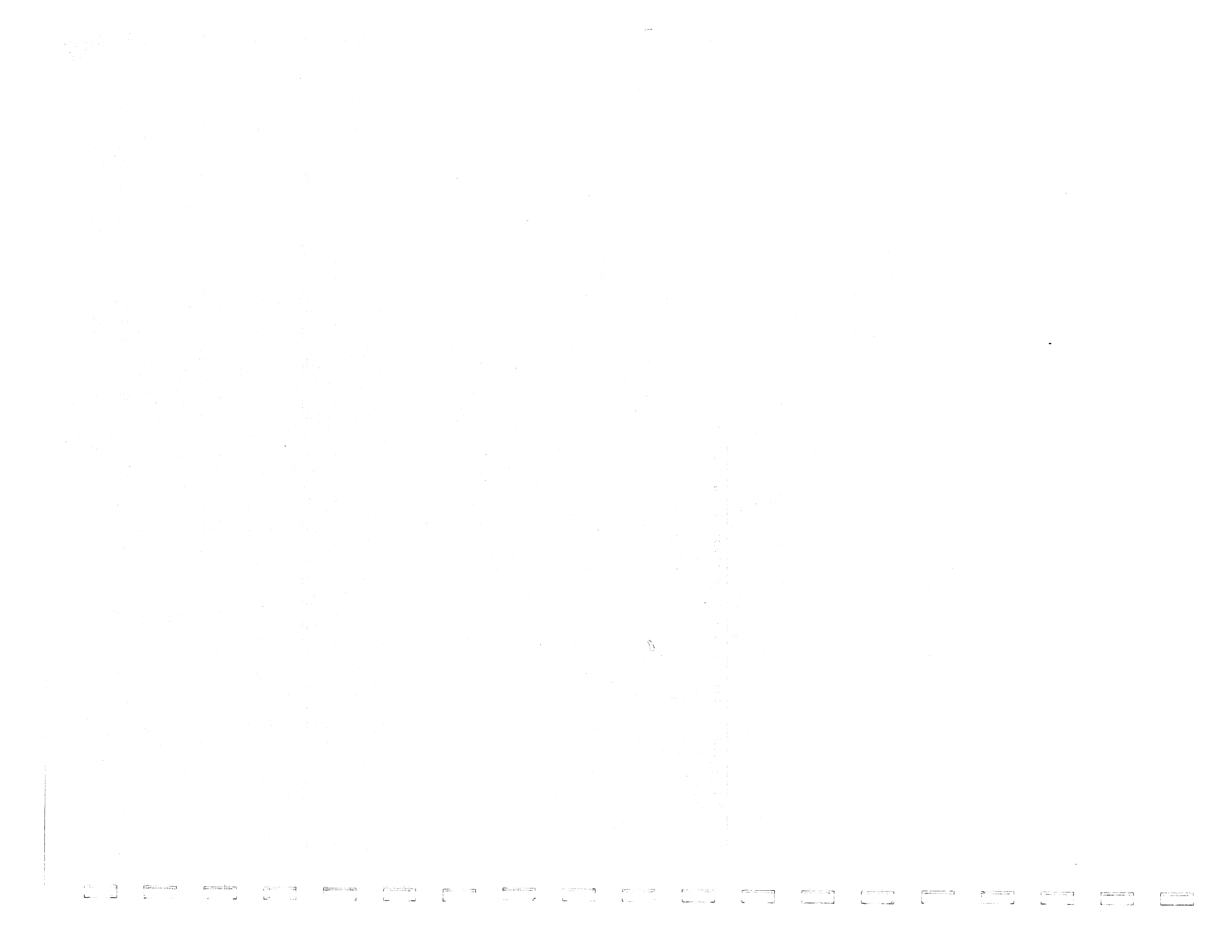

WATER RESOURCES RESEARCH, VOL. 32, NO. 5, PAGES 1429–1439, MAY 1996

St. Anthony Falls Laboratory
Technical Paper 455 - Series A

Self-affinity in braided rivers

Victor Sapozhnikov and Efi Foufoula-Georgiou
St. Anthony Falls Laboratory, University of Minnesota, Minneapolis

Abstract. Three braided rivers of different scales and different hydrologic/geomorphologic characteristics (the Aichilik and Hulahula in Alaska and the Brahmaputra in Bangladesh) are analyzed for spatial scaling using a logarithmic correlation integral method developed earlier by the authors. It is shown that the rivers exhibit anisotropic scaling (self-affinity) with fractal exponents $\nu_x = 0.72$–0.74 and $\nu_y = 0.51$–0.52, the x axis being oriented along the river and the y axis in the perpendicular direction. The fact that despite large differences in scales (0.5–15 km in braid plain width), slopes (7×10^{-3} to 8×10^{-5}), and types of bed material (gravel to sand), the analyzed braided rivers show similar spatial scaling deserves special attention. It might indicate the presence of universal features in the underlying mechanisms responsible for the formation of the spatial structure of braided rivers. Also, comparison of fractal characteristics of braided rivers with those of single-channel rivers and river networks suggests that braided rivers form a class of fractal objects lying between the classes of single-channel rivers and river networks.

1. Introduction

Braided rivers, i.e., rivers "having a number of alluvial channels with bars and islands between meeting and dividing again" [*Lane*, 1957], form a separate class of hydrologic systems, other than single-channel rivers and river networks. They prevail in mountainous and glacial regions and are highly dynamic systems characterized by intensive erosion, sediment transport and deposition, and frequent channel shifting. Study of the morphology of the braided rivers and processes governing their behavior is important in geomorphology, geology, hydrology, and environmental studies. The alluvial deposits of braided rivers are important reservoirs of water, oil, gas, coal, sand, gravel, and heavy minerals. Despite their importance, braided rivers have not been studied as extensively as single-channel rivers and river networks (see, for example, *Bristow and Best* [1993]). In particular, there is a significant lack of quantitative studies in braided rivers; the existing models and frameworks are mostly qualitative. With the exception of the early work by *Howard et al.* [1970] it is only recently that some more quantitative studies were carried out, such as, for example, that of *Murray and Paola* [1994, 1996], *Murray* [1995], and *Webb* [1995].

Braided rivers exist over a large range of scales from several meters to 20 km in width. It is clear that when applying results from one braided river to another of different size, or from a physical model to a real braided river, the issue of scale and its effect on the geometry, runoff, and forming processes of the river inevitably arises. Scale relationships are also important in understanding the internal structure of a particular braided river. Indeed, the processes shaping a braided river and causing branching, confluence and bar growth, and erosion act over a wide range of scales and produce an internal structure which also manifests itself over a large range of scales. Exploring scale relations in the internal structure of braided rivers can help to understand better the processes responsible for sculpturing the river. To address these questions, quantitative tools for the description of the geometric and hydrologic characteristics of braided rivers are needed.

Paper number 96WR00490.
0043-1397/96/96WR-00490$09.00

In braided rivers, sinuosity of individual channels and their branching and confluence produces a rather complex and hierarchical spatial structure which needs appropriate tools for its description. Often, such complex structures find their natural description in terms of self-similar or self-affine fractals [*Mandelbrot*, 1982]. At first glance the spatial structure of the whole braided river and its structure at the level of channels appear to have some kind of similarity [see *Bristow and Best*, 1993]. This impression, however, needs to be either validated or disproved by quantitative analysis.

The presence of scaling in a phenomenon means that statistical properties of the phenomenon at one scale relate to its statistical properties at another scale via a transformation which involves only the ratio of the two scales. This implies a certain invariance of the phenomenon under magnification or contraction (scale invariance). Objects showing the same spatial scaling in all directions (which makes it impossible to determine the scale of the object from its photograph) are called self-similar fractals and can be characterized by their fractal dimension D. In a more general case, scaling properties are different in different directions. Such anisotropically scaled objects are called self-affine fractals and are characterized by more than one fractal exponents which properly reflect scaling in each direction. In terms of fractal dimension a self-affine fractal is characterized not by one but rather by two fractal dimensions: the local fractal dimension D_L and the global fractal dimension D_G [*Mandelbrot*, 1986].

Spatial scaling has been established for single-channel rivers and river networks [see *Tarboton et al.*, 1988; *La Barbera and Rosso*, 1989; *Nikora*, 1991; *Sapozhnikov and Nikora*, 1993; *Peckham*, 1995]. Moreover, it was shown that the fractal geometry of river networks is closely connected to other hydrologic characteristics, such as distribution of discharge masses and of energy dissipation in river basins [e.g., *Rodriguez-Iturbe et al.*, 1992]. *Nikora et al.* [1993] demonstrated that natural and simulated individual streams show a complicated geometry:

self-similarity at small scales and self-affinity at larger scales. Self-affine behavior of the streams is caused by gravity which makes the streams scale differently in the direction of the mainstream slope and in the perpendicular direction. Self-affinity in natural river courses was also reported by *Ijjasz-Vasquez et al.* [1994]. Anisotropic spatial scaling ("external scaling," see section 2) was revealed in simulated river networks [e.g., *Kondoh et al.*, 1987; *Meakin et al.*, 1991]. *Nikora and Sapozhnikov* [1993] found that both natural and simulated river networks show isotropic scaling at small scales and anisotropic scaling at larger scales.

In contrast to a great number of papers existing on fractal properties of rivers and river networks the scaling in braided rivers has virtually not been studied. We are aware only of one study by *Nikora et al.* [1995], who analyzed several sections of New Zealand rivers as self-similar objects and reported fractal dimension $D = 1.5$–1.7. However, the presence of gravity which causes the scaling anisotropy in individual streams and river networks provides reasons to expect self-affine geometry in the braided streams too. The problem is that until recently no method existed for analyzing scaling anisotropy (self-affinity) except for the special case of a nonbranched line [see *Matsushita and Ouchi*, 1989; *Nikora et al.*, 1993] or of an object having a distinct hierarchical structure (e.g., one can easily find fractal exponents for a self-affine Sierpinsky carpet; see also *Nikora and Sapozhnikov* [1993] and *Nikora* [1994], who used scaling of subbasins to estimate fractal exponents of river networks).

It was only recently that a method was developed by the authors to study self-affinity in objects having any topology [*Sapozhnikov and Foufoula-Georgiou*, 1995]. The method is applied in this paper to study the self-affine characteristics of three braided rivers (Brahmaputra in Bangladesh and Aichilik and Hulahula in Alaska). It is found that these rivers exhibit self-affine scaling, the fractal exponents being $\nu_x = 0.72$–0.74 and $\nu_y = 0.51$–0.52. The fact that the fractal exponents ν_x and ν_y are practically the same for all three rivers is worth noticing given that these rivers exist over disparate spatial scales (from 0.5 to 15 km in braid plain widths and from 6.4 to 200 km in length of analyzed sections) and have different slopes (7×10^{-3} to 8×10^{-5}) and different types of bed material (gravel to sand).

This paper is structured as follows. In section 2 the difference between "internal" and "external" fractal exponents is discussed. It is emphasized that the internal fractal exponents (ν_x and ν_y) characterize the internal self-affine structure of a braided river; that is, they show how parts of the whole object scale with respect to each other. These exponents should not be confused with the external self-affine exponents (α_x and α_y) which show how the whole object scales with respect to other (whole) objects and which could be obtained by analyzing a large number of rivers as realizations of an ensemble. Section 3 presents a method for estimating the internal self-affine fractal exponents of an object of any geometry. More details of this method are given by *Sapozhnikov and Foufoula-Georgiou* [1995]. In section 4 the results of the application of this method to three braided rivers are presented. In section 5 we study robustness of the proposed method in estimating the fractal exponents of natural rivers. In section 6, scaling in the sizes of islands in the three studied rivers is analyzed and compared with the results obtained in section 4. Concluding remarks are given in section 7.

2. Internal Versus External Self-Affine Scaling

Each part of a self-affine object is an image of the whole object (either strictly or in a statistical sense) scaled differently in different directions. In other words, if we take a part of the object within a $X \times Y$ rectangle and then change X and Y in a certain different way, we will get the same pattern. This finds its mathematical expression in the relationship

$$M(X, Y) \sim X^{1/\nu_x} \sim Y^{1/\nu_y} \tag{1}$$

where $M(X, Y)$ is the mass of the object within the rectangle of size $X \times Y$ and ν_x and ν_y are the fractal exponents. In the case of self-similarity this equation takes the form

$$M(R) \sim R^D, \tag{2}$$

where $R = X = Y$ is the length of the square side.

While there are several methods for determination of the fractal dimension of self-similar objects, methods for determination of the fractal exponents characterizing self-affine objects seem to be much less developed. The fractal dimension of a self-similar object can be easily estimated from a pattern of the object. However, in a general case, one cannot find the fractal exponents ν_x and ν_y from a pattern of a self-affine object. The problem is that the mass M scales only if the sides of the rectangle change in a certain different way, and in contrast to the self-similar case we do not know a priori how to change X and Y because we do not know the ratio ν_x/ν_y. We can only state that the mass within the rectangle scales provided $X^{1/\nu_x} \sim Y^{1/\nu_y}$.

The methods available for studying a general self-affine object do not analyze the geometry of the object but rather follow how the mass M_0 of the total object changes as the sides X_0 and Y_0 of the object change. If one has available either an ensemble of the same type of objects of different size or patterns of the object at different stages of growth, the ensemble or the evolution of the object can be characterized by exponents α_x and α_y using the relationship

$$M_0(X_0, Y_0) \sim X_0^{1/\alpha_x} \sim Y_0^{1/\alpha_y} \tag{3}$$

We will call α_x and α_y external exponents, in contrast to the internal exponents ν_x and ν_y that characterize the geometry of the object. Since methods for extracting the internal exponents from a pattern of the object are not available in a general case, external exponents instead of internal ones have often been used to describe the geometry of the object [e.g., *Kondoh et al.*, 1987; *Meakin et al.*, 1991]. However, this approach supposes that internal and external exponents are equivalent. *Sapozhnikov and Foufoula-Georgiou* [1995] demonstrated that this supposition is, generally speaking, wrong. To get an idea of the difference between internal and external exponents, let us consider here two examples.

1. Let us consider a trajectory of a biased random walk, such that every jump has a projection on the x axis equal to 1 and a projection on the y axis equal to 1 or -1 with equal probability (e.g., one can think of this trajectory as a simplified representation of a river). This trajectory is known to be a self-affine fractal [e.g., *Mandelbrot*, 1982, p. 350]. Its geometry is characterized by fractal exponents $\nu_x = 1$ (which implies that the average projection X of a part of the trajectory on the x axis depends linearly on its length, measured along the trajectory, or on its "mass" M) and $\nu_y = 1/2$ (implying that the

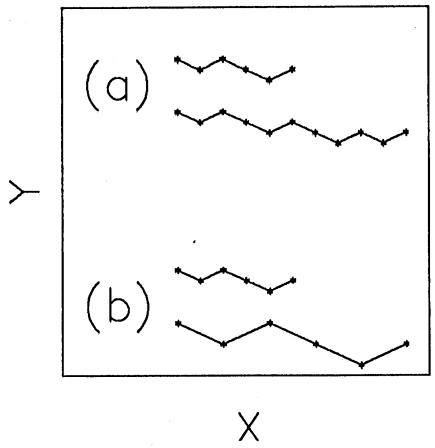

Figure 1. Two types of ensembles of biased random walk trajectories ("rivers") having the same internal fractal exponents $\nu_x = 1$, $\nu_y = 1/2$ but different external exponents α_x and α_y (two elements of each ensemble are shown). (a) The step length of the walk is preserved within the ensemble, which gives $\alpha_x = 1$, $\alpha_y = 1/2$, and (b) the number of steps is preserved within the ensemble, which gives $\alpha_x = 1$, $\alpha_y = 1$.

projection Y of a part of the trajectory on the y axis is proportional to the square root of the length of that part of the trajectory). Suppose now that one has an ensemble of biased random walk trajectories and wants to find its external fractal exponents α_x and α_y, i.e., find the dependence of the projections of the whole trajectory, X_0 and Y_0, on the length of the trajectory M_0. It turns out that the values of the exponents α_x and α_y depend on the way the ensemble is constructed. If the length of the jump is preserved within the ensemble, as shown in Figure 1a (e.g., one can think of rivers having similar hydrologic characteristics and therefore the same sinuosity), then a shorter trajectory is statistically equivalent to a part of same length of the longer trajectory; that is, it has the same projection. Therefore the external exponents of the ensemble α_x and α_y are equal to the internal exponents ν_x and ν_y of each trajectory. However, in another ensemble, shown in Figure 1b, where the trajectories have the same number of jumps but each trajectory has a different jump length (e.g., one can think of rivers having different widths and therefore different characteristic lengths of persistence of the direction of their flows), both projections X_0 and Y_0 of trajectories are obviously proportional to the length of the trajectories, i.e., $\alpha_x = \alpha_y = 1$, different from the internal exponents $\nu_x = 1$ and $\nu_y = 1/2$.

2. In some cases the ensemble of objects is characterized by the external exponents, but the internal exponents of the objects are not defined uniquely at all. As the simplest case, let us consider here compact objects. For example, Scheidegger river networks obtained by computer simulation are shown to be compact objects, and their ensemble is characterized by the values $\alpha_x = 2/3$, $\alpha_y = 1/3$ [*Kondoh et al.*, 1987, p. 1913; *Meakin et al.*, 1991, p. 409]. It is implied (e.g., see discussion after equation (4) of *Kondoh et al.* [1987]) that these exponents characterize the fractal geometry of the networks. However, the compactness of a two-dimensional object means that the object is just a piece of a plane. This, in turn, means that in contrast to the external components α_x and α_y, which characterize the ensemble of the networks, the internal exponents characterizing their geometry are not defined uniquely. For instance, it is quite obvious that a piece of a plane can be treated as a self-similar object as well and can be characterized by $\nu_x = \nu_y = 1/D = 1/2$. The nonuniqueness of the fractal exponents ν_x and ν_y can arise for noncompact objects too. *Sapozhnikov and Foufoula-Georgiou* [1995] showed that a class of noncompact fractal objects exists for which the internal exponents ν_x and ν_y are still not defined uniquely and derived general conditions under which an object falls into this class.

The above examples demonstrate that the external exponents α_x and α_y not only require a set of patterns for their estimation but, generally speaking, are something different from the internal exponents ν_x and ν_y. Therefore *Sapozhnikov and Foufoula-Georgiou* [1995] elaborated a method that enabled extraction of the internal fractal exponents from a pattern of an object of any topology. This method is briefly presented in the next section. The reader is referred to *Sapozhnikov and Foufoula-Georgiou* [1995] for more details and example applications.

3. A Logarithmic Correlation Integral Method for Studying the Geometry of Self-Affine Objects

3.1. Estimation of the Fractal Exponents ν_x and ν_y

Let us write the scaling equation (equation (3)) describing a self-affine object in the form

$$(X_2/X_1)^{1/\nu_x} = (Y_2/Y_1)^{1/\nu_y} = (M_2/M_1). \tag{4}$$

where $M_1 \equiv M(X_1, Y_1)$ is the mass of the object within a rectangle of size $X_1 \times Y_1$ and M_2 is similarly defined. Introducing $x = \log X$, $y = \log Y$, and $z = \log M$, we rewrite the above equation as

$$\frac{x_2 - x_1}{\nu_x} = \frac{y_2 - y_1}{\nu_y} = z_2 - z_1, \tag{5}$$

or

$$(dx/\nu_x) = (dy/\nu_y) = dz. \tag{6}$$

The function $M(X, Y)$ is known as the correlation integral [see *Grassberger and Procaccia*, 1982, p. 191]. Here by analogy we call the function $z(x, y)$ logarithmic correlation integral of the object under study.

Notice from (5) and (6) that $z(x, y)$ is a cylindric surface i.e., a surface that has constant derivative in a specific direction (the direction of the cylinder generating line). The second equality in (6) is true only if the first one is true. Comparing (6) with the generic equation of the differential of the $z(x, y)$ function, that is, $(\partial z/\partial x)\, dx + (\partial z/\partial y)\, dy = dz$, we obtain

$$\nu_x(\partial z/\partial x) + \nu_y(\partial z/\partial y) = 1. \tag{7}$$

The last relationship provides a method for estimating the fractal exponents ν_x and ν_y of a self-affine object. Indeed, having estimated the logarithmic correlation integral $z(x, y)$ from a pattern of the object (by direct calculation of the mass $M(X, Y)$ within rectangles of sizes $X \times Y$), one can calculate the derivatives $\partial z(x, y)/\partial x$ and $\partial z(x, y)/\partial y$ and use them to find the values of ν_x and ν_y that satisfy (7). Ideally, two points (x, y) giving different values of the derivatives $\partial z(x, y)/\partial x$ and $\partial z(x, y)/\partial y$ are sufficient, but for a good estimation it is preferable to compute the derivatives at all (x, y) points and follow a least squares estimation technique. The effectiveness

of this method in estimating the self-affine fractal exponents from single patterns is demonstrated by *Sapozhnikov and Foufoula-Georgiou* [1995] using simulated fractal objects.

3.2. Quantifying the Other Correlation Characteristics of Self-Affine Objects

The solution of (7), as well as of (6), is

$$z(x, y) = \frac{x}{2\nu_x} + \frac{y}{2\nu_y} + \omega\left(\frac{x}{2\nu_x} - \frac{y}{2\nu_y}\right), \tag{8}$$

where $\omega(\theta)$ is an arbitrary function of $\theta = [(x/2\nu_x) - (y/2\nu_y)]$.

Relationship (8) shows that the fractal exponents ν_x and ν_y contain only part of the information on the correlation properties of a fractal object. The rest of the information is contained in the function $\omega(\theta)$. Indeed, *Sapozhnikov and Foufoula-Georgiou* [1995, Figure 4] presented an example of fractal objects having the same values of ν_x and ν_y and different correlation properties because their $\omega(\theta)$ functions are different. It can be seen from (5) and (8) that while the fractal exponents ν_x and ν_y determine the direction of the generating line of the cylindric surface $z(x, y)$, the function $\omega(\theta)$ provides the additional information needed to describe the shape of any cross section of the cylindric surface. Thus together ν_x, ν_y, and $\omega(\theta)$ completely determine the shape of the logarithmic correlation integral surface $z(x, y)$.

By choosing the coordinate system (ξ, η, ζ), such that the (ξ, η) plane is perpendicular to the direction of the cylinder generating line, the surface $z(x, y)$ can be expressed as a function of one variable, $\eta(\xi)$, representing the curve of intersection of the cylinder with the (ξ, η) plane. *Sapozhnikov and Foufoula-Georgiou* [1995] showed that in this new coordinate system, the equation for the logarithmic correlation integral takes the form

$$\eta(\xi) = \frac{\nu_y^2 - \nu_x^2}{2\nu_x\nu_y\sqrt{1 + \nu_x^2 + \nu_y^2}}\,\xi + \frac{\sqrt{\nu_y^2 + \nu_x^2}}{\sqrt{1 + \nu_x^2 + \nu_y^2}}\,\omega\left(\frac{\sqrt{\nu_y^2 + \nu_x^2}}{2\nu_x\nu_y}\,\xi\right) \tag{9}$$

The function $\eta(\xi)$ is exactly what one sees viewing the $z(x, y)$ surface from the direction of the generating line. Since the (ξ, η) plane is orthogonal to the direction of the generating line, it is preferable to use $\eta(\xi)$ instead of $\omega(\theta)$ to describe the correlation properties of an object, since these properties are now not only complementary to the scaling exponents ν_x and ν_y (determining the direction of the generating line of the cylinder) but also independent of them.

It can be shown that the function $\omega(\theta)$ has two linear asymptotes at positive and negative infinities [see *Sapozhnikov and Foufoula-Georgiou*, 1995, p. 563]. This gives an important feature of the $z(x, y)$ surface, namely that, if large enough, it can be considered as composed of two asymptotic planes (see (14) and (15) below) and an intermediate zone between them. Also, it implies that $\eta'(\xi)$ has two asymptotic values, $\eta'(+\infty)$ and $\eta'(-\infty)$, which can be used to quantify the correlation characteristics of a self-affine object, other than the fractal exponents ν_x and ν_y. In particular, we introduce two parameters characterizing the correlation properties of self-affine objects: the "nonscaling anisotropy parameter" δ defined as

$$\delta \equiv [\eta'(-\infty) + \eta'(+\infty)]/2 \tag{10}$$

and the "curvature parameter" κ defined as

$$\kappa \equiv [\eta'(-\infty) - \eta'(+\infty)]/2 \tag{11}$$

These two parameters are important characteristics of a self-affine object and complement the information contained in the fractal exponents ν_x and ν_y. The value of δ characterizes the anisotropy of the cross section of the function $z(x, y)$. It is equal to zero when the cross section is isotropic and describes a different type of anisotropy of a self-affine object than the ratio of the scaling exponents ν_x/ν_y. In fact, *Sapozhnikov and Foufoula-Georgiou* [1995] showed that even a self-similar object ($\nu_x = \nu_y$) may have anisotropic correlation characteristics which are indicated by $\delta \neq 0$. To distinguish between these two types of anisotropy, we coined the terms "scaling anisotropy parameter" for ν_x/ν_y and "nonscaling anisotropy parameter" for δ. The parameter κ is a measure of curvature of $z(x, y)$. *Sapozhnikov and Foufoula-Georgiou* [1995] showed that if it is equal to zero, that is, the cylindric surface $z(x, y)$ degenerates into a plane, the exponents ν_x and ν_y of the fractal object are not defined uniquely.

3.3. Connection Between the Exponents ν_x and ν_y and Other Characteristics of Fractal Objects

Let D_{cx} and D_{cy} be the fractal dimensions of cross sections of the object in the directions of the x and y axes and D_{px2} and D_{py2} be the correlation fractal dimensions [see *Grassberger and Procaccia*, 1982] of the projections of the object on the x and y axes, respectively. Let us remind the reader that the generalized fractal dimensions D_q are

$$D_q = \lim_{\varepsilon \to 0} \frac{\log\left(\sum p_i^q\right)}{(q - 1)\log \varepsilon} \qquad q \neq 1 \tag{12}$$

$$D_1 = \lim_{\varepsilon \to 0} \frac{\sum p_i \log p_i}{\log \varepsilon}, \tag{13}$$

where p_i is the fraction of the measure in a box of size ε (in our case it is the fraction of the object that projects into an interval of size ε). D_0 is the fractal dimension of the support of the measure, and D_1 and D_2 are called information and correlation dimensions, respectively. Thus D_{px2} and D_{py2} are computed using (12) with $q = 2$ and with the p_i obtained using the projections of the object on the x and y axes.

Sapozhnikov and Foufoula-Georgiou [1995] showed the equations for the two asymptotic plane parts of the surface $z(x, y)$ to be

$$z_-(x, y) = D_{px2}x + D_{cy}y \tag{14}$$

$$z_+(x, y) = D_{cx}x + D_{py2}y \tag{15}$$

These relationships make it possible to demonstrate clearly what one gets when the fractal dimension of a self-affine object is determined: One finds how the mass within a $X \times Y$ rectangle changes as its sides change proportionally to each other. In other words, one just finds the slope of the section of the plane $z(x, y)$ by the plane $y = x + a$, where constant $a = \log(Y/X)$. If $\nu_x > \nu_y$, then for positive values of a $(Y > X)$, the plane $y = x + a$ will intersect only the $z_-(x, y)$ plane, while for negative values of a, both $z_-(x, y)$ and $z_+(x, y)$ planes will be intersected. That creates two slopes, corresponding to what is called global and local fractal dimensions of a self-affine object D_G and D_L, correspondingly [*Mandelbrot*,

1986]. Putting $y = x + a$ in (14) and (15), we obtain that for $\nu_x > \nu_y$

$$D_G = D_{px2} + D_{cy} \tag{16}$$

$$D_L = D_{py2} + D_{cx} \tag{17}$$

It is easy to see from (14), (15), and (7) that *Mandelbrot*'s [1986] expressions

$$D_G = (\nu_y - \nu_x + 1)/\nu_y, \tag{18}$$

$$D_L = (\nu_x - \nu_y + 1)/\nu_x \tag{19}$$

can be obtained as a special case (for $D_{px2} = D_{py2} = 1$) of the more general expressions derived here.

Another set of useful relations, obtained from (7), (14), and (15), is

$$\nu_x D_{cx} + \nu_y D_{py2} = 1 \tag{20}$$

$$\nu_x D_{px2} + \nu_y D_{cy} = 1. \tag{21}$$

For example, these relationships can be used for estimation of ν_x and ν_y, given D_{cx}, D_{cy}, D_{px2}, and D_{py2}. Notice that for a self-similar object, (20) and (21) give

$$D_{cx} + D_{py2} = D_{cy} + D_{px2} = D \tag{22}$$

where D is the fractal dimension of the object.

4. Study of Spatial Scaling in Three Natural Rivers

As mentioned in the introduction, braided rivers manifest salient features of their spatial structure at scales below their width, where branching comes into play. Therefore we focused in this study on scales smaller than the braid plain width. The patterns of three rivers were analyzed: the Brahmaputra River (Bangladesh), the Aichilik River (Alaska), and the Hulahula River (Alaska). We used the traced air and satellite photo images of these rivers and tried to capture anabranches up to the smallest possible width. The tracing was done by a geologist experienced in morphology of braided rivers and their field observation (A. Brad Murray, Department of Geology and Geophysics, University of Minnesota). In the tracing, only active channels, that is, channels which are connected to the drainage system, were included. The traced photo images were then digitized to produce images consisting of black and white pixels indicating the presence or absence of active channels. The pixel size for each river was chosen such that the resolution of the digitized image was at least as good as the resolution of the traced photo, so that no details of the tracing were lost due to digitization.

The Brahmaputra is one of the world's largest rivers. It starts at Tibet and joins the Ganges near the Bay of Bengal. It is a very dynamic sand-bed river, with intensive bank erosion, mobile sand bars, less mobile islands, and frequent shifting of anabranches and switching flows between anabranches. The braid plain width of the Brahmaputra River reaches 20 km. The mean discharge is around 12,200 m^3/s. The hydrograph of the Brahmaputra River shows high annual variations, with lower flows in winter and high flows in summer (causing severe floods). Its highly dynamic nature causes a serious threat to the surrounding cities and villages and presents considerable problems for designers of bridges, roads, and other adjacent constructions. The river carries about 500 million tons of sediment annually, mostly silt and sand. Figure 2a shows the digitized image of the reach of the Brahmaputra River between Teesta and Ganges confluences, in winter stage.

The Aichilik and Hulahula Rivers are located at the North Slope of Alaska. The Aichilik is a gravel-bed river, with dominantly gravel to cobble-sized load. The gravel braid plain width is about 0.5 km. The river is fed largely by snow and permafrost melt. The Hulahula is a gravel-bed river, similar to the Aichilik except that it is a little larger (its braid plain is about 0.7 km) and largely glacially fed. The digitized photo images of the studied sections of the Aichilik and Hulahula Rivers are shown in Figures 2b and 2c, respectively. Some hydrologic and geomorphologic characteristics of the three rivers are summarized in Table 1. It can be seen from Table 1 that the rivers under study are characterized by large differences in their scales, slopes, and type of bed material. The braiding index (BI) for each river was computed as the average number of channels in cross sections of the photo image of the river (see *Bristow and Best* [1993] for several definitions of BI). Note that the BI is a resolution dependent quantity and therefore the BI values reported in Table 1, although properly reflecting the geometry of the analyzed images, are not directly comparable to each other due to the different resolution of the analyzed images. For example, in the case of the Brahmaputra River the computed BI value is lower than its actual value since the sizes of the smallest existing channels are below the resolution of the photo used in this analysis.

First, a traditional fractal analysis was applied. Square boxes of size R were positioned around every black pixel (i.e., every pixel indicating the presence of active channels), and the average number of black pixels within squares of size R was computed. The "mass" $M(R)$ was then calculated by multiplying this average number of pixels by the area of a pixel. Figures 3a, 3b, and 3c present in log-log scale the dependence of M on R for the Brahmaputra, Aichilik, and Hulahula Rivers, respectively. For the Brahmaputra River the dependence follows a straight line up to the scale of 15 km, and the slope of the line is 1.50. For the Aichilik and Hulahula Rivers, scaling is observed up to scales of 0.5 km and 0.7 km, respectively, and the slopes of the best fit straight lines are 1.58 and 1.54, respectively. One can see that for all three rivers, the upper scale of linearity of these lines coincides with the rivers' width shown in Table 1. The estimated values of the fractal dimensions agree with the results of *Nikora et al.* [1995], who found fractal dimension $D = 1.5$–1.7 for several New Zealand braided rivers using a box-counting method (number of cells containing the pattern as a function of the grid cell size). However, the linear (in log-log scale) $M(R)$ dependence itself does not show whether the object is self-similar or self-affine. Indeed, self-affine objects can still show linear log-log dependence of $M(R)$. As demonstrated in section 3 (see (14) and (15) and discussion afterward) the $M(R)$ dependence may have either two slopes at different scales (D_L at smaller scale and D_G at bigger scale) or one slope D_G. For example, in the case of the biased random walk considered in section 2, if the steps in the X direction have the same length as the steps in the Y direction, one obtains just one trivial fractal dimension $D_G = 1$ which obviously does not reflect fully the scaling properties of this self-affine object expressed by the fractal exponents $\nu_x = 1$, $\nu_y = 1/2$.

To find the fractal exponents of the braided rivers under investigation, we first estimated their logarithmic correlation integrals $z(x, y)$ from the patterns of the rivers. The x axis was

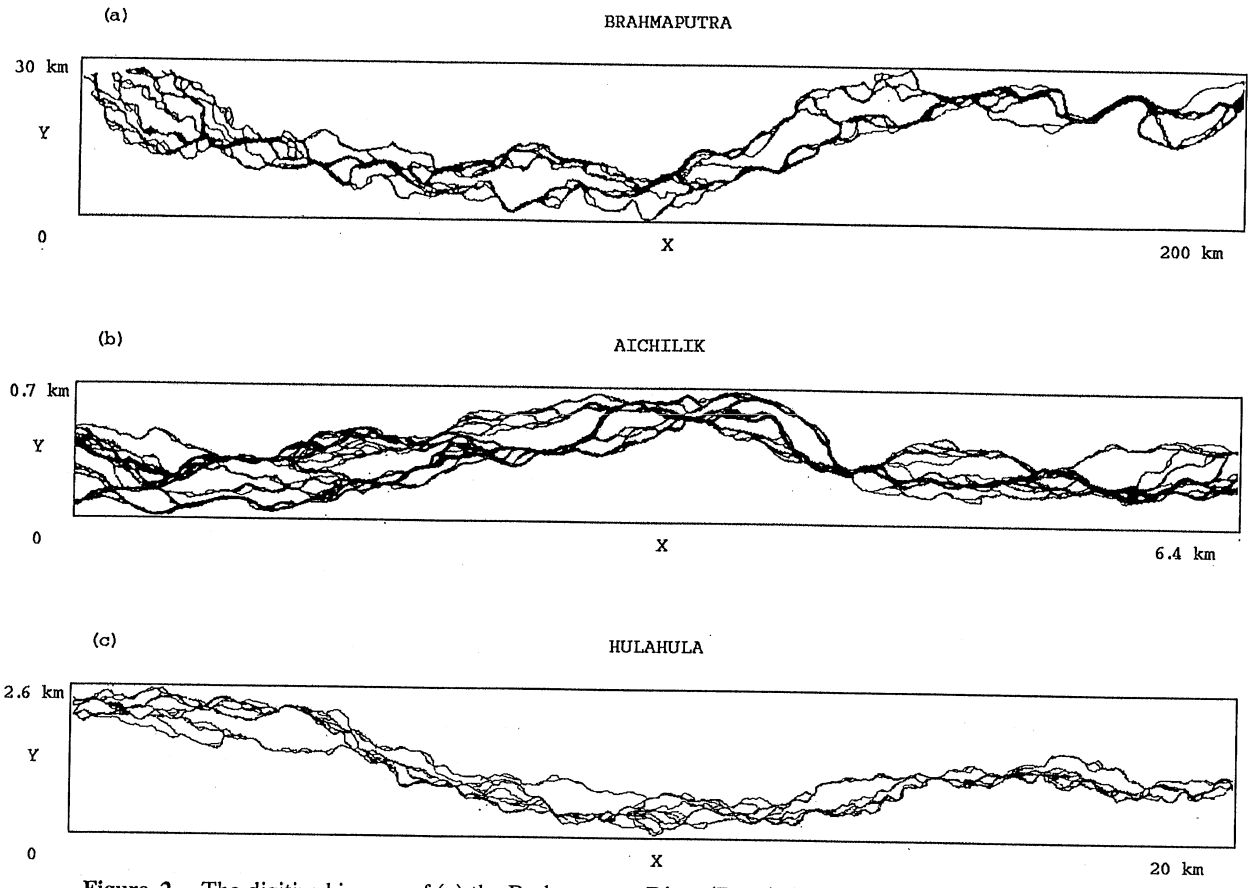

Figure 2. The digitized images of (a) the Brahmaputra River (Bangladesh), (b) the Aichilik River (Alaska), and (c) the Hulahula River (Alaska).

oriented along the line connecting the beginning and the end of the analyzed section of each river. The $z(x, y)$ surface for the Brahmaputra River is presented in Figure 4; the surfaces for the other two rivers look similar and are not shown here. From the correlation integral surfaces $z(x, y)$ we calculated numerically the derivatives $\partial z(x, y)/\partial x$ and $\partial z(x, y)/\partial y$ and plotted the dependence $\partial z(x, y)/\partial y$ versus $\partial z(x, y)/\partial x$. The dependence for the Brahmaputra River is presented in Figure 5a. According to (7), in the self-affinity region the partial derivatives should show linear dependence. However, one can see that while the upper part of the plot in Figure 5a shows linearity, the dependence breaks in the lower part of the plot. It is natural to expect that there is a scaling break at a certain scale, namely for Y values bigger than the average width of the river (approximately 15 km). This scaling break is also reflected in Figure 3a, showing deviation from the straight line for scales greater than 15 km. To check if the points in the lower part of the plot come from this range of scales, we cut off the part of the $z(x, y)$ surface corresponding to the Y values higher than 15 km (see Figure 6 for the truncated $z(x, y)$ surface of the Brahmaputra River). Figure 7a displays the values of the partial derivatives coming from the part of the correlation integral shown in Figure 6. The points show a good linear dependence, indicating that this part of the $z(x, y)$ surface is cylindric; that is, the Brahmaputra River exhibits spatial scaling within the examined scales of Y (0.4–15 km: the width of the smallest included channels to braid plain width). Using (7) we calculated the values of the fractal exponents for the Brahmaputra River. They are $\nu_x = 0.74$ and $\nu_y = 0.51$. Similar analysis applied to the Aichilik and Hulahula Rivers

Table 1. Hydrologic and Geomorphologic Characteristics of the Studied Rivers

	Brahmaputra	Aichilik	Hulahula
Reach width, km	15	0.5	0.7
Reach length, km	200	6.4	20
Mean channel depth, m	5	1	1
Slope	0.000077	0.001	0.0007
Braiding index*	3.8	6.8	5.2
Predominant type of the bed material	sand	gravel	gravel

*The braiding index (BI) for each river was computed as the average number of channels in cross sections of the photo image of the river (see section 4 for more discussion).

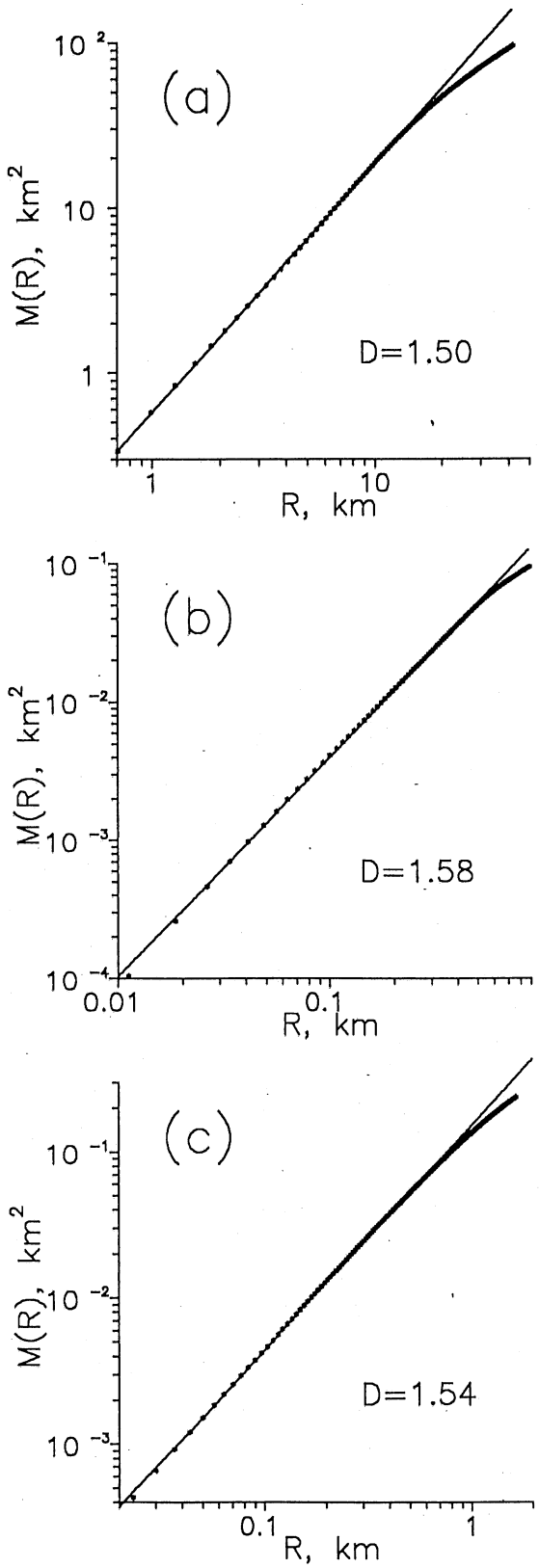

Figure 3. Spatial scaling in the (a) Brahmaputra, (b) Aichilik. and (c) Hulahula Rivers indicated by straight-line log-log dependence of the "mass" M on the size of the square box R (see text for the definition). The slopes of the straight lines give the values of the fractal dimensions D.

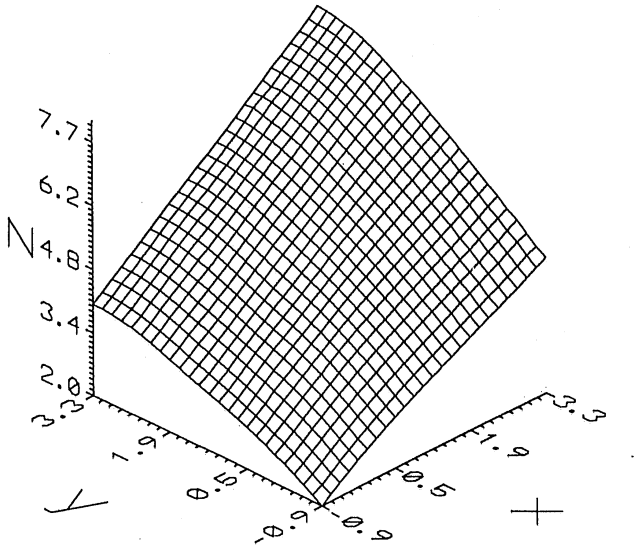

Figure 4. Logarithmic correlation integral surface $z(x, y)$ of the Brahmaputra River.

(Figures 5b, 5c, 7b, and 7c) gave fractal exponents $\nu_x = 0.72$, $\nu_y = 0.51$ and $\nu_x = 0.74$, $\nu_y = 0.52$, respectively. These results imply that all three rivers are self-affine objects showing a rather high degree of anisotropy: $\nu_x/\nu_y = 1.45$ for the Brahmaputra, $\nu_x/\nu_y = 1.41$ for the Aichilik, and $\nu_x/\nu_y = 1.42$ for the Hulahula. The values of the fractal exponents ν_x and ν_y agree with the results of the traditional fractal analysis shown in Figures 3a, 3b, and 3c ("mass" within a box as a function of the box size) which is expected to show a slope equal to the value of the global fractal dimension D_G for a self-affine object. Indeed, for the estimated values of ν_x and ν_y the global fractal dimensions according to *Mandelbrot* [1986] (see also (18) here) are found to be $D_G = 1.51$ for the Brahmaputra, $D_G = 1.55$ for the Aichilik, and $D_G = 1.50$ for the Hulahula. These values are very close to the corresponding values of D obtained previously from the slopes of $M(R)$ log-log linear dependence (1.50, 1.58, and 1.54, respectively). The results of the analysis are summarized in Table 2.

Since the function $z(x, y)$ of a fractal object is a cylindric surface it can be viewed in the direction of the cylinder generating line (see (5) and (6)). In other words, it is possible to adjust the rotation angle φ about the z axis and the tile angle ψ above the (x, y) plane from which the surface is viewed to see only the edge of the surface (which is the $\eta(\xi)$ function of (9)). It is not difficult to show that the following relationships connecting the angles and the exponents hold

$$\tan \varphi = \nu_x/\nu_y \tag{23}$$

$$\sin \psi = (1 + \nu_x^2 + \nu_y^2)^{-1/2}. \tag{24}$$

Figure 8 shows the $z(x, y)$ surface of the Brahmaputra River viewed from the angles $\varphi = 36.6°$ and $\psi = 47.7°$ determined by (23) and (24). It can be seen that $z(x, y)$ really represents a cylindric surface and that the angles φ and ψ correspond to relationships (23) and (24). What one sees in Figure 8 is a cross section of the cylindric surface $z(x, y)$ by a plane perpendicular to the cylinder generating line; that is, one sees the $\eta(\xi)$ function (9). By the same procedure we rotated the $z(x, y)$

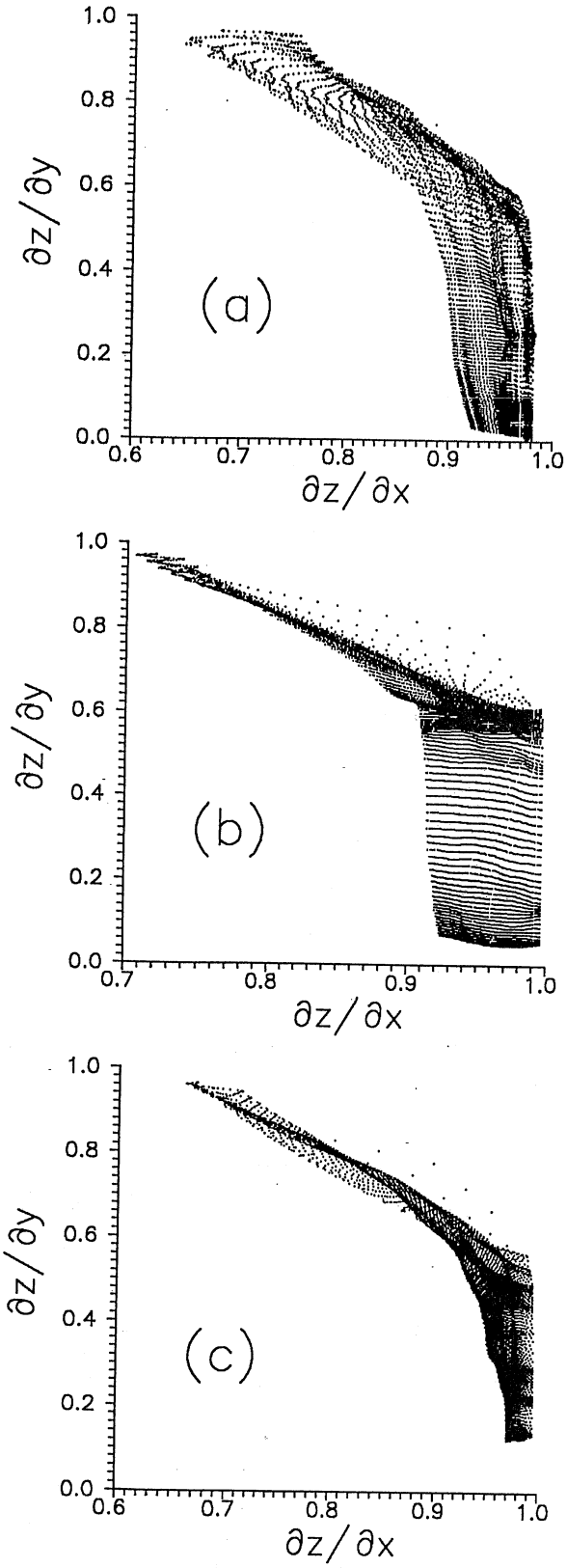

Figure 5. Dependence $\partial z(x, y)/\partial y$ versus $\partial z(x, y)/\partial x$ for the (a) Brahmaputra, (b) Aichilik, and (c) Hulahula Rivers. The partial derivatives are estimated from the entire correlation integral surfaces $z(x, y)$ of the rivers (see Figure 4 for the $z(x, y)$ surface of the Brahmaputra).

surfaces of the Aichilik and Hulahula Rivers at the appropriate φ and ψ angles and found that they look similar to the rotated $z(x, y)$ surface of the Brahmaputra River shown in Figure 8.

As we already stated, the $z(x, y)$ surface of a self-affine object asymptotically approaches two planes (one when $x/2\nu_x - y/2\nu_y$ is a large positive value and the other when it is a large negative value). Therefore, if the $z(x, y)$ surface is large enough to reach its asymptotic behavior, one can think of it as being composed of two planes and an intermediate zone between them. The analysis of the $z(x, y)$ functions of all three rivers shows that they do not reach their asymptotic behavior within the studied region; that is, we deal only with the intermediate zone in this case. This did not allow us to estimate reliably the values of D_{cx}, D_{cy}, D_{px2}, D_{py2}, and accordingly, the anisotropy parameter δ and curvature parameter κ. Rough estimates show that they are both of the order of 0.1, i.e., small values, which implies that the $z(x, y)$ surfaces are not inclined significantly to the x or y axes (indicating that there is no significant nonscaling anisotropy in the patterns of the analyzed rivers) and are not very curved.

5. Robustness of Scaling Exponent Estimates

In studying a natural river for self-affine scaling with the proposed method, there are three sources of subjectivity (and therefore uncertainty) which can potentially affect the obtained estimates of fractal exponents. The first source of subjectivity relates to the procedure of tracing the river image from an aerial photograph, the second relates to the selection of the orientation of the coordinate axes, and the third relates to the choice of the portion of the $z(x, y)$ surface used for estimation of the fractal exponents ν_x and ν_y. The sensitivity of the obtained estimates to these three factors gives an indication of the robustness of the proposed method in estimating the self-affine structure of a natural braided river.

In tracing the river image from an aerial photograph one must decide whether or not to include small channels that are on the threshold of vision. To test the sensitivity of the esti-

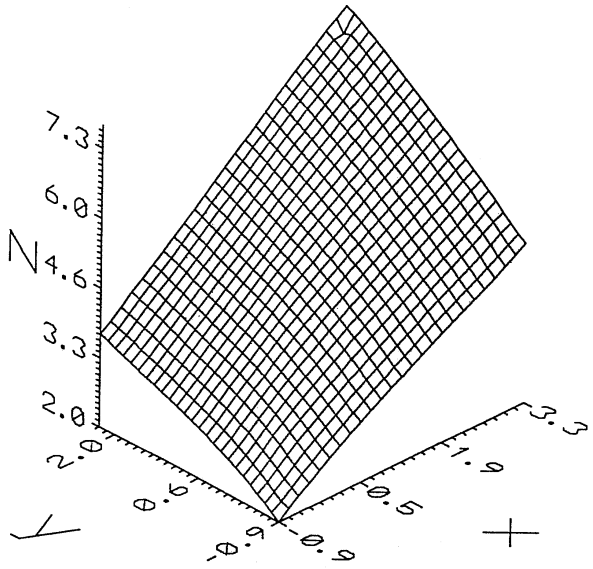

Figure 6. Truncated logarithmic correlation integral surface $z(x, y)$ of the Brahmaputra River.

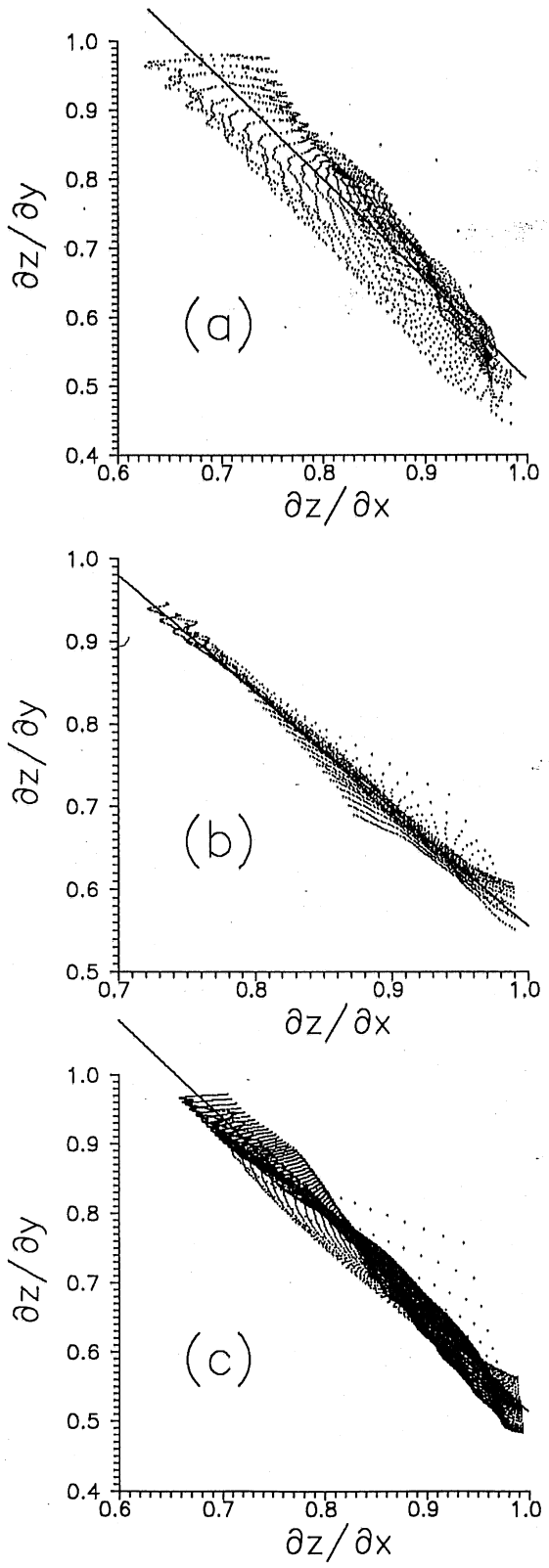

Figure 7. Estimation of the fractal exponents ν_x and ν_y for the (a) Brahmaputra, (b) Aichilik, and (c) Hulahula Rivers from the truncated parts of the $z(x, y)$ surfaces (see Figures 6 and 8). Advantage is taken of (7). The estimated values are $\nu_x = 0.74$, $\nu_y = 0.51$ for Figure 7a, $\nu_x = 0.72$, $\nu_y = 0.51$ for Figure 7b, and $\nu_x = 0.74$, $\nu_y = 0.52$ for Figure 7c.

Table 2. Fractal Characteristics of the Studied Rivers

River	ν_x	ν_y	ν_x/ν_y	D_G, (18)	D, (2)
Brahmaputra	0.74	0.51	1.45	1.51	1.50
Aichilik	0.72	0.51	1.41	1.55	1.58
Hulahula	0.74	0.52	1.42	1.50	1.54

mated values of fractal exponents ν_x and ν_y to the tracing procedure, we analyzed two tracings of the same aerial photograph of the Aichilik River. The first tracing, for which the results were reported in the previous section, included all visible channels, while the second tracing did not include the smallest, and therefore questionable, channels. The estimated values of the fractal exponents for the second tracing were $\nu_x = 0.78$ and $\nu_y = 0.55$, not very different from the corresponding exponents of the tracing which included all small channels ($\nu_x = 0.72$ and $\nu_y = 0.51$). The anisotropy parameter $\nu_x/\nu_y = 1.42$ was practically the same as in the first tracing ($\nu_x/\nu_y = 1.41$). Quite naturally, for this tracing, because of absence of small details, the scaling breaks at small scales, so that up to the width of the smallest included channels (25 m) the $M(R)$ dependence has a slope close to 2. For the same reason the $z(x, y)$ surface of this tracing also deviated from a cylindric surface up to the scales of 15 m. This observation suggests that the self-affinity of braided rivers, observed up to the rivers' width, starts at the scales of the width of the smallest channels.

In our analysis the coordinate system was oriented such that the x axis is directed along the line connecting the endpoints of the analyzed section of the river. However, because this coordinate system depends on the analyzed segment of the river, the sensitivity of the obtained estimates to the orientation of the coordinates system was tested. For that we rotated the coordinate system in the Brahmaputra River by 8° counterclockwise. This value corresponds to deviation of the x axis from one of the endpoints of the analyzed section by approximately two widths of the river. This rotation changed the

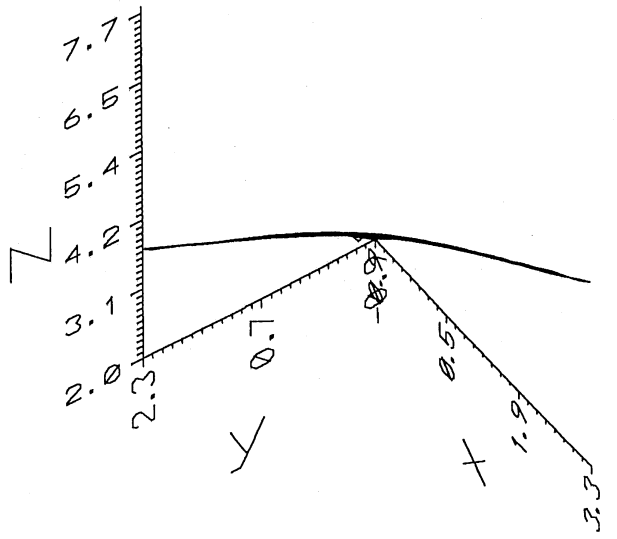

Figure 8. Truncated logarithmic correlation integral surface $z(x, y)$ of the Brahmaputra River viewed from the direction of the cylinder generating line (see (23) and (24)).

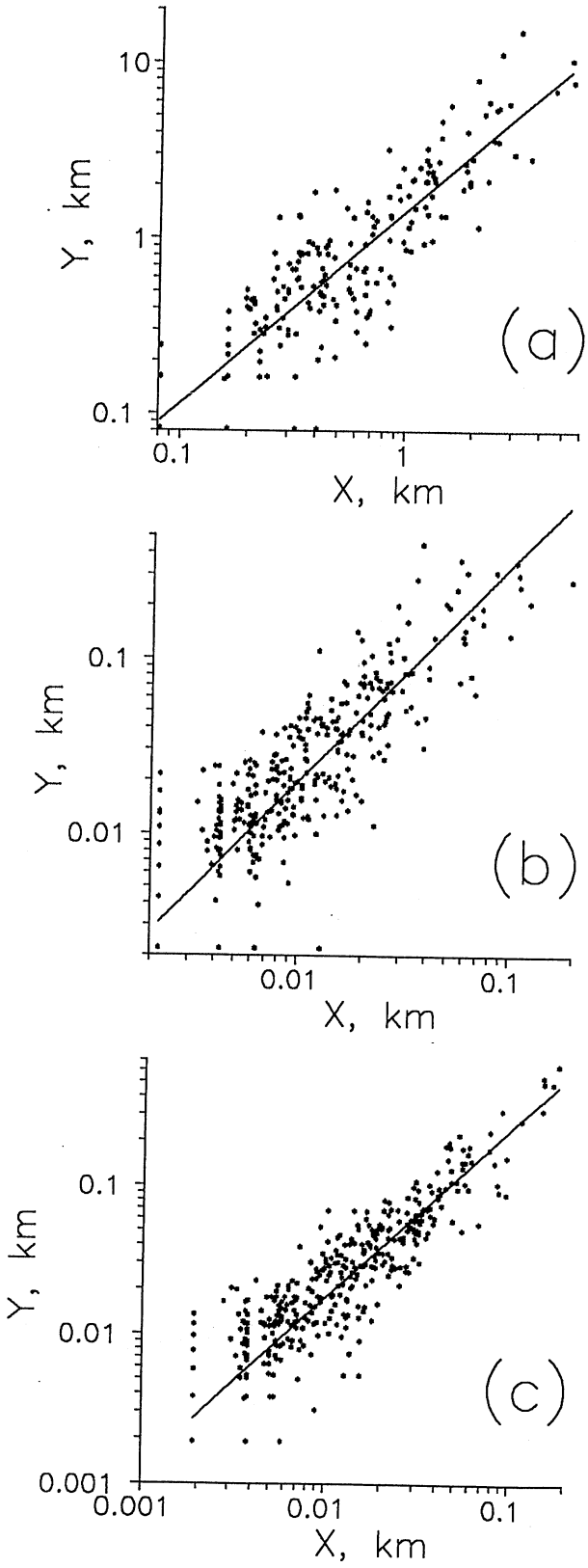

Figure 9. Scaling in the projections of the islands on the x and y axes. The slopes are different from 1, indicating scaling anisotropy. The estimated values of the slopes are (a) 1.2 for the Brahmaputra, (b) 1.3 for the Aichilik, and (c) 1.2 for the Hulahula.

Table 3. Average Fractal Characteristics of Single-Channel Rivers, River Networks, and Braided Rivers

Objects	ν_x	ν_y	ν_x/ν_y	D_G, (18)
Single-channel rivers*	~1	~0.5	~2	~1
River networks†	0.62	0.47	1.32	1.83
Braided rivers‡	0.73	0.51	1.43	1.52

*Reaches of the Dniester and Pruth Rivers in Moldova [*Nikora et al.*, 1993].
†Sixty river networks [*Nikora and Sapozhnikov*, 1993; *Nikora*, 1994].
‡This study.

values of the fractal exponents only slightly from $\nu_x = 0.74$, $\nu_y = 0.51$ to $\nu_x = 0.73$, $\nu_y = 0.54$. Naturally, since we artificially deviated from the real direction of the river, the anisotropy in spatial scaling decreased somewhat (from $\nu_x/\nu_y = 1.45$ for the initial picture to $\nu_x/\nu_y = 1.35$ for the rotated one).

Another element of subjectivity comes from choosing the portion of the logarithmic correlation integral surface $z(x, y)$ for estimating the self-affine characteristics of the object. This problem is similar to that of choosing the portion of the log-log $M(R)$ plot for straight-line fit in a traditional fractal analysis (see Figures 3a, 3b, and 3c). The choice of the portion of the $z(x, y)$ surface affects the estimated values of the fractal exponents. We tested our method by selecting different portions of the $z(x, y)$ surface for analysis (see Figures 6 and 8) and then calculating the fractal exponents for each. The test gave the following small ranges of the fractal exponents: for the Brahmaputra River, $\nu_x = 0.73$–0.75 and $\nu_y = 0.51$–0.55; for the Aichilik River, $\nu_x = 0.71$–0.74 and $\nu_y = 0.50$–0.52; for the Hulahula River, $\nu_x = 0.71$–0.75 and $\nu_y = 0.50$–0.54.

The results of these tests indicate that our method for analyzing and estimating scaling in self-affine natural objects is reasonably robust. However, one cannot expect it to be as robust as traditional fractal analysis because it reveals subtler features of spatial scaling of the objects.

6. Scaling in the Sizes of Islands

As another indicator of scaling anisotropy we also studied sizes of islands (here we did not distinguish between islands and exposed bars surrounded by water). The log-log plots of the projections of the islands on the x and y axes, ΔX and ΔY, respectively, displayed in Figures 9a, 9b, and 9c, reveal scaling. The slopes are different from 1, indicating anisotropy in scaling of the islands in X and Y directions. The slopes of these plots are 1.2 for the Brahmaputra, 1.3 for the Aichilik, and 1.2 for the Hulahula. They are lower than the obtained values of the scaling anisotropy parameters for the rivers, ν_x/ν_y, which were equal to 1.45, 1.41, and 1.42, respectively. In our opinion this difference implies that the scaling anisotropy of a braided river is only partially reflected by the anisotropy of islands; part of the anisotropy in a braided river stems from the anisotropy in tortuosity of the river (same as anisotropy in tortuosity of single-channel rivers causing their scaling anisotropy). These two factors exist on scales which overlap and therefore cannot be separated. The relations between scaling anisotropy in size distribution of islands and fractal structure of a braided river need further study, which is outside the scope of the present article.

7. Concluding Remarks

Within the scales of their width the three studied rivers (the Brahmaputra in Bangladesh and the Aichilik and Hulahula in Alaska) are self-affine, with fractal exponents $\nu_x = 0.72–0.74$ and $\nu_y = 0.51–0.52$. Table 3 enables one to compare these fractal exponents with the fractal exponents of other self-affine hydrologic objects. In Table 3 the average fractal characteristics of the analyzed braided rivers are listed together with the average fractal characteristics (in the self-affinity regions) of single-channel rivers Dniester and Pruth [*Nikora et al.*, 1993] and of 60 river networks [*Nikora and Sapozhnikov*, 1993; *Nikora*, 1994]. Comparison of the fractal characteristics of the hydrologic objects summarized in Table 3 suggests a conclusion that braided rivers form a class of fractal objects which lies between the classes of single-channel rivers and river networks. Indeed, the scaling anisotropy of braided rivers (characterized by the ν_x/ν_y value) is lower than that of single-channel rivers but higher than that of river networks; the global fractal dimension D_G shows that braided rivers fill the surface more densely than single-channel rivers but not as densely as river networks. It should be noticed that in contrast to the single-channel rivers, no self-similarity range of scales was revealed in the studied braided rivers. In our opinion the absence of the self-similarity region in braided rivers is related to the lower sinuosity of their channels [see *Friend and Sinha*, 1993, p. 110].

The fact that despite big difference in scales, slopes, and types of bed material (see Table 1) the analyzed braided rivers show similar spatial scaling is worthy of notice. It might indicate that the spatial structure of braided rivers is determined by universal physical mechanisms. However, more braided rivers need to be studied to validate this hypothesis.

The study of the fractal geometry of braided rivers and scaling in their hydrologic characteristics can eventually help to relate their geometry to the hydrologic characteristics and dynamics of the rivers, as it was partially done for individual streams and river networks. This is a challenging area of research which we are currently pursuing with the help of experimentally produced braided rivers in our laboratory.

Acknowledgments. This research was partially supported by NSF grant BSC-8957469 and NASA grant NAG-52108. Supercomputer resources were kindly provided by the Minnesota Supercomputer Institute. The aerial photographs for the Aichilik and Hulahula Rivers were provided to us by Chris Paola's group at the Department of Geology and Geophysics, University of Minnesota, and the tracing was performed by A. Brad Murray. Without their help this study would not have been possible.

References

Bristow, C., and J. Best, Braided rivers: Perspectives and problems, in *Braided Rivers*, edited by J. Best and C. Bristow, pp. 1–11, Geol. Soc., London, 1993.

Friend, P. F., and R. Sinha, Braiding and meandering parameters, in *Braided Rivers*, edited by J. Best and C. Bristow, pp. 105–111, Geol. Soc., London, 1993.

Grassberger, P., and I. Procaccia, Measuring of strangeness of strange attractors, *Physica D*, *9*, 189–208, 1982.

Howard, A. D., M. E. Keetch, and C. L. Vincent, Topological and geometrical properties of braided streams, *Water Resour. Res.*, *6*, 1674–1688, 1970.

Ijjasz-Vasquez, E. I., R. Bras, and I. Rodriguez-Iturbe, Self-affine scaling of fractal river courses and basin boundaries, *Physica A*, *209*, 288–300, 1994.

Kondoh, H., M. Matsushita, and Y. Fukuda, Self-affinity of Scheidegger's river patterns, *J. Phys. Soc. Jpn.*, *56*, 1913–1915, 1987.

La Barbera, P., and R. Rosso, On the fractal dimension of stream networks, *Water Resour. Res.*, *25*, 735–741, 1989.

Lane, E., *A Study of the Shape of Channels Formed by Natural Streams Flowing in Erodable Material, M.R.D. Sediment Ser.*, vol. 9, U.S. Army Eng. Div., Mo. River, Corps Eng., Omaha, Neb., 1957.

Mandelbrot, B. B., *The Fractal Geometry of Nature*, W. H. Freeman, New York, 1982.

Mandelbrot, B. B., Self-affine fractal sets, in *Fractals in Physics, Proceedings of the Sixth Trieste International Symposium on Fractals in Physics, ICTP, Trieste, Italy*, edited by L. Petroniero and E. Tosatti, pp. 3–16, North-Holland, New York, 1986.

Matsushita, M., and S. Ouchi, On the self-affinity of various curves, *Physica D*, *38*, 246–251, 1989.

Meakin, P., J. Feder, and T. Jossang, Simple statistical models for river networks, *Physica A*, *176*, 409–429, 1991.

Murray, A. B., Braided-stream modeling and model evaluation: Dynamical-systems approaches, Ph.D. thesis, Univ. of Minnesota, Minneapolis, 1995.

Murray, A. B., and C. Paola, A cellular automata model of braided rivers, *Nature*, *371*, 54–57, 1994.

Murray, A. B., and C. Paola, A new quantitative test of geomorphic models, applied to a model of braided streams, *Water Resour. Res.*, in press, 1996.

Nikora, V. I., Fractal structures of river plan forms, *Water Resour. Res.*, *27*, 1327–1333, 1991.

Nikora, V. I., On self-similarity and self-affinity of drainage basins, *Water Resour. Res.*, *30*, 133–137, 1994.

Nikora, V. I., and V. B. Sapozhnikov, River network fractal geometry and its computer simulation, *Water Resour. Res.*, *29*, 3569–3575, 1993.

Nikora, V. I., V. B. Sapozhnikov, and D. A. Noever, Fractal geometry of individual river channels and its computer simulation, *Water Resour. Res.*, *29*, 3561–3568, 1993.

Nikora, V. I., D. M. Hicks, G. M. Smart, and D. A. Noever, Some fractal properties of braided rivers, paper presented at the 2nd International Symposium on Fractals and Dynamic Systems in Geoscience, Johann Wolfgang Goethe Univ., Frankfurt/Main, Germany, April 4–7, 1995.

Peckham, S. D., New results for self-similar trees with application to river networks, *Water Resour. Res.*, *31*, 1023–1029, 1995.

Rodriguez-Iturbe, I., E. Ijjasz-Vasquez, R. Bras, and D. Tarboton, Power law distributions of discharge mass and energy in river basins, *Water Resour. Res.*, *28*, 1089–1093, 1992.

Sapozhnikov, V. B., and E. Foufoula-Georgiou, Study of self-similar and self-affine objects using logarithmic correlation integral, *J. Phys. A Math. Gen.*, *28*, 559–571, 1995.

Sapozhnikov, V. B., and V. I. Nikora, Simple computer model of a fractal river network with fractal individual watercourses, *J. Phys. A Math. Gen.*, *26*, L623–L627, 1993.

Tarboton, D. G., R. L. Bras, and I. Rodriguez-Iturbe, The fractal nature of river networks, *Water Resour. Res.*, *24*, 1317–1322, 1988.

Webb, E. K., Simulation of braided channel topology and topography, *Water Resour. Res.*, *31*, 2603–2611, 1995.

E. Foufoula-Georgiou and V. Sapozhnikov, St. Anthony Falls Laboratory, University of Minnesota, Mississippi River at Third Avenue S.E., Minneapolis, MN 55414. (e-mail: sapoz001@maroon.tc.umn.edu)

(Received July 24, 1995; revised February 6, 1996; accepted February 8, 1996.)

WATER RESOURCES RESEARCH, VOL. 32, NO. 4, PAGES 1109–1112, APRIL 1996

Do the current landscape evolution models show self-organized criticality?

St. Anthony Falls Laboratory
Technical Paper No. 453, Series A

Victor B. Sapozhnikov and Efi Foufoula-Georgiou
St. Anthony Falls Laboratory, University of Minnesota, Minneapolis

Abstract. In this note we question the relevance of the self-organized criticality concept as currently applied to landscape evolution modeling. We also express concerns about possible inference problems in testing hypotheses about landscape multifractality using simulated landscapes.

1. Introduction

Landscape and river network evolution modeling is an active area of research [e.g., *Willgoose et al.*, 1991a, b; *Howard*, 1994; *Kramer and Marder*, 1992; *Leheny and Nagel*, 1993; *Takayasu and Inaoka*, 1992; *Rinaldo et al.*, 1993; *Rigon et al.*, 1994; *Rodriguez-Iturbe et al.*, 1994]. In this article we concentrate on the work of *Takayasu and Inaoka* [1992] and *Rinaldo et al.* [1993] (see also *Rigon et al.* [1994] and *Rodriguez-Iturbe et al.* [1994]), who presented models for river networks and landscape evolution and claimed that their behavior shows self-organized criticality (SOC). We argue that these models do not really fall under the SOC framework, since none of their states behaves as a critical state. On a secondary but related account, we give some thought to the recent hypothesis that multifractality in landscapes might be the result of heterogeneities of field properties [*Rodriguez-Iturbe et al.*, 1994]. Although this hypothesis seems reasonable and may well be true, the way it was tested using simulated landscapes from an "SOC" model has potential inference problems and warrants further investigation. The implications of our arguments may be significant for further development of landscape evolution models and interpretation of the underlying mechanisms of scaling observed in natural landscapes.

2. What Is a Critical State in Traditional Systems and in Systems Showing Self-Organized Criticality?

Near critical points (i.e., at limiting states of equilibrium of two-phase systems when the phases become identical) and points of second-order phase transitions, physical systems show anomalies in both static properties (thermodynamic coefficients, correlation length) and dynamic properties (relaxation rates, transport coefficients). These anomalies are called critical phenomena [see, e.g., *Ma*, 1976; *Patashinskii and Pokrovskii*, 1979], and the state of the system is called the critical state. It is established in modern theories of critical phenomena that large-scale fluctuations play a crucial role in the behavior of systems in the vicinity of the critical state. The correlation length of fluctuations (roughly their average length) grows infinitely as the system approaches the critical state [see, e.g., *Ma*, 1976, chap. 3; *Patashinskii and Pokrovskii*, 1979, chap. 2]. This means that any part of the system in the critical state can "feel" changes in other parts (cooperative behavior). Therefore if the system is in the critical state, a small local perturbation can cause a significant change in the configuration of the whole system. In the critical state, systems show both static and dynamic scaling. These two phenomena, expressed by scaling in the distribution of correlation lengths of fluctuations (implying lack of characteristic scale in space) and by corresponding power law distribution in relaxation times of the fluctuations (absence of temporal scale), respectively, are fundamentally related. Qualitatively, the reason for this relation is simple: the longer the correlation length of a fluctuation, the longer the time it needs to relax. Specifically, the characteristic frequency of fluctuations depends on their characteristic length as a power law [see, e.g., Hohenberg and *Halperin*, 1977; *Ma*, 1976; *Patashinskii and Pokrovskii*, 1979].

The concept of self-organized criticality was introduced by *Bak et al.* [1987] as a general organizing principle governing the evolution of nonlinear systems to a state which exhibits the features of a traditional critical state: there is no natural scale in this state, and the systems fluctuate strongly in space and time, exhibiting spatial and temporal scaling. This enabled Bak et al. (by analogy to traditional critical phenomena) to call the state reached by such systems critical and to coin the term "self-organized criticality" for these phenomena. For instance, in the typical example of a sand pile, as the pile is built up, the characteristic size of the largest avalanches grows until the pile reaches the critical state. As soon as this happens, one sand grain can produce an avalanche of any size up to the size of the system [*Bak et al.* 1987, p. 382; 1988, p. 365]. The strength of the avalanches (number of particles involved in an avalanche) follows a power law distribution. Also at the critical state, the sand pile surface shows fractal geometry. Another example of a system showing self-organized criticality is presented in a model of earthquakes [see, e.g., *Bak et al.*, 1994]. In this model, the transfer (according to some rule) of force to the neighboring elements may cause them to become unstable, thus triggering a chain reaction (modeling the earthquake). Again, this system evolves to a SOC state which is characterized by the presence of earthquakes of all possible energies, the energy of the earthquakes being distributed as a power law.

In systems showing self-organized criticality, similarly to traditional critical phenomena, temporal and spatial behavior are interrelated. In fact, *Bak et al.* [1987, 1988] show that there is a close connection between the "$1/f$" noise observed in many natural phenomena and the spatial self-similar fractal structure of the critical state. The relationship between spatial fractal

Paper number 96WR00161.
0043-1397/96/96WR-00161$05.00

behavior and temporal scaling in SOC systems was further studied and formally established by *Maslov et al.* [1994].

Systems showing self-organized criticality are characterized by two seemingly contradictory but in essence complementary features:

1. On the one hand, large, catastrophic events are intrinsic, unavoidable features of a system at the critical state [*Bak et al.*, 1994, p. 69]. Under small perturbations, such systems are proven to undergo changes which show power law distribution of strength. These changes can alter the configuration of the system dramatically. This feature corresponds to the dynamic properties of traditional critical states.

2. On the other hand, however, once the critical state is reached, the system stays there [*Bak et al.*, 1988, p. 365]. In other words, for systems showing SOC the critical state is an attractor of the dynamics. This means that the state of self-organized criticality is stationary; once it is achieved, the statistical properties of the system, such as spatial scaling and the power law frequency distribution of the events that change the system (avalanches or earthquakes), do not change. Except for fluctuations (which can be very strong, though; see feature 1), the system does not evolve. In that sense, the critical state of such systems is their destination point. The interplay of these two features determines the nontrivial behavior of systems exhibiting self-organized criticality.

3. Do the Current Models of River Network and Landscape Evolution Show Self-Organized Criticality?

In the model of river networks and landscape evolution introduced by *Rinaldo et al.* [1993] and further investigated by *Rigon et al.* [1994] and *Rodriguez-Iturbe et al.* [1994], self-organization takes place. However, we argue that none of the states of the model is critical and that the model therefore cannot be called an SOC model. In brief, the evolution rules of the model are as follows:

1. A given threshold shear stress value τ_c is assigned to the model.

2. Two variables are assigned to each site of a two-dimensional lattice: an elevation z_i and a discharge surrogated by the draining area A_i.

3. For each site the shear stress is computed as $\tau_i \propto A_i^{0.5}\Delta z_i$, Δz_i being the drop along the steepest descent. The computed τ_i are compared with the assigned critical shear stress τ_c. The elevation of the site j having the maximum exceedance of τ_j over τ_c is then reduced to the value which yields $\tau_j = \tau_c$ (this reduction simulates erosion). The released "mass" is evacuated from the system.

4. Drainage directions (fixed by the steepest descent in each site) are recomputed because they are altered as a result of the modified elevation of the site j. Accordingly, the values of the draining areas A_i and shear stresses τ_i are recalculated too.

5. Steps 3 and 4 are repeated until there are no exceedances of τ_i over τ_c.

6. The state achieved after step 5 is perturbed at random by adding elevation to a node. The perturbation may lead to a readjustment of the structure, and this is repeated until further perturbations do not induce variations in the configuration of the system.

For more details, the reader is referred to *Rinaldo et al.* [1993, p. 824]. The earlier model of *Takayasu and Inaoka* [1992] in many respects is analogous to the model described above except that the erosion is not modeled as a threshold process.

The authors of the model call the intermediate states reached after every step 5 (when there are no exceedances of τ_i over τ_c) critical. For example, *Rigon et al.* [1994, p. 976] describe step 5 of the model as follows: "5. Steps 3 and 4 are repeated until no exceedances are isolated. Thus at any stage the studied system evolves to a critical state (step 5). 6. The critical state 5 is perturbed...." The claim that the state of the system after each step 5 is critical, is also made by *Rinaldo et al.* [1993, p. 824] and *Rodriguez-Iturbe et al.* [1994, p. 3532]. We argue that these states cannot be considered critical for two reasons. First, the states achieved after every step 5 are intermediate; the statistics of the system continue to change systematically from step to step. up to the final configuration. This implies that the system does not exhibit one of the two inherent features of SOC systems, namely, feature 2. As was mentioned earlier, this feature requires that in SOC systems once a critical state is reached, the system stays there; i.e., a system showing self-organized criticality is stationary in the critical state, which is an attractor of the dynamics of the system. Second, the configuration of the system after every step 5, and before it reaches its final state, does not yet show fractal structure; it still has a characteristic scale as clearly demonstrated in Figures 4a and 4b of *Rinaldo et al.* [1993. p. 824], where one sees that a power law distribution of drainage areas and stream lengths is not present at that state. This again indicates that the state of the system after every step 5 is not a critical state.

Fractal structure indicated by a power law distribution of spatial characteristics (drainage areas and stream lengths), is present in the final state of the model. The authors of the model do not explicitly call the final state critical (although at one point they mention that "the studied system always evolves into a stable critical state" [*Rinaldo et al.*, 1993, p. 822]). However, as was discussed earlier. they do say that the critical state is achieved after each step 5. If this were true, then the final configuration of the system achieved after a series of perturbations followed by step 5 would also have to be critical, since once the critical state is reached, the SOC system remains there. We point out, however. that although the power law relations in spatial characteristics could mislead someone to consider this final state critical. one must note that SOC systems in the critical state also show a power law distribution of changes under small perturbations (e.g., a power law distribution of avalanche sizes or earthquake strengths), described earlier in the discussion of feature 1. In contrast to the behavior of SOC systems, in the final state of the landscape evolution model there are simply no changes at all, let alone the absence of large catastrophic events (characteristic of a critical state and implied by a power law distribution of changes). Indeed. since the drainage pattern (and consequently the feeding areas) do not change in the final state of the model, the shear stresses do not change either. and thus they do not exceed the critical value, which is a necessary condition for erosion to occur in this model (step 4). The analogous model of river network and landscape evolution by *Takayasu and Inaoka* [1992] also evolves into a state in which the river patterns are frozen. It should be pointed out. however, that in the final state of this model, the water flow continues to erode the surface. Takayasu and Inaoka recognized that the final state of their model "is very different from that of the SOC model" [*Takayasu and Inaoka*, 1992, p. 966] and introduced the term "a new

type of SOC system" to imply a system with spatial but not temporal scaling. We argue that this terminology is misleading and that not any system evolving to a fractal structure can be called an SOC system. As was mentioned earlier, in the critical state, both for traditional and for SOC systems, spatial and dynamic scaling are fundamentally related. Therefore a claim that a system exhibits SOC because it evolves into a state characterized by fractal geometry, i.e., shows "critical behavior in space" but does not show any changes under perturbations, seems internally contradictive. Thus since the final configuration of the system, i.e., the drainage pattern in the model of *Takayasu and Inaoka* [1992] and the drainage pattern and landscape itself in the model of *Rinaldo et al.* [1993], does not change under perturbations, the final state of the system cannot be considered critical.

In a recent popularized article by *Bak and Paczuski* [1993], the model of *Rinaldo et al.* [1993] was cited as an example of SOC models. To the general scientific audience, this in itself could put to rest any reservations such as the ones we raise here. However, we invite the reader to carefully examine this article, which in fact further supports rather than weakens our arguments. For example, *Bak and Paczuski* [1993, p. 39] stress that SOC systems are highly dynamic:

> A common feature of these complex systems is that they are driven by slowly pumping in energy, which is stored and later dissipated ..., in an avalanche process ... They exist in metastable states and small, seemingly insignificant, increments in energy input can trigger an arbitrary large avalanche."

This is completely different from (in fact, opposite to) the behavior of the considered landscape model which evolves into a state where perturbations do not change the configuration of the system. Furthermore, *Bak and Paczuski* [1993, p. 40] acknowledge that traditional equilibrium systems in a critical state also exhibit "fluctuations of all sizes and durations," which again implies not only spatial, but also temporal variability in such systems. Thus calling the considered landscape model a SOC model contradicts not only the relatively new concept of SOC systems, but also the concept of a critical state established in equilibrium physics long ago.

4. Caution for Spurious Multifractality

Rodriguez-Iturbe et al. [1994] tried to reproduce with their landscape evolution model the observed multifractal (as opposed to monofractal) structure of natural landscapes and argued that "multiple-scaling behavior ... cannot be explained in terms of homogeneous processes" and that "heterogeneity of field properties is needed for multiple scaling to emerge" [*Rodriguez-Iturbe et al.*, 1994, p. 3538]. To test this hypothesis, they introduced spatial inhomogeneity in the critical shear stress τ_c in two different ways. First, the spatial variability of shear stress was introduced as a correlated random field (log-normal field $\tau_c(\mathbf{x})$ with $\langle\tau_c\rangle = 1$, $\sigma_\tau^2 = 0.2$, and an exponential correlation structure with an integral scale equal to 2 pixels). In this case the simulated landscapes showed monofractal behavior [see *Rodriguez-Iturbe et al.*, 1994, Figure 9]. Second, inhomogeneity was introduced in a different way: a "highly bimodal distribution of critical shear stress" was used with values $\tau_c = 2$ for the upper half of the field divided along the diagonal through the outlet, and $\tau_c = 0.5$ for the lower half. The authors state that the elevation field [*Rodriguez-Iturbe et al.*, 1994, Plate 2] shows multiscaling behavior in this case, as is implied from the nonlinear behavior of the $K(q)$ function [see *Rodriguez-Iturbe et al.*, 1994, Figure 10]. However, one can see in Plate 2 that the introduction of inhomogeneity of the second type produced a significant step in the landscape along the line dividing the two zones. We demonstrate that imposing such a step onto a monofractal object, without any other change in the structure of the object, can lead to a deviation of its behavior from scaling which can be misinterpreted as multifractality.

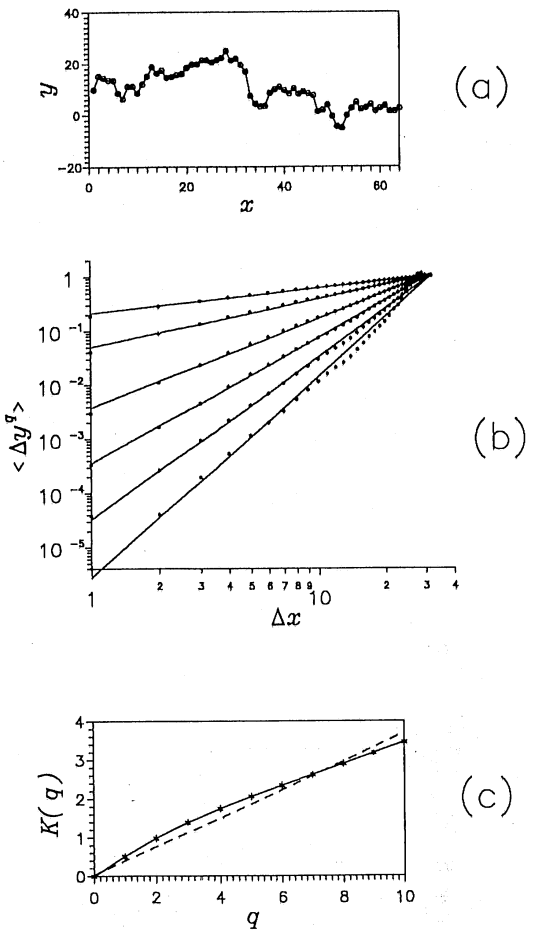

Figure 1. (a) A realization of simple Brownian motion with a step (in the middle) imposed. (b) Behavior of qth moments of the process shown in Figure 1a (the moments are produced by averaging over 500 realizations). Deviations from scaling produced by the imposed step are deceptively small, so the dependencies can easily be taken for straight lines; from bottom to top, the lines are for $q = 0, 2, 4, 6, 8, 10$. (c) $K(q)$ curve produced from Figure 1b under the (erroneous) assumption that Figure 1b shows scaling. This example depicts the possibility of inferring multifractality for a process which is clearly monofractal but has an imposed step (change in level).

The curve shown in our Figure 1a is a realization of simple Brownian motion with a step imposed: $x(t) = B(t) + a$ for $0 < x \leq 32$ and $x(t) = B(t)$ for $33 \leq x < 64$ (same length as in the work by *Rodriguez-Iturbe et al.* [1994]), with $a = 10$. Following the representation of *Rodriguez-Iturbe et al.* [1994, Figure 12] the points in our Figure 1b, i.e., moments $\langle \Delta y^q \rangle$ versus distance $\langle \Delta x \rangle$ for different powers q, were calculated. The points show some deviation from straight lines, but the deviation is not very strong, making it easy to mistake this

behavior for scaling (especially given the statistical variability in the moment estimates). In this case, one is bound to get misleading results if the calculation of the $K(q)$ curve is done using the "slopes" of the "straight lines" in Figure 1b. Indeed, though the object we analyzed is definitely not a multifractal, the curve $K(q)$ obtained in this way shows a deviation from linearity, as is shown in Figure 1c. Of course, the $K(q)$ curve obtained for the same Brownian motion without the step was perfectly linear. One can see that the curves $K(q)$ in our Figure 1c and in Figure 12 of *Rodriguez-Iturbe et al.* [1994] are practically identical. Thus we caution that the deviation of the $K(q)$ curve from linearity in their Figure 12 may be caused by the step in the landscape produced by the bimodality of the critical shear-stress function and does not necessarily demonstrate the multifractal structure of the simulated landscape. Notably, the first way of introducing spatial heterogeneity in the critical shear stress τ_c, such that the heterogeneity was spread over the lattice, did not lead to a deviation of the $K(q)$ curve from linearity [see *Rodriguez-Iturbe et al.*, 1994, Figure 9].

This example demonstrates that there are potential problems one should be aware of when analyzing real and simulated landscapes. These problems deserve special study.

5. Concluding Remarks

In this note we argue that in the current river network and landscape evolution models presented by *Takayasu and Inaoka* [1992] and *Rinaldo et al.* [1993], neither intermediate states nor the final state can be considered critical, and therefore in our opinion these models cannot be attributed to models showing self-organized criticality. Although they may still be valid simulation models, we caution that some claims based on the conclusion that they are SOC models should be revised. In particular, the claim that "optimal channel networks (OCN) obtained by minimizing the local and global rates of energy expenditure" [*Rodriguez-Iturbe et al.*, 1992, 1994; *Rinaldo et al.*, 1992] "are a particular case of self-organized critical structures" [*Rodriguez-Iturbe et al.*, 1994, p. 3531] is not justified by the model. The same caution applies to a more general question raised by Rodriguez-Iturbe that all self-organized structures might evolve through some global principle of energy minimization [see *Yam*, 1994, p. 26]. This conjecture may very well be true. We just point out that it does not follow from the models under consideration.

As the originators of the SOC concept have argued, the SOC mechanism can be responsible for many natural phenomena exhibiting both spatial and temporal scaling over a wide range of scales. Therefore the SOC concept looks promising for the description of natural landscapes which are known to show spatial scaling and undergo changes constantly from small to very large scales. However, in our opinion the considered models of landscape evolution do not really show SOC behavior.

As a final remark we point out that the considered models of landscape evolution lead to a final state in which the drainage pattern (model of *Takayasu and Inaoka* [1992]) or both the drainage pattern and landscape (model of *Rinaldo et al.* [1993]) remain frozen. We question how realistic conceptually such landscape evolution models are, since natural landscapes do change constantly and never really reach a "frozen state" of equilibrium. This, however, is outside the scope of this note and calls for careful investigation in itself.

Acknowledgments. This research was partially supported by NSF grant BSC-8957469 and NASA grant NAG-52108. This support is gratefully acknowledged.

References

Bak, P., and M. Paczuski, Why nature is complex, *Phys. World*, *12*, 39–43, 1993.

Bak, P., C. Tang, and K. Wiesenfeld, Self-organized criticality: An explanation of $1/f$ noise, *Phys. Rev. Lett.*, *59*, 381–384, 1987.

Bak, P., C. Tang, and K. Wiesenfeld, Self-organized criticality, *Phys. Rev. A*, *38*, 364–374, 1988.

Bak, P., C. Christensen, and Z. Olami, Self-organized criticality: Consequences for statistics and predictability of earthquakes, in *Nonlinear Dynamics and Predictability of Geophysical Phenomena, Geophys. Monogr. Ser.*, vol. 83, edited by W. I. Newman, A. Gabrielov, and D. L. Turcotte, pp. 69–74, AGU, Washington, D. C., 1994.

Hohenberg, P. C., and B. I. Halperin, Theory of dynamic critical phenomena, *Rev. Mod. Phys.*, *49*, 435–479, 1977.

Howard, A. D., A detachment-limited model of drainage basin evolution, *Water Resour. Res.*, *30*, 2261–2285, 1994.

Kramer, S., and M. Marder, Evolution of river networks, *Phys. Rev. Lett.*, *68*, 205–208, 1992.

Leheny, R. L., and S. R. Nagel, Model for the evolution of river networks, *Phys. Rev. Lett.*, *71*, 1470–1473, 1993.

Ma, S. K., *Modern Theory of Critical Phenomena*, Benjamin, White Plains, N. Y., 1976.

Maslov, S., M. Paczuski, and P. Bak, Avalanches and $1/f$ noise in evolution and growth models, *Phys. Rev. Lett.*, *73*, 2162–2165, 1994.

Patashinskii, A. Z., and V. L. Pokrovskii, *Fluctuation Theory of Phase Transitions*, Pergamon, Tarrytown, N. Y., 1979.

Rigon, R., A. Rinaldo, and I. Rodriguez-Iturbe, On landscape self-organization, *J. Geophys. Res.*, *99*, 971–993, 1994.

Rinaldo, A., I. Rodriguez-Iturbe, R. Rigon, R. L. Bras, E. Ijjasz-Vasquez, and A. Marani, Minimum energy and fractal structures of drainage networks, *Water Resour. Res.*, *28*, 2183–2195, 1992.

Rinaldo, A., I. Rodriguez-Iturbe, R. Rigon, and R. L. Bras, Self-organized fractal river networks, *Phys. Rev. Lett.*, *70*, 822–825, 1993.

Rodriguez-Iturbe, I., A. Rinaldo, R. Rigon, R. L. Bras, and E. Ijjasz-Vasquez, Energy dissipation, runoff production and the three-dimensional structure of channel networks, *Water Resour. Res.*, *28*, 1095–1103, 1992.

Rodriguez-Iturbe, I., M. Marani, R. Rigon, and A. Rinaldo, Self-organized river basin landscapes: Fractal and multifractal characteristics, *Water Resour. Res.*, *30*, 3531–3539, 1994.

Takayasu, H., and H. Inaoka, New type of self-organized criticality in a model of erosion, *Phys. Rev. Lett.*, *68*, 966–969, 1992.

Willgoose, G., R. L. Bras, and I. Rodriguez-Iturbe, A coupled channel network growth and hillslope evolution model, 1, Theory, *Water Resour. Res.*, *27*, 1671–1684, 1991a.

Willgoose, G., R. L. Bras, and I. Rodriguez-Iturbe, A coupled channel network growth and hillslope evolution model 2, Nondimensionalization and applications, *Water Resour. Res.*, *27*, 1685–1696, 1991b.

Yam, P., Branching out, *Sci. Am.*, *271* (5), 26–30, 1994.

E. Foufoula-Georgiou and V. B. Sapozhnikov, St. Anthony Falls Hydraulic Laboratory, University of Minnesota, Mississippi River at Third Avenue SE, Minneapolis, MN 55414-2196. (e-mail: efi@mykonos.safhl.umn.edu; sapoz001@maroon.tc.umn.edu)

(Received May 23, 1995; revised July 7, 1995;
accepted January 13, 1996.)

STATIC AND DYNAMIC SCALING OF LANDSCAPES

Efi Foufoula-Georgiou and Victor Sapozhnikov

St.Anthony Falls Hydraulic Laboratory
University of Minnesota, Minneapolis, MN 55414

Abstract

The purpose of this study is to explore quantitatively how the morphology and evolution of landscapes is connected to the physical and statistical characteristics of the shaping processes. Proceeding from the fact that landscapes are shaped to a large extent by forces of stochastic nature causing both roughening and smoothing we propose a model that incorporates these types of mechanisms. As a first step, we focus on roughening processes in this study. An important feature of the model is that it permits the shaping processes to be distributed over a wide range of scales. By combining dynamic and geometrical descriptions of landscapes we expect to gain a better understanding of the underlying mechanisms governing the formation and evolution of landscapes, such as tectonic, erosion and deposition processes, by relating these processes to the present geometry of the landscapes.

University of Minnesota Supercomputer Institute Report MSI 95/90 dated, April 1995.

(A copy can be requested directly from the authors)

J. Phys. A: Math. Gen. 28 (1995) 559–571. Printed in the UK

UofM, St. Anthony Falls Laboratory
Technical Paper 419 – Series A

Study of self-similar and self-affine objects using logarithmic correlation integral

Victor Sapozhnikov and Efi Foufoula-Georgiou
St. Anthony Falls Hydraulic Laboratory, University of Minnesota, Minneapolis, MN 55414, USA

Received 22 April 1994, in final form 27 October 1994

Abstract. We suggest a logarithmic correlation integral $z(x, y)$ as a good tool for investigating self-affine and self-similar objects. First, it enables us to extract fractal exponents ν_x and ν_y from one pattern of an object having any topology. Second, we show that the integral $z(x, y)$ which completely characterizes a monofractal object provides more information on the density correlation properties of the object than just the exponents ν_x and ν_y. We quantify this additional information by introducing two parameters: δ, characterizing the object's anisotropy of a non-scaling nature, and κ characterizing the curvature of the logarithmic correlation integral of the object. We demonstrate that the four parameters: ν_x, ν_y, δ and κ provide an effective parametrization of the logarithmic correlation integral of a self-affine monofractal object. We give some examples of self-affine objects, having the same fractal exponents ν_x and ν_y but different parameters δ and κ indicating the differences in the correlation properties of the objects. We demonstrate that even a self-similar object showing isotropic scaling ($\nu_x = \nu_y$) may have the non-scaling anisotropy parameter δ different from zero, which indicates that the object has an asymmetric integral $z(x, y)$ and, therefore, different correlation properties in different directions. It is shown that the equality $\kappa = 0$ outlines a class of objects for which the exponents ν_x and ν_y are not defined uniquely. For instance, such objects can be treated as both self-similar and self-affine. If κ is close to zero, estimation of the exponents ν_x and ν_y may become problematic. Relationships connecting the exponents ν_x, ν_y and fractal dimensions of the projection and cross section of an object are established.

1. Introduction

Many objects, such as relief vertical cross sections, rivers and river networks, growing surfaces and interfaces, dendritic structures, trails of Brownian motion and others are self-affine fractals [1]. Each part of a self-affine object is an image of the whole object (either strictly or in a statistical sense) scaled differently in different directions. In other words, if we take a part of the object within an $X \times Y$ rectangle and then change X and Y in a certain different way, we will get the same pattern. This finds its mathematical expression in the relationship

$$M(X, Y) \sim X^{1/\nu_x} \sim Y^{1/\nu_y} \tag{1}$$

where $M(X, Y)$ is the mass of the part of the object within the $X \times Y$ rectangle, and ν_x, ν_y are the fractal exponents.

While there are several methods for determination of the fractal dimension of self-similar objects, methods for determination of the fractal exponents characterizing self-affine objects seem to be much less developed. The fractal dimension of a self-similar object can be easily found using one pattern. However, in a general case, e.g. for branched structures,

0305-4470/95/030559+13$19.50

one cannot find the fractal exponents ν_x and ν_y from one pattern of a self-affine object. The problem is that the mass M only scales if the sides of the rectangle change in a certain different way and, in contrast to the self-similar case, we do not know *a priori* how to change X and Y because we do not know the ratio ν_x/ν_y. We can only state that the mass within the rectangle scales *provided* $X^{1/\nu_x} \sim Y^{1/\nu_y}$. Therefore, it seems that if one faces the problem of determination of the fractal exponents of a natural or simulated self-affine object using one pattern one would usually fail to do that. An appropriate method has only been developed for a special case when the self-affine object represents a non-branched line (e.g. see [2]).

The methods available for studying a general self-affine object do not analyse the geometry of the object, but rather follow how the mass M_0 of the total object changes as the sizes X_0 and Y_0 of the object change. If one has available either an ensemble of the same type of objects of different size, or the patterns of the object at different stages of growth, the ensemble or the evolution of the object can be characterized by exponents α_x and α_y using the relationship

$$M(X_0, Y_0) \sim X_0^{1/\alpha_x} \sim Y_0^{1/\alpha_y}. \tag{2}$$

We will call α_x and α_y *external exponents*, in contrast to the *internal exponents* ν_x and ν_y which characterize the geometry of the object. As shown in section 2 the internal and external scaling exponents have different meanings and are not always equal. A method for extracting the exponents ν_x and ν_y from one pattern of a fractal object is developed in section 3. We also introduce two parameters, δ and κ which complement the information contained in the fractal exponents ν_x and ν_y. We establish relationships connecting the exponents ν_x and ν_y and fractal dimensions of the projection and cross section of an object. In section 4 we demonstrate the applicability of the developed method using some fractal objects for which ν_x and ν_y are known theoretically. We show that the estimated values of ν_x and ν_y correspond to the theoretical ones. We also estimate the parameters δ and κ for these objects. In section 5 we show the significance of the introduced parameters δ and κ. Using these parameters we indicate some types of fractal objects showing rather unexpected correlation properties. Finally, some conclusions are drawn in section 6.

2. Internal fractal exponents versus external exponents

Since methods for extracting the internal exponents from one pattern of the object are not available in the general case, external exponents instead of internal ones are often used to describe the geometry of the object (see, e.g. [3–5]). However, this approach supposes that internal and external exponents are equivalent. We will present theoretical evidence and two examples demonstrating that this supposition is, generally speaking, wrong.

(i) The external exponents may be different from the internal ones. To compare the external exponents α_x and α_y with the internal ones, ν_x and ν_y, let us examine a growing self-similar object as a particular case of a self-affine object. If the size of the object is R and the mass is $M(R)$, then the mass within the square of size r covering a part of the object will be $m(r, R) = M(R)(r/R)^{1/\nu}$. If $M(R) \sim R^{1/\alpha}$, then

$$m(r, R) \sim R^{1/\alpha - 1/\nu}. \tag{3}$$

The last relationship shows that $\alpha = \nu$ if and only if m does not depend on R, which means that the external and the internal exponents are equal when, in the course of its evolution, the object neither grows nor dissolves inside. If this is not the case, the internal and external exponents differ.

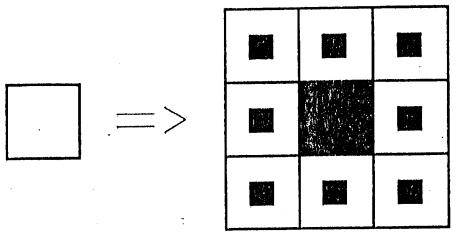

Figure 1. One step of a process where growth of an object in size is accompanied by its internal dissolution. Due to the dissolution the external exponents $\alpha_x = \alpha_y = \log 3/\log(64/9)$ characterizing the process are different from the internal fractal exponents $\nu_x = \nu_y = \log 3/\log 8$ describing the geometry of the object.

As an illustration let us build an ensemble of Sierpinsky carpets. Let the first one be just a square. To build the next carpet we take two steps. At the first step we put together 8 squares to build a regular 3×3 Sierpinsky carpet and at the second step we divide the initial squares in 9 squares and delete the middle one (which corresponds to the dissolution of the object in the course of its growth)—see figure 1. Repeating this process will give us an ensemble of Sierpinsky carpets with $\nu_x = \nu_y = \log 3/\log 8$. However, the mass of each next carpet will be not 8, but $8 \times (8/9)$ times greater than the mass of the previous one, and therefore for this process $\alpha_x = \alpha_y = \log 3/\log(64/9)$. Clearly, ν_x and ν_y are different from α_x and α_y in this case.

(ii) In some cases the ensemble of objects or the object growth is characterized by the external exponents, and the internal exponents of the objects are not defined uniquely at all. As the simplest case here let us consider compact objects. For example, Scheidegger river networks obtained by computer simulation are shown to be compact objects and their ensemble is characterized by the values $\alpha_x = \frac{2}{3}, \alpha_y = \frac{1}{3}$ [3,4]. It is implied (e.g. see the discussion after (4) in [3]) that these exponents characterize the fractal geometry of the networks. However, the compactness of a two-dimensional object means that the object is just a piece of a plane. This, in turn, means that, in contrast to the external exponents α_x and α_y that characterize the evolution (or the ensemble) of the networks, the internal exponents characterizing their geometry are not defined uniquely. For example, it is quite obvious that a piece of a plane can be treated as a self-similar object as well and be characterized by $\nu_x = \nu_y = 1/D = 1/2$. It will be shown formally in section 5 that any fractal exponents satisfying the relationship $\nu_x + \nu_y = 1$ describe a compact object. The non-uniqueness of the fractal exponents ν_x and ν_y can arise for non-compact objects too. As shown in section 5 there exists a class of non-compact fractal objects for which the internal exponents ν_x and ν_y are still not defined uniquely and derive general conditions under which an object falls into this class (equations (29) and (30)). The internal exponents of such objects are bounded only by relation (31).

The above theoretical evidence and examples demonstrate clearly that the external exponents α_x and α_y not only require a set of patterns for their estimation, but, generally speaking, are something different from the internal exponents ν_x and ν_y. Therefore elaboration of a method that would enable us to extract the internal fractal exponents from one pattern of an object is highly desirable. Such a method is developed in the next section.

3. Correlation characteristics of self-affine objects

3.1. A method for estimating the fractal exponents ν_x and ν_y

Let us write the scaling equation describing a self-affine object in the form

$$\left(\frac{X_2}{X_1}\right)^{1/\nu_x} = \left(\frac{Y_2}{Y_1}\right)^{1/\nu_y} = \frac{M_2}{M_1}. \tag{4}$$

Introducing $x = \log X$, $y = \log Y$ and $z = \log M$, we get

$$\frac{x_2 - x_1}{\nu_x} = \frac{y_2 - y_1}{\nu_y} = z_2 - z_1 \tag{5}$$

or

$$\frac{dx}{\nu_x} = \frac{dy}{\nu_y} = dz\,. \tag{6}$$

The function $M(X, Y)$ is known as the correlation integral [6]. Here by analogy we call the function $z(x, y)$ *the logarithmic correlation integral* of the object under study.

Equations (5) and (6) describe a cylindric surface $z(x, y)$, i.e. a surface that has constant derivative in a specific direction (the direction of the cylinder generating line). The second equality in (6) is true only if the first one is true. Comparing (6) with the equation

$$\frac{\partial z}{\partial x}dx + \frac{\partial z}{\partial y}dy = dz \tag{7}$$

valid for any values of dx and dy, we obtain

$$\nu_x \frac{\partial z}{\partial x} + \nu_y \frac{\partial z}{\partial y} = 1\,. \tag{8}$$

The last relationship provides a method for estimating the fractal exponents ν_x and ν_y of a self-affine object. Indeed, having estimated the logarithmic correlation integral $z(x, y)$ from a pattern of the object (by direct calculation of the mass $M(X, Y)$ within rectangles of sizes $X \times Y$), one can calculate the derivatives $\partial z(x, y)/\partial x$ and $\partial z(x, y)/\partial y$ and use them to find the values of ν_x and ν_y. Ideally, two points (x, y) giving different values of the derivatives $\partial z(x, y)/\partial x$ and $\partial z(x, y)/\partial y$ are sufficient, but for a good estimation it is preferable to compute the derivatives at all (x, y) points and follow a least-squares estimation technique. Such a technique is employed in section 4 to extract the fractal exponents from a pattern of some simulated fractal objects.

3.2. *Quantifying the other correlation characteristics of self-affine objects*

The solution of (8), as well as of (6), is

$$z(x, y) = \frac{x}{2\nu_x} + \frac{y}{2\nu_y} + \omega\left(\frac{x}{2\nu_x} - \frac{y}{2\nu_y}\right) \tag{9}$$

or

$$M(X, Y) = X^{1/2\nu_x} Y^{1/2\nu_y} \Omega\left(X^{1/2\nu_x} Y^{-1/2\nu_y}\right) \tag{10}$$

where $\omega(\xi)$ and $\Omega(\xi) \equiv \exp(\omega(\log \xi))$ are arbitrary functions.

Relationship (9) shows that the fractal exponents ν_x and ν_y contain only a part of the information on the correlation properties of a fractal object. The rest of the information is contained in the function $\omega(\xi)$. Indeed, in section 5 we give an example of fractal objects having the same values of ν_x and ν_y and different correlation properties because their $\omega(\xi)$ functions are different. It can be seen from (6) and (9) that while the fractal exponents ν_x and ν_y determine the direction of the generating line of the cylindric surface $z(x, y)$, the function $\omega(\xi)$ provides the additional information needed to describe the shape of any cross section of the cylindric surface. Thus, together ν_x, ν_y and $\omega(\xi)$ completely determine the shape of the logarithmic correlation integral $z(x, y)$.

Let us study some general features of the behaviour of the function $\omega(\xi)$ and $z(x, y)$. The nature of the function $M(X, Y)$ imposes some restrictions on $\omega(\xi)$. Indeed, by its

meaning, the function $M(X, Y)$ cannot have negative derivatives. As it follows from (9), the requirements $\partial M(X, Y)/\partial X > 0$ and $\partial M(X, Y)/\partial Y > 0$ lead to the inequality $-1 < \omega(\xi) < 1$. Assuming, that $\omega(\xi)$ does not oscillate at infinity, we find, that it has two asymptotes, $\omega'(+\infty)$ and $\omega'(-\infty)$. This gives us an important feature of $\omega(\xi)$ and of the $z(x, y)$ surface, namely, that $\omega(\xi)$ saturates to two lines at positive and negative infinities, i.e. $z(x, y)$ is composed of two planes (one when $\xi = x/2\nu_x - y/2\nu_y$ is a large positive value and the other when it is a large negative value) and an intermediate zone between them.

Since the $z(x, y)$ surface is a cylinder it can be described using only two coordinates (ξ, η) in the appropriate coordinate system (ξ, ζ, η). We obtain this coordinate system from the original (x, y, z) by (i) rotating the (x, y, z) system about the z-axis until the y-axis coincides with the projection of the generating line on the x–y plane, and (ii) rotating the system about the new x-axis until the y-axis coincides with the generating line. It can be shown that in this new coordinate system the equation for the logarithmic correlation integral takes the form

$$\eta(\xi) = \frac{\nu_y^2 - \nu_x^2}{2\nu_x\nu_y\sqrt{1 + \nu_x^2 + \nu_y^2}}\,\xi + \frac{\sqrt{\nu_y^2 + \nu_x^2}}{\sqrt{1 + \nu_x^2 + \nu_y^2}}\,\omega\left(\frac{\sqrt{\nu_y^2 + \nu_x^2}}{2\nu_x\nu_y}\,\xi\right). \tag{11}$$

As we see, because the ζ-axis coincides with the cylinder generating line, the equation for the cylinder surface is expressed in terms of ξ and η only. The function $\eta(\xi)$ is exactly what one sees when one views the $z(x, y)$ surface from the direction of the generating line. Since the ξ–η plane is orthogonal to the direction of the generating line, it is preferable to use $\eta(\xi)$ instead of $\omega(\xi)$ to describe the correlation properties of an object, since these properties are now not only complementary to the scaling exponents ν_x and ν_y (determining the direction of the generating line of the cylinder), but also independent of them.

Since the $z(x, y)$ surface has two asymptotic planes, its cross section $\eta(\xi)$ saturates to two asymptotic lines. Therefore $\eta'(\xi)$ has two asymptotic values, $\eta'(+\infty)$ and $\eta'(-\infty)$.

To quantify the correlation characteristics of a self-affine object, other than the fractal exponents ν_x and ν_y we introduce two parameters

$$\begin{aligned}\delta &= \frac{\eta'(-\infty) + \eta'(+\infty)}{2} \\ &= \frac{\nu_y^2 - \nu_x^2}{2\nu_x\nu_y\sqrt{1 + \nu_x^2 + \nu_y^2}} + \frac{\nu_y^2 + \nu_x^2}{2\nu_x\nu_y\sqrt{1 + \nu_x^2 + \nu_y^2}}\,\frac{\omega'(-\infty) + \omega'(+\infty)}{2}\end{aligned} \tag{12}$$

and

$$\kappa = \frac{\eta'(-\infty) - \eta'(+\infty)}{2} = \frac{\nu_y^2 + \nu_x^2}{2\nu_x\nu_y\sqrt{1 + \nu_x^2 + \nu_y^2}}\,\frac{\omega'(-\infty) - \omega'(+\infty)}{2}. \tag{13}$$

The value of δ characterizes the anisotropy of the cross section of the function $z(x, y)$ ($\delta = 0$ when the cross section is isotropic), and κ is a measure of curvature of the $z(x, y)$ function ($\kappa = 0$ when the surface is flat). These two parameters are important characteristics of a self-affine object. They complement the information contained in the fractal exponents ν_x and ν_y. The parameter δ describes a different type of anisotropy of a self-affine object than the ratio of the scaling exponents ν_x/ν_y. In fact, in section 5 we show that even a self-similar object ($\nu_x = \nu_y$) may have anisotropic correlation characteristics which is indicated by $\delta \neq 0$. To distinguish between these two types of anisotropy we coined the terms *scaling anisotropy parameter* for ν_x/ν_y and *non-scaling anisotropy parameter* for δ. Regarding the curvature parameter κ, in section 5 we show that if it is equal to zero, i.e.

the cylindric surface $z(x, y)$ degenerates into a plane, the exponents ν_x and ν_y of the fractal object are not defined uniquely.

3.3. Further study of the shape of the surface $z(x, y)$. Connection between the exponents ν_x and ν_y and other characteristics of fractal objects

Let us now find the equations for the plane parts of the surface $z(x, y)$. To do that we consider the slope of each plane in the x and y directions. By definition of the function $M(X, Y)$ the derivatives $\partial z(x, 0)/\partial x$ and $\partial z(0, y)/\partial y$ are fractal dimensions of cross sections of the object in the directions of X and Y axes, D_{cx} and D_{cy}, respectively. As shown in the appendix the derivatives $\partial z(0, y)/\partial x$ and $\partial z(x, 0)/\partial y$ are correlation fractal dimensions D_2 [6] of the projections of the object on X and Y axes, D_{px2} and D_{py2}, respectively. Putting $z(0, 0) = 0$ (which is just a matter of normalization of $M(X, Y)$) we get the equations for the two asymptotic planes

$$z_-(x, y) = D_{px2}x + D_{cy}y \tag{14}$$

$$z_+(x, y) = D_{cx}x + D_{py2}y\,. \tag{15}$$

Let us remind the reader that the generalized fractal dimensions D_q are

$$D_q = \lim_{\varepsilon \to 0} \frac{\log(\sum p_i^q)}{(q-1)\log \varepsilon} \qquad q \neq 1 \tag{16}$$

$$D_1 = \lim_{\varepsilon \to 0} \frac{\sum p_i \log p_i}{\log \varepsilon}\,. \tag{17}$$

Here p_i is the fraction of the measure in a box of size ε (in our case it is the fraction of the object that projects into an interval of size ε). D_0 is the fractal dimension of the support of the measure, D_1 and D_2 are called information and correlation dimensions, respectively.

The relationships (14) and (15) enable us to demonstrate clearly what one gets when one determines the fractal dimension of a self-affine object: one finds how the mass within an $X \times Y$ rectangle changes as its sides change *proportionally to each other*. In other words, one just finds the slope of the section of the plane $z(x, y)$ by the plane $y = x + a$, where constant $a = \log(Y/X)$. If $\nu_x > \nu_y$ then for positive values of a ($Y > X$) the plane $y = x + a$ will only intersect the $z_-(x, y)$ plane, while for negative values of a both $z_-(x, y)$ and $z_+(x, y)$ planes will be intersected. This creates two slopes, corresponding to what is called global and local fractal dimensions of a self-affine object D_G and D_L, correspondingly [8]. Putting $y = x + a$ in (14) and (15), we obtain that for $\nu_x > \nu_y$

$$D_G = D_{px2} + D_{cy} \tag{18}$$

$$D_L = D_{py2} + D_{cx}\,. \tag{19}$$

It follows from (14), (15) and (8) that for the case $D_{px2} = D_{py2} = 1$ this result coincides with the expressions $D_G = (\nu_y - \nu_x + 1)/\nu_y$, $D_L = (\nu_x - \nu_y + 1)/\nu_x$ from [8].

Having substituted (9) in (14) and (15), and differentiated the equations with respect to x and y one can see that the fractal dimensions of the cross sections and of the projections, D_{cx}, D_{cy} and D_{px2}, D_{py2} are connected with the $\omega(\xi)$ function by the following relationships:

$$\omega'(-\infty) = -2\nu_y D_{cy} + 1 = 2\nu_x D_{px2} - 1 \tag{20}$$

$$\omega'(+\infty) = 2\nu_x D_{cx} - 1 = -2\nu_y D_{py2} + 1 \tag{21}$$

so knowing, say, ν_x, ν_y, D_{px2} and D_{py2} one can easily calculate the parameters δ and κ from (12), (13) and (20), (21).

Substituting (14) and (15) into (8) we obtain the important relationships

$$\nu_x D_{cx} + \nu_y D_{py2} = 1 \tag{22}$$

$$\nu_x D_{px2} + \nu_y D_{cy} = 1 \tag{23}$$

which can be used for estimation of ν_x and ν_y given D_{cx}, D_{cy}, D_{px2} and D_{py2}. For a self-similar object (22) and (23) give

$$D_{cx} + D_{py2} = D_{cy} + D_{px2} = D \tag{24}$$

where D is the fractal dimension of the object. We note that the last equation is different from the equation obtained by Mandelbrot [8]: $D_{cx} + D_{py1} = D$ where D_{py1} is the information dimension [6] of the projection on the Y-axis. In the next section we consider some examples confirming our result (22)–(24).

4. Analysis of correlation properties of some fractal objects

To illustrate the application of the proposed approach for analysing self-affine objects we study the correlation properties of three fractal objects whose fractal exponents we know in advance. The objects are shown in the upper row of figure 2: (*a*) simulated river ($\nu_x = \nu_y = 0.77$), (*b*) trace of Brownian motion ($\nu_x = 1$, $\nu_y = \frac{1}{2}$) and (*c*) 3×5 Sierpinsky carpet ($\nu_x = \log 5/\log 6 = 0.898$, $\nu_y = \log 3/\log 6 = 0.613$). (The simulated river channel shown in figure 2(*a*) is built by a special type of a self-avoiding walk. If a walking particle crossed its own trajectory, the formed loop was erased. The final trajectory of a random walk was regarded as a river. See [2, 9] for details).

Taking advantage of (8) we find the values of the exponents ν_x and ν_y for the objects shown in figure 2(*a*) and (*b*)—see figure 3. They are (*a*) $\nu_x = \nu_y = 0.77$ and (*b*) $\nu_x = 1.00$, $\nu_y = 0.48$, in agreement with the theoretical values.

Let us first visualize the surfaces $z(x, y)$ of the objects (see figures 2(*a*)–(*c*), bottom row). Since the functions $z(x, y)$ of fractal objects are cylindric surfaces we can view them in the direction of the cylinder generating line (see (5) and (6)). In other words, it is possible to adjust the rotation angle φ about the z-axis and the tilt angle ψ above the x–y plane from which the surface is viewed to see only the edge of the surface (which is the $\eta(\xi)$ function). It is not difficult to show that the following relationships connecting the angles and the exponents hold:

$$\tan\varphi = \nu_x/\nu_y \tag{25}$$

$$\sin\psi = \left(1 + \nu_x^2 + \nu_y^2\right)^{-1/2} \tag{26}$$

or, reversely

$$\nu_x = \sin\varphi \cot\psi \tag{27}$$

$$\nu_y = \cos\varphi \cot\psi\,. \tag{28}$$

The second row of figure 2(*a*)–(*c*) shows the surfaces viewed from the angles φ and ψ determined by (25) and (26). It can be seen that $z(x, y)$ really represent cylindric surfaces and that the angles φ and ψ correspond to the relationships (25)–(28).

The surface $z(x, y)$ of the Sierpinsky carpets is step-like because of the step-like procedure of their construction. This produces a large spread in the values of the derivatives $\partial z/\partial x$ and $\partial z/\partial y$ and does not allow us to find its fractal exponents from (8). However, looking at its $z(x, y)$ surface in figure 2(*c*), middle row, one can see that apart from its

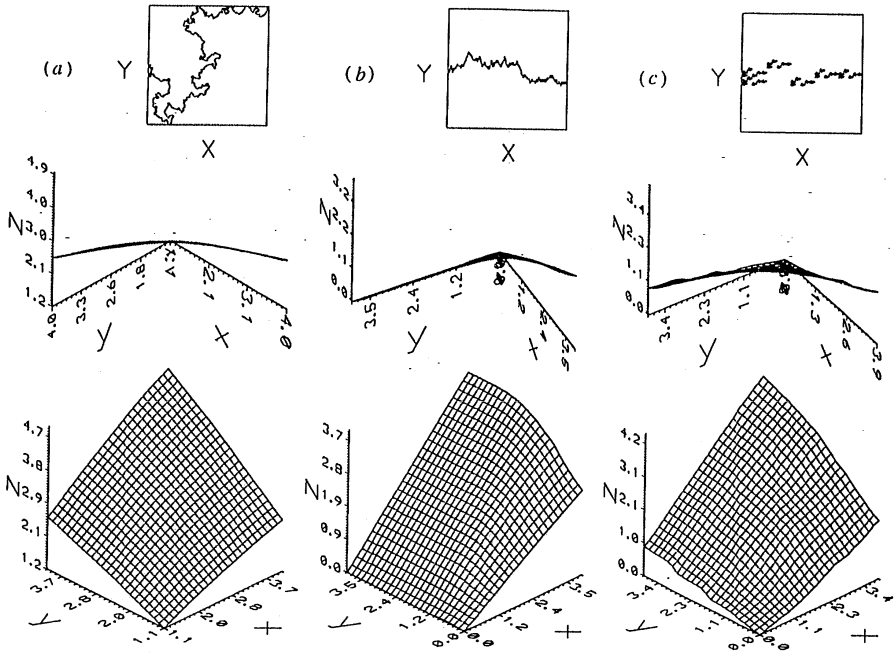

Figure 2. Fractal objects and their $z(x, y)$ functions: (a) simulated river ($\nu_x = \nu_y = 0.77$, $\delta = 0$, $\kappa = 0.27$), (b) Brownian motion trace ($\nu_x = 1$, $\nu_y = 1/2$, $\delta = -0.083$, $\kappa = 0.417$) and (c) 3×5 Sierpinsky carpet ($\nu_x = \log 5/\log 6 = 0.898$, $\nu_y = \log 3/\log 6 = 0.613$, $\delta = -0.038$, $\kappa = 0.266$). The second row shows the surfaces viewed from the angles φ and ψ determined by (25) and (26).

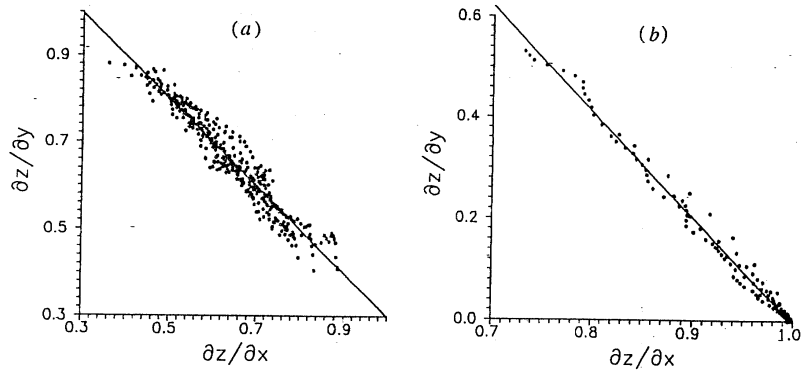

Figure 3. Estimation of the fractal exponents ν_x and ν_y for (a) simulated river—see figure 2(a), and (b) trace of Brownian motion—see figure 2(b). Advantage is taken of (8). The estimated values are (a) $\nu_x = \nu_y = 0.77$ and (b) $\nu_x = 0.48$, $\nu_y = 1.00$.

step-like form it is a cylindric surface, with the direction of generating line corresponding to (25)–(28).

As can be seen from (14) and (15) the slopes of the intersection of the $z(x, y)$ surface with the XZ and YZ planes are D_{cx} and D_{cy}, respectively. Having found these values for

Table 1. Summary of correlation characteristics ν_x, ν_y, δ and κ, of the fractal objects simulated in the paper.

Object	Figure	ν_x	ν_y	ν_y/ν_x	δ	κ
River channel	2(*a*)	0.77	0.77	1	0	0.27
Trace of Brownian motioin	2(*b*)	1	0.5	0.5	−0.083	0.417
5×3 Sierpinsky carpet	2(*c*)	0.898	0.613	0.683	−0.038	0.266
3×3 Sierpinsky carpet	4(*a*)	1	1	1	0	0.577
3×3 Sierpinsky carpet	4(*b*)	1	1	1	−0.268	0.310
3×3 Sierpinsky carpet	4(*c*)	1	1	1	0	0.040

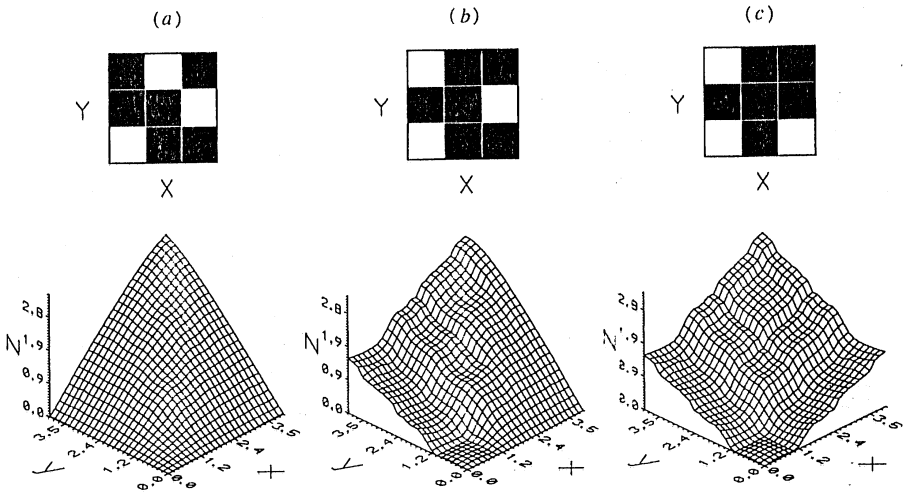

Figure 4. Logarithmic correlation integrals $z(x, y)$ of different self-similar Sierpinsky carpets having fractal dimension $D = 1$ (bottom figures) and the corresponding generators (top figures). The deleted parts are marked black. Though the carpets have the same fractal dimension their correlation properties are different, which is reflected in the difference of their $z(x, y)$ functions. The asymmetric function $z(x, y)$ for the carpet (*b*) shows that this self-similar fractal is anisotropic.

the three analysed objects we used (20) and (21) to estimate $\omega'(+\infty)$ and $\omega'(-\infty)$ and then (12) and (13) to determine the parameters δ and κ characterizing the anisotropy and the curvature of their logarithmic correlation integrals $z(x, y)$. The values of the parameters are: for the river $\delta = 0$, $\kappa = 0.27$, for the trace of Brownian motion $\delta = -0.083$, $\kappa = 0.417$, and for the Sierpinsky carpet $\delta = -0.038$, $\kappa = 0.266$ (see table 1 for a summary). For all three objects the curvature parameter is significantly different from zero. As will be seen in the next section this is a necessary condition for being able to estimate the fractal exponents ν_x and ν_y. The anisotropy parameter δ is equal to zero for the self-similar object, the river channel. One could think that a self-similar object is bound to have symmetric correlation properties and therefore its non-scaling anisotropy parameter δ should always be equal to 0. However, as shown in the next section this is not true.

We make use of the above fractal objects to demonstrate that relationships (22)–(24) hold. For instance, from the $z(x, y)$ function of the river channel (figure 2(*a*)) we found $D_{px2} = D_{py2} = 0.91$ and $D_{cx} = D_{cy} = 0.39$, which are in a good agreement with the fractal exponents of the channel $\nu_x = \nu_y = 0.77$ found above. We also projected the picture of

the river and found the values D_{px2} and D_{py2} directly by calculating the sum from the right part of (A4). The direct calculation gives $D_{px2} = D_{py2} = 0.92$, in good agreement with the values found from the analysis of the function $z(x, y)$.

Application of the same procedure to some Sierpinsky carpets confirms the results (22)–(24), as well. In these cases we were also able to make sure that the determined values of the derivatives $\partial z(0, y)/\partial x$ agree with the theoretical values of the correlation dimension D_{px2}, and not with the informative dimension D_{px1} as implied by Mandelbrot in [8]. For instance, for the Sierpinsky carpet, shown in figure 4(*c*) $\partial z(0, y)/\partial x = 0.53$; the projection of the carpet and the direct calculation gives the same value. The theoretical value $D_{px2} = D_{py2} = -\log(\sum p_i^2)/\log 3 = 0.535$, while the informative dimension $D_{px1} = D_{py1} = -(\sum p_i \log p_i)/\log 3 = 0.579$. The dimensions of the cross sections found from the analysis of the $z(x, y)$ function are $D_{cx} = D_{cy} = 0.47$, so $D_{cx} + D_{py2} = 1$, in agreement with (24).

5. Surprising correlation properties of some fractal objects

5.1. A class of fractal objects for which the scaling exponents ν_x and ν_y are not defined uniquely

As pointed out in section 3, having found the values of D_{cx}, D_{cy}, D_{px2} and D_{py2} one can calculate the fractal exponents ν_x and ν_y from (22) and (23). However, this system of linear equations has an infinite set of solutions if the fractal dimensions of the cross sections are equal to the fractal dimensions of the corresponding projections

$$D_{cx} = D_{px2} \equiv D_x \tag{29}$$

$$D_{cy} = D_{py2} \equiv D_y\,. \tag{30}$$

If equations (29) and (30) hold the cylindric surface $z(x, y)$ degenerates into a plane. Indeed, comparing (13), (20) and (21) with (8) one can easily see that the conditions (29) and (30) are equivalent to one condition: the curvature parameter $\kappa = 0$, which means that the function $\omega(\xi)$ is a straight line, i.e. $z(x, y)$ is a plane. In this case, equations (22) and (23) are reduced to one equation

$$\nu_x D_x + \nu_y D_y = 1 \tag{31}$$

having an infinite set of solutions ν_x and ν_y. Equations (29) and (30) (or, equivalently, the condition $\kappa = 0$) specify a class of fractal objects for which it is impossible to point out a unique pair of fractal exponents. These objects can be described by any exponents which are in agreement with (31). In other words, when the surface $z(x, y)$ degenerates into a plane, the difference between the self-affine and self-similar object disappears and there is no preferable direction for cutting the surface because the trace is a straight line in any direction. For instance, a compact object is characterized by $D_{cx} = D_{cy} = D_{px2} = D_{py2} = 1$. Comparing this relationship with (31), we obtain $\nu_x + \nu_y = 1$. This means that a compact object can be treated as a self-affine one with arbitrary ratio ν_x/ν_y, including e.g. $\nu_x/\nu_y = 1$ (self-similar case). The only significant relationship for such an object is that the sum of the exponents ν_x and ν_y is 1.

It is important to emphasize that relationships (29) and (30) can also be true for a non-compact object. For example, the Sierpinsky carpet having a 3×5 generator with four non-empty cells in the corners (see figure 5) has $D_{cx} = D_{px2} = \log 2/\log 5$, $D_{cy} = D_{py2} = \log 2/\log 3$, and the only thing one can say about the fractal exponents ν_x and ν_y is that they must satisfy (31).

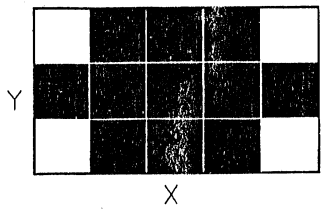

Figure 5. For this Sierpinsky carpet (29) and (30) hold, i.e. fractal dimensions of cross sections are equal to the corresponding fractal dimensions of projections ($D_{cx} = D_{px2} = \log 2/\log 5$, $D_{cy} = D_{py2} = \log 2/\log 3$) and, equivalently, the curvature parameter $\kappa = 0$. Therefore its logarithmic correlation integral $z(x, y)$ degenerates into a plane and there is no unique pair of the exponents ν_x and ν_y for this object. Any pair of the exponents bound by relationship (31): $(\log 2/\log 5)\nu_x + (\log 2/\log 3)\nu_y = 1$ characterizes this object.

As we have seen, the curvature parameter κ is an important characteristic of correlation properties of an object. Indeed, if $\kappa = 0$, the fractal object can be characterized by an infinite number of exponents ν_x and ν_y. Moreover, even if $\kappa \neq 0$, but is close enough to zero, that is, the $z(x, y)$ function is flat, the estimation of the fractal exponents may become impossible (though in this case they exist). For example, if one uses (8) to estimate the exponents ν_x and ν_y one may find that since the surface $z(x, y)$ is not curved enough, the variations in the true values of the partial derivatives $\partial z(x, y)/\partial x$ and $\partial z(x, y)/\partial y$ over the surface $z(x, y)$ are small and therefore masked by statistical fluctuations.

5.2. Fractal objects having the same scaling exponents ν_x and ν_y and different correlation properties. Anisotropic self-similar objects

We have shown that in some cases one surface $z(x, y)$ can be characterized by different fractal exponents ν_x and ν_y. We will now demonstrate that different surfaces may correspond to the same exponents. Indeed, Sierpinsky carpets whose generators and corresponding $z(x, y)$ surfaces are shown in figures 4(*a*)–(*c*) have the same fractal exponents $\nu_x = \nu_y = 1/D = 1$. Calculating D_{p2} as $-\log(\sum p_i^2)/\log 3$, where $p_i = n_i/n$ (n_i is the number of non-empty squares in the ith row and n is the total number of non-empty squares in a generator), and using (12), (13), (20) and (21), we find: (i) $D_{px2} = D_{py2} = 1$, $\delta = 0$, $\kappa = 0.577$, (ii) $D_{px2} = 0.535$, $D_{py2} = 1$, $\delta = -0.268$, $\kappa = 0.310$, and (iii) $D_{px2} = D_{py2} = 0.535$, $\delta = 0$, $\kappa = 0.040$. So, objects having the same fractal dimension may have different parameters κ and δ and, hence, different surface $z(x, y)$. Moreover, the example shown in figure 4(*b*) demonstrates that density correlation characteristics even of a self-similar object can be different in different directions. This anisotropy is reflected in the asymmetry of the function $z(x, y)$ and is characterized by the value of the non-scaling anisotropy parameter $\delta = -0.268$.

6. Conclusion

The approach proposed, based on the study of the logarithmic correlation integral (i) provides a method for extracting the fractal exponents ν_x and ν_y characterizing the geometry of a self-affine or self-similar object from one pattern only and (ii) permits a better understanding of the correlation properties of such objects. To the best of our knowledge no such method is available in the literature and this may have resulted in the erroneous use of the external exponents α_x and α_y (which can be estimated from an ensemble or evolving pattern) for the description of the geometry of a self-affine object. As demonstrated in this paper the external and internal exponents are generally not equal, except in the special case that the object evolves in a way that it neither grows nor dissolves inside. Even in such a case the suggested approach enables one to find the external exponents (unless (29) and (30) hold) and thus, to predict the evolution of the object from one pattern only instead of an ensemble

of patterns.

Apart from the ability to estimate ν_x and ν_y the use of the logarithmic correlation integral provides more information about the correlation structure of an object than simply ν_x and ν_y. This additional information was quantified by introducing two parameters, one of them (δ) measuring the anisotropy of the object of non-scaling nature and the other (κ) measuring the curvature of the logarithmic correlation integral. Several examples were presented to illustrate the fact that even self-similar fractals for which $\nu_x = \nu_y$ (i) may have different correlation properties and (ii) may still exhibit anisotropy in their correlation structure. The four parameters ν_x, ν_y, δ and κ were connected to fractal dimensions of projections and cross sections of the object. Conditions under which a fractal object has non-unique ν_x and ν_y parameters were derived.

In this paper our analysis focused on the characterization of a monofractal object. The same analysis could be applied to a multifractal object to characterize the behaviour of the first moments only of its correlation structure. However, to fully characterize a multifractal self-affine object one could introduce a function $z(x, y; q)$ where the parameter q characterizes the order of the moment. Following the same approach as here a reduced efficient parametrization of a self-affine multifractal object could be obtained in terms of four functions: $\nu_x(q)$, $\nu_y(q)$, $\delta(q)$ and $\kappa(q)$. This extension is currently under investigation.

Acknowledgments

We would like to thank A Carsteanu and V Nikora for helpful discussions. This research was partially supported by NSF grants BSC-8957469 and EAR-9117866 and NASA grant NAG-52108.

Appendix.

The density correlation function of the object $c(X, Y) = \partial^2 M(X, Y)/\partial X \partial Y$ is the probability to find a particle at the point $(X_0 + X, Y_0 + Y)$ provided there is a particle at the point (X_0, Y_0). For the lattice model it can be estimated as

$$c(X, Y) = \frac{1}{N} \sum_{X_0, Y_0} \delta(X_0, Y_0)\delta(X_0 + X, Y_0 + Y) \tag{A1}$$

where N is the total number of the particles in the object, $\delta(X_0, Y_0) = 1$ if there is a particle at the point (X_0, Y_0) and $\delta(X_0, Y_0) = 0$ otherwise. Hence $M(X, Y)$ can be estimated as

$$\sum_{U=0}^{X} \sum_{V=0}^{Y} c(U, V) = \frac{1}{N} \sum_{U=0}^{X} \sum_{X_0, Y_0} \delta(X_0, Y_0) \sum_{V=0}^{Y} \delta(X_0 + U, Y_0 + V). \tag{A2}$$

For large values of Y so that $Y \simeq Y_{0,\max}$, where $Y_{0,\max}$ is the size of the object in the Y-direction

$$\sum_{V=0}^{Y} \delta(X_0 + U, Y_0 + V) \simeq N_X(X_0 + U) \tag{A3}$$

where $N_X(X_0 + U)$ is the number of particles of the object that project onto the lattice point $X_0 + U$ of X-axis. Therefore, for large values of Y the function $M(X, Y)$ can be estimated as

$$\frac{1}{N} \sum_{U=0}^{X} \sum_{X_0} \sum_{Y_0} \delta(X_0, Y_0) N_X(X_0 + U) = \frac{1}{N} \sum_{X_0} N_X(X_0) \sum_{U=0}^{X} N_X(X_0 + U). \tag{A4}$$

The right-hand side of the last equation up to a constant coefficient coincides with the expression for the correlation integral from [7] which in a one-dimensional case is $C(X) = N^{-2} \sum_{i,j=1}^{N} \theta(X - |X_{0i} - X_{0j}|)$ where $\theta(X)$ is the Heaviside function and X_{0i}, X_{0j} are the coordinates of the particles. The value $C(X)$ is the number of pairs (i, j) whose distance $|X_{0i} - X_{0j}|$ is less then X. When calculating the right-hand side of expression (A4) one performs the same procedure as when he calculates $C(X)$ for the projection of the particles of the object on X-axis. As is shown in [6,7], $C(X)$ scales as X^{D_2}. In other words, $M(X, Y) \sim X^{D_{px2}}$ and $\partial z(x, y)/\partial x = D_{px2}$ for $Y \simeq Y_{0,\max}$. Since for $y/v_y \gg x/v_x$ the surface $z(x, y)$ is a plane and the derivative $\partial z(x, y)/\partial x$ is constant the equality $\partial z(x, y)/\partial x = D_{px2}$ is valid not only for $y \simeq \log Y_{0,\max}$, but also for any $y \gg (v_y/v_x)x$.

References

[1] Mandelbrot B B 1977 *Fractals: Form, Chance, and Dimension* (New York: Freeman)
[2] Nikora V I, Sapozhnikov V B and Noever D A 1993 *Water Resources Res.* **29** 3561
[3] Kondoh H, Matsushita M and Fukuda Y 1987 *J. Phys. Soc. Japan* **56** 1913
[4] Meakin P, Feder J and Jossang T 1991 *Physica* **176A** 463
[5] Nikora V I and Sapozhnikov V B 1992 *Water Resources Res.* **29** 3569
[6] Grassberger P and Procaccia I 1982 *Physica* **9D** 189
[7] Grassberger P and Procaccia I 1982 *Phys. Rev. Lett.* **9D** 346
[8] Mandelbrot B B 1986 Self-affine fractal sets *Fractals in Physics* (Amsterdam: North-Holland) p 3
[9] Sapozhnikov V B and Nikora V I 1993 *J. Phys. A: Math. Gen.* **26** L623